The Effect of the Magnetic Field Structure on the Spectral Properties of Accreting Neutron Stars

Nabil Brice

A dissertation submitted in partial fulfillment

of the requirements for the degree of

Doctor of Philosophy

of

University College London.

Space Science and Climate Physics

University College London

February 26, 2024

I, Nabil Brice, confirm that the work presented in this thesis is my own. Where information has been derived from other sources, I confirm that this has been indicated in the thesis.

Abstract

The description of an accreting neutron star (NS) with a pure dipole magnetic field structure, allowing for a tilt from the spin-axis, is challenged when applied to Pulsating Ultra-Luminous X-ray sources (PULXs), which are X-ray bright ($\gtrsim 10^{39}$erg s^{-1}), accreting, magnetised NSs.

One explanation of the apparent super-Eddington emission from PULXs involves the NS's ultra-strong ($\gtrsim 10^{13}$G) magnetic field reducing the opacity of the accreting plasma, consequently raising its Eddington limit (from $\sim 10^{38}$erg s^{-1}). However, NGC5907 ULX-1 presents an issue for the simple dipole topology, as its observed spin-period and inferred magnetic field strength would place it in the propeller regime. Relaxing the dipole topology assumption resolves this by decoupling the magnetic field strengths in the accretion column and magnetosphere. I developed an accretion column model, incorporating multipole components, and calculated the change to the maximum luminosity. Results demonstrated the need for a multipolar magnetic field in NGC5907 ULX-1 and likely in NGC7793 P13.

PULXs' high accretion rates were theorised to sheathe the NS magnetosphere in an optically thick envelope. Whereas the luminosity amplification model was unsuccessful in explaining the observed pulsed fraction of PULXs, no similar test had been done for the optically thick envelope model. I developed a model for the time-resolved spectral emission from an optically thick envelope, accounting for tilt from the spin-axis, and calculated the pulsed fraction. This model successfully explained the high pulsed fractions seen in NGC7793 P13 and NGC5907 ULX-1.

In conclusion, these results show the significance of the magnetic field structure in shaping the observed emission, especially for PULXs. Future missions that

provide higher quality datasets of NS spectra will demand a more comprehensive understanding of the effects of the magnetic field structure. This thesis contributes to advancing that understanding.

Impact Statement

The impact of the work in §3 and §4 has contributed to the scholarship on the nature of Ultra-luminous X-ray sources. These chapters have been published in the Monthly Notices of the Royal Astronomical Society as full articles:

- **Brice, N.**, Zane, S., Turolla, R., Wu, K. (2021) Super-eddington emission from accreting, highly magnetized neutron stars with a multipolar magnetic field, Monthly Notices of the Royal Astronomical Society, Volume 504, Issue 1, pp.701-715

- **Brice, N.**, Zane, S., Taverna, R., Turolla, R., Wu, K. (2023) Observational properties of accreting neutron stars with an optically thick envelope, Monthly Notices of the Royal Astronomical Society, Volume 525, Issue 3, pp.4176-4185

In §3, I developed an accretion column model suitable for accreting, highly magnetised neutron stars with a multipolar magnetic field. I applied this model to two Pulsating Ultra-luminous X-ray sources, which are widely considered to be accreting neutron stars, in order to diagnose the necessity for a multipolar magnetic field. The analysis showed that an interpretation of these sources as highly magnetised neutron stars specifically with a complex magnetic field topology (than a pure dipole) was favoured. This has resolved the tension between the required strength of the magnetic field local to the surface (to allow for a sufficient raising of the maximum luminosity) with the constraint on the maximum strength of the dipole component of the magnetic field placed by the observed spin period of the neutron star. More generally, this work has shown that a more complex magnetic

field topology can significantly influence the accretion column properties, which subsequently affect the emission properties. Future studies that attempt to diagnose system properties from the (observed) emission properties should take into account the affects of the magnetic field topology to construct a more accurate model.

In addition, the work in §3 has highlighted the need for a theoretical investigation of suitable models for the interaction of a geometrically thick disc with the neutron star magnetic field. I considered a simplified parameterised model for the size of the disc-magnetosphere boundary, where the accreting material is loaded onto the magnetic field lines, since the disc-magnetosphere interaction in the super-Eddington accretion regime is still currently poorly understood. I found the size to be a crucial factor on the accretion column geometry and subsequently on the emission properties, especially the maximum luminosity.

In §4, I studied a model of a neutron star with an optically thick envelope, which is formed by (super-Eddington) accreting material. This work accounted for the tilt of the magnetic moment from the spin axis in the calculation of the velocity of the accreting material and the optical depth of the envelope. I found the synthetic spectrum and pulsed fraction of the envelope model (for particular model parameters) matched the characteristics of the observed spectrum and pulsed fraction of two Pulsating Ultra-luminous X-ray sources, unlike in the case for models of high luminosity amplification from outflows in the disc. These results indicate that further theoretical study, for which this work serves as a foundation, of the optically thick envelope scenario would enable a better understanding of the properties of Pulsating Ultra-luminous X-ray sources.

Research Paper Declaration

UCL Research Paper Declaration Form: referencing the doctoral candidate's own published work(s)

1. **For a research manuscript that has already been published:**

   (a) **What is the title of the manuscript?**
   Super-eddington emission from accreting, highly magnetised neutron stars with a multipolar magnetic field

   (b) **Please include a link to or doi for the work:**
   doi: 10.1093/mnras/stab915

   (c) **Where was the work published?**
   Monthly Notices of the Royal Astronomical Society

   (d) **Who published the work?**
   Oxford University Press

   (e) **When was the work published?**
   June 2021

   (f) **List the manuscript's authors in the order they appear on the publication:**
   Brice, N., Zane, S., Turolla, R., Wu, K.

   (g) **Was the work peer reviewed?**
   Yes

   (h) **Have you retained the copyright?**
   Yes

(i) **Was an earlier form of the manuscript uploaded to a preprint server?**

Yes, doi: 10.48550/arXiv.2104.06138

2. **For multi-authored work, please give a statement of contribution covering all authors:**

I wrote the code for the accretion column model, taking previously written code by Silvia Zane and Roberto Turolla as example for the code to calculate the scattering cross-sections. I wrote the manuscript with editing by Silvia Zane. Roberto Turolla suggested the research project and provided comments for editing. Kinwah Wu provided comments for editing and feedback on the direction of the work.

3. **In which chapter(s) of your thesis can this material be found?**

Chapter 3

e-Signatures confirming that the information above is accurate :

Candidate:

Date:

Supervisor/Senior Author signature (where appropriate)**:**

Date:

UCL Research Paper Declaration Form: referencing the doctoral candidate's own published work(s)

1. **For a research manuscript that has already been published:**

(a) **What is the title of the manuscript?**

Observational properties of accreting neutron stars with an optically thick envelope

(b) **Please include a link to or doi for the work:**

doi: 10.1093/mnras/stad2391

(c) **Where was the work published?**

Monthly Notices of the Royal Astronomical Society

(d) **Who published the work?**

Oxford University Press

(e) **When was the work published?**

November 2023

(f) **List the manuscript's authors in the order they appear on the publication:**

Brice, N., Zane, S., Taverna, R., Turolla, R., Wu, K.

(g) **Was the work peer reviewed?**

Yes

(h) **Have you retained the copyright?**

Yes

(i) **Was an earlier form of the manuscript uploaded to a preprint server?**

No

2. **For multi-authored work, please give a statement of contribution covering all authors:**

I derived the analytical results for the model, with suggestions by Roberto Turolla and Silvia Zane. I wrote the code to calculate the temperature map for the models. Roberto Taverna and Roberto Turolla adapted previously written code to add a thin disc geometry. I modified the code to add emission from the disc. I wrote the manuscript with editing by Silvia Zane. Roberto Taverna and Roberto Turolla provided comments for editing and feedback on the direction of the work. Kinwah Wu provided comments for editing.

3. **In which chapter(s) of your thesis can this material be found?**

Chapter 4

e-Signatures confirming that the information above is accurate :

Candidate:

Date:

Supervisor/Senior Author signature (where appropriate)**:**

Date:

Acknowledgements

Thanks to everyone that supported me along the way! It's been a difficult last bit. First, I would like to thank my supervision team at UCL, Silvia Zane and Kinwah Wu, for their patience in putting up with my scattered approach, especially while getting this thesis to submission. Thanks also to Roberto Turolla and Roberto Taverna for their time and effort in the research projects that made this thesis possible.

There are a lot of other people at MSSL who have had a big impact on my experiences and the direction I'm taking now. Thank you to them for all the good moments. I would like to specifically thank Harry, Chiara, Paul, JingTing, and Jun. Your company while writing this thesis made it a lot easier to get through. Of course, I want to especially thank Ruth for all the support and encouragement.

Finally, but not least, I want to thank all of my family for the support they've given up to this point. Thanks especially to my mum for getting to this point first and making it seem very possible to my younger self. Thanks especially to my dad for the encouragement to submit!

Contents

List of Figures

List of Tables

Chapter 1

Introduction

1.1 Overview

Neutron stars (NSs) present a rich and diverse phenomenology in different messenger-modes: gravitational waves, neutrino emission, and the entirety of the electromagnetic spectrum. Decoding these signals is a crucial step in understanding the properties of NSs but it requires an accurate model to correctly interpret the phenomena. The central aim of this thesis is to contribute in making an accurate model by examining how the magnetic field configuration affects predicted observables.

Of particular interest is the study of X-ray emission, which gives a window into the highly energetic phenomena in the universe. The X-ray emission from NSs offers a unique laboratory to test our most successful quantum field theory - quantum electrodynamics (QED) - in a regime that is otherwise inaccessible to terrestrial experiments. This regime is the strong-field regime of QED, where super-strong magnetic fields affect the properties of plasmas and even the vacuum, changing the behaviour of electromagnetic propagation.

So far, a super-strong magnetic field is associated only with NSs, whose material composition allows for a magnetic field of such magnitude. This magnetic field affects the observables of the X-ray emission: from cyclotron absorption lines to the pulse profiles. In the first place, the magnetic field of a NS is a crucial part of how they are distinguished from their compact-object counterparts: black holes. Although there is a large body of work that investigates the effects of a magnetic

field on the NS environs, many models rely on a simple description of the magnetic field structure, namely as a pure dipole.

In this thesis, the focus of investigation is accreting NSs, and specifically those that exhibit super-Eddington emission. These NSs are in a group of the most luminous persistent X-ray sources, barring active galactic nuclei. They have posed as a problem for using a simple description of the magnetic field structure, especially when giving a self-consistent account of the accretion process - from accretion disc to emission close to the surface. For accreting NSs with super-Eddington emission, many open questions still remain and the physics is far from fully settled. The analysis here is meant to show an example scenario where the magnetic field structure changes the observables.

1.2 Accreting Neutron Stars

A NS in a binary system that accumulates material from its companion star is called an accreting NS. The infalling material is supplied by the companion star, which either ejects material in a stellar wind, or loses material through Roche-lobe overflow (Savonije, 1978). Once captured in the gravitational well of the NS, the infalling material liberates its gravitational energy as radiation. This emission is observed in the X-ray band (Giacconi et al., 1971) and it is the basis for the study of the properties of accreting NSs.

The available gravitational energy per unit mass of infalling material is obtained by integrating the work from moving a unit mass from infinity to the NS surface, where the gravitational potential energy is converted into radiation, i.e.

$$\int_{\infty}^{R} -\frac{GM}{r^2}\mathrm{d}r = \frac{GM}{R_*}, \tag{1.1}$$

where M and R_* are the mass and radius of the NS, respectively. Therefore, for a mass accretion rate $\dot{M}$, the luminosity from accretion is given by

$$L = \frac{GM}{R_*}\dot{M}. \tag{1.2}$$

The observed X-ray luminosity of accreting NSs spans many orders of magnitude: $\sim 10^{32} - 10^{42}$ erg s^{-1}, which indicates a large range of possible mass accretion rates.

In general, there is an upper limit to the possible luminosity, called the Eddington luminosity, because of a back-reaction of the radiation on infalling matter. The Eddington luminosity is calculated from equating the force of gravity acting on the infalling material, with the outgoing radiation pressure on the infalling material, which gives

$$L_{\rm Edd} \approx 1.3 \times 10^{38} \left(\frac{\kappa_{\rm T}}{\kappa}\right) \left(\frac{M}{M_{\odot}}\right) \text{erg s}^{-1}, \tag{1.3}$$

where κ is the scattering opacity of the infalling material, and $\kappa_{\rm T}$ is the Thomson scattering opacity of electrons.

In the scenario of accretion from stellar wind (of the companion star), the accreting material is modelled to infall from all directions, i.e. spherically symmetric infall, onto the NS because of a lack of bulk angular momentum. In the Roche-lobe overflow accretion case, the accreting material has substantial angular momentum and so forms an accretion disc, which mediates the infall (Pringle & Rees, 1972; Shakura & Sunyaev, 1973).

Theoretical study of the X-ray spectra from an accreting NS suggests that the X-ray continuum is seeded by thermal emission from the NS surface, which is heated by the collision of the infalling material with the surface; cyclotron emission; and thermal brehmsstrahlung from the hot infalling material. The seed X-ray spectrum is modified by Compton scattering of the photons by relativistic electrons in the infalling magnetised plasma to produce the final X-ray emission (Basko & Sunyaev, 1975; Becker & Wolff, 2007) that is modelled as a power-law with an exponential cutoff.

There are various observational characteristics from accreting NSs that can be used as a diagnostic of the system, the principal being periodic pulsations (Lamb, 1977; Rappaport & Joss, 1977), which was first discovered from the X-ray sources Centaurus X-3 (Giacconi et al., 1971; Schreier et al., 1972) and Hercules X-1

(Tananbaum et al., 1972). This particular characteristic was the first direct evidence for the existence of accreting NSs. It was quickly shown that the regular, coherent pulsations could be successfully explained using the model of magnetically controlled accretion, developed from the early 1970s onward (Pringle & Rees, 1972; Davidson & Ostriker, 1973; Lamb et al., 1973; Ghosh & Lamb, 1978). In this scenario, the strong ($> 10^{12}$G) NS magnetic field disrupts the flow of the infalling material at the magnetosphere and subsequently channels the accretion flow along magnetic field lines towards the magnetic poles. The gravitational energy of the infalling material is therefore released at the magnetic poles, which results in a hot-spot with an area $A \approx 1\%$ of the total surface. The thermal emission from this area has an effective blackbody temperature

$$T_{\rm eff} \sim 1.7 \left(\frac{L}{L_{\rm Edd}}\right)^{\frac{1}{4}} \left(\frac{A}{10^6 {\rm cm}}\right)^{-\frac{1}{4}} \ {\rm keV}, \tag{1.4}$$

i.e. in X-rays; or if the accretion rate is above a critical rate, the result is an accretion column supported by a radiative shock above the surface (Basko & Sunyaev, 1976), which is discussed in more detail in §3. The footprint of the hot-spot/accretion column on the NS surface depends on the structure of the magnetic field (Rappaport & Joss, 1977). In particular, if the magnetic poles are misaligned with the rotation axis, an observer sees a moving emitting area. [1] Thus, the X-ray emission from an accreting NS has periodic pulsations, occurring with the spin period.

Across all accreting NSs with a periodic pulsation, there is an observable change in the pulse period (Giacconi, 1975; Bildsten et al., 1997). This characteristic can also be explained by the model of magnetically controlled accretion. Namely, the change in the spin period over time is due to a transfer of angular momentum between the accreting material and the NS (Rappaport & Joss, 1977; Ghosh et al., 1977). To produce a secular change in the spin period, there needs to be a transfer of angular momentum along a stable axis and so the accretion is thought to be fed by a disc.

[1] The external magnetic field is thought to be locked in place on the surface, so co-rotates with the NS.

The simplest description of the spin period changes is to assume the disc material moves with a Keplerian velocity and deposits all its excess angular momentum to the NS at the magnetosphere (Pringle & Rees, 1972; Lamb et al., 1973). In this case, for a NS spinning with a frequency $\omega_s = 2\pi/P$, where P is the spin period, the NS has total angular momentum

$$K = \omega_s I, \tag{1.5}$$

where I is the moment of inertia of the NS, the change in angular momentum of the NS is given by

$$\dot{K} = \dot{M}\left(\sqrt{GMR_m} - R_m^2\omega_s\right), \tag{1.6}$$

where R_m is the magnetospheric radius, defined later in §2.1.1.1. This can be related to the change in spin period using the time derivative of equation (1.5) and assuming the moment of inertia is approximately constant, i.e.

$$-2\pi\frac{\dot{P}}{P^2}I = \dot{K} = \dot{M}\left(\sqrt{GMR_m} - R_m^2\frac{2\pi}{P}\right). \tag{1.7}$$

The change in angular momentum, $\dot{L}$, vanishes for the specific period

$$P_{\rm eq} = 2\pi\left(\frac{GM}{R_m^3}\right)^{-\frac{1}{2}}, \tag{1.8}$$

which is called the equilibrium spin period of the accreting NS. In the case where the NS is spinning faster than the equilibrium spin period, the disc material (at the magnetospheric radius) has a lower angular momentum than the NS. Thus, angular momentum is transferred outwards from the NS to the disc material ($\dot{K} < 0$). This moves the disc material to an orbit at a greater distance than R_m, which prevents accretion. This is called the propeller effect (Illarionov & Sunyaev, 1975).

Because the magnetospheric radius can be related to measurements of the spin period, the spin period derivative, and luminosity, attempts have been made to esti-

mate the magnetic field strength from a combination of these observables (e.g. see Erkut et al. 2020). However, the mechanism that drives the disc-magnetosphere interaction (and subsequently a precise quantification for the angular momentum transfer) is unknown, e.g. see Lai (2014) for a review of the different mechanisms that have been studied. This makes an inference of the magnetic field strength from these observables alone uncertain.

A direct measurement of the magnetic field strength local to the hot-spot/accretion column can be made when there is a detection of electron cyclotron resonance features (CRFs) in the X-ray spectrum. CRFs are believed to be absorption lines in the X-ray continuum resulting from resonant scattering of the seed photons through the accreting magnetised plasma near the surface (Staubert et al., 2019). The energy of the CRF is related to the magnetic field strength by

$$E_{\rm cycl} = h\frac{eB}{m_e c} \approx 11.6\, B_{12}\ {\rm keV}, \tag{1.9}$$

where e and m_e is the charge and mass of an electron respectively, and B_{12} is the magnetic field strength in units of 10^{12}G.

The first CRF was serendipitously discovered in the spectrum of Hercules X-1 at an energy of ~ 58 keV (Truemper et al., 1978), which corresponds to a magnetic field strength $\sim 5.0 \times 10^{12}$G for the fundamental harmonic. These magnetic field strengths are expected at the NS surface near the magnetic poles, which gives credence to the theory that the X-ray production is local to the surface rather than farther away in the magnetosphere.

1.3 Super-Eddington Accreting Neutron Stars

Theoretical work in understanding the processes of accreting NSs has also been invigorated by the discovery of pulsating ultra-luminous X-ray sources (PULXs), which are a sub-class of ultra-luminous X-ray sources (ULXs). A comprehensive literature review of the phenomenology of ULXs is available by Kaaret et al. (2017) as well as literature reviews of the theoretical work pertaining to ULXs in general by Fabrika et al. (2021) and ULXs as accreting NSs by Mushtukov & Tsygankov

(2022); King et al. (2023). In this section, I present the relevant background to motivate a study of multi-polar magnetic fields in PULXs.

ULXs are X-ray bright point-like sources, found inside or near the optical extent of a galaxy but outside of the galactic nucleus (to exclude active galactic nuclei among the class members). They are defined by an X-ray luminosity that exceeds 10^{39}erg s^{-1}, which is greater than the Eddington luminosity for stellar mass, $M \sim 1 - 10\ M_{\odot}$, black holes (BHs). The most widely accepted model of ULXs is as a stellar mass black hole undergoing super-critical accretion (Gladstone et al., 2009) (also known as super-Eddington accretion), in contrast to Eddington limited accretion by an intermediate mass ($M \sim 10^2 - 10^4\ M_{\odot}$) BH (Colbert & Mushotzky, 1999), although there are ULXs that exhibit phenomena more readily explainable by the presence of an intermediate mass BH accretor (Kaaret et al., 2017). The super-critical accretion model is supported by high-resolution spectra observations of several ULXs: spectral modelling shows a significant difference in the model parameters for the spectra of galactic sub-critical BH X-ray binaries and the spectra of ULXs (Stobbart et al., 2006; Gladstone et al., 2009); spectroscopic analysis shows a relativistic shift in absorption lines, which indicates the presence of ultra-fast ($v \sim 0.1c$) outflows (Pinto et al., 2016, 2017; Kosec et al., 2018) that are expected in the super-critical accretion mode (Fabrika et al., 2021).

PULXs are a sub-class of ULXs that exhibit a regular, sinusoidal pulsation with a period $\sim$ 1s in their X-ray emission. The pulsations are strongly suggestive of a NS accretor (Bachetti et al., 2014). However, the mechanism by which an accreting NS is able to exceed its Eddington luminosity limit by over two orders of magnitude (Israel et al., 2017a) is still an open question.

Previous theoretical work on the magnetically controlled accretion model for NSs found that a highly-magnetised NS is able to exceed its Eddington luminosity by a factor of several, owing to the geometry of the accretion column (Basko & Sunyaev, 1976). In these models, an optically thick, radiation pressure supported accretion column forms above the NS surface (because the accretion rate is above the critical rate in these cases). The radiation primarily escapes perpendicular to

the infall direction after multiple scatterings in the accretion column. This escape direction is due to the accretion column being geometrically thinner perpendicular to the magnetic field lines than parallel to the magnetic field lines. However, the effect of the geometry of an accretion column from a dipole magnetic field topology alone is unable to account for the observed luminosities in PULXs.

A more recent calculation on the maximum luminosity by Mushtukov et al. (2015) includes the opacity reduction from an ultra-strong magnetic field ($>10^{14}$G), which results in a lower optical depth of the accretion column parallel to the magnetic field lines. This effect, coupled with the geometry of the accretion column does allow for luminosities up to 10^{41}erg s^{-1}. However, another problem arises for the PULXs with the highest luminosities, such as NGC5907 ULX-1 (Israel et al., 2017a) when the magnetic field is assumed to be a pure dipole (which is done by all previous models examining the maximum luminosity). The co-rotating, ultra-strong dipole magnetic field of the NS should prevent accretion altogether because of a centrifugal barrier (Illarionov & Sunyaev, 1975; Stella et al., 1986; Tsygankov et al., 2016), i.e. the propeller effect. The proposed solution of a more complex magnetic field topology (Israel et al., 2017a) is one of the areas of investigation of this thesis, discussed in §3.

The magnetic field structure determines the geometry of the accreting NS system, which itself has effects on the emission properties. Previous works on constructing a model of accreting NS systems assumes a pure dipole magnetic field topology for simplicity (e.g. see Basko & Sunyaev 1976). This assumption is suitable for studying the effects of the magnetic field at large distances from the NS because of the steeper fall-off in strength of higher-order multipole components. However, at distances closer to the NS surface, the higher-order multipole components can dominate and the assumption of a pure dipole field will change the interpretation of observables because of differences in the topology and magnetic field strength of each component.

For example, in models of the surface emission of X-ray dim, isolated NSs (XDINs), the presence of higher-order multipole components has been shown to

affect the light curves (Page & Sarmiento, 1996; Zane & Turolla, 2006). In general, the emission is expected to be contingent on the magnetic field structure. In fact, suggestions of a more complex magnetic field topology than a pure dipole were already made for several sources from the initial analysis of the pulse profiles (Rappaport & Joss, 1977). This points to a need for a systematic analysis in accreting NSs of how different magnetic field structures influence the emission properties.

Chapter 2

Background

2.1 Magnetic Field Structure

A self-consistent description of the magnetic field of a NS, generated by processes in the core and crust, is still an open question (Spruit, 2008). For the purposes of the investigation of this thesis, where the focus is on a systematic analysis of the effects of different magnetic field structures, no attempt is made to derive the magnetic field structure from physical principles. Instead, I treat the magnetic field external to the NS, $\vec{B}$, as a static, current-free magnetic field, which satisfies

$$\nabla \times \vec{B} = \vec{0}. \tag{2.1}$$

In general, an irrotational vector field can be written as the gradient of a scalar field, hence in this case

$$\vec{B} = -\nabla \psi, \tag{2.2}$$

where ψ is the magnetic potential.

The divergence-free condition for the magnetic field becomes a condition that the Laplacian of the magnetic potential vanishes, i.e.

$$\nabla^2 \psi = 0. \tag{2.3}$$

In a spherical coordinate system (r, θ, φ), where r is the radial coordinate, θ is the colatitude coordinate, φ is the longitude coordinate, the general solution to equation (2.3) is a sum of the spherical harmonics, which takes the form

$$\psi(r, \theta, \varphi) = \sum_{\ell,m} \frac{C_{\ell,m}}{r^{\ell+1}} P_\ell^m(\cos\theta) e^{im\varphi}, \tag{2.4}$$

where ℓ is the degree of the (multi-)pole; m is an integer in the range $-\ell \leq m \leq \ell$; $C_{\ell,m}$ is a constant coefficient; and P_ℓ^m is the associated Legendre polynomial of degree ℓ and order m, satisfying the general Legendre equation

$$\frac{\mathrm{d}}{\mathrm{d}\mu}\left[(1-x^2)\frac{\mathrm{d}}{\mathrm{d}\mu}P_\ell^m(\mu)\right] + \left[\ell(\ell+1) - \frac{m^2}{(1-x^2)}\right] P_\ell^m(\mu) = 0, \tag{2.5}$$

where $\mu = \cos\theta$. Solutions of order $m = 0$ result in an axisymmetric magnetic field, which are referred to in the literature as purely poloidal magnetic fields. In fact, the axis of symmetry is the magnetic moment, which is aligned along the zenith ($\theta = 0$) in the spherical coordinate system.

In general, the magnetic field can be decomposed into its poloidal and toroidal components, where the poloidal components are axisymmetric about the magnetic moment, i.e. they have $B_\varphi = 0$. In this thesis, I focus on the effects of the poloidal components and the tilt of the magnetic moment with respect to the rotation axis. The effects of a toroidal component are not examined. These effects have been studied for the light curves from the surface emission of magnetars (Pavan et al., 2009), and on the polarization observables from the surface emission of cooling NSs (Taverna et al., 2015), albeit where the toroidal component is represented by a global twist to the poloidal component rather than as an expansion in terms of the spherical harmonics.

An expression for the magnetic field vector of each poloidal component can be obtained from the general spherical harmonic solutions (2.4) by setting $m = 0$. The degree ℓ poloidal potential is

$$\frac{1}{r^{\ell+1}} P_\ell^0(\mu), \tag{2.6}$$

where P_ℓ^0 can be found by solving equation (2.5). For reference, the Legendre polynomials for the degree $0,1,2,3$ poloidal components, i.e. the monopole, dipole, quadrupole, octupole components respectively, are given in table 2.1.

ℓ	$P_\ell^0(\cos\theta)$
0	1
1	$\cos\theta$
2	$\frac{1}{2}(3\cos^2\theta - 1)$
3	$\frac{1}{2}(5\cos^3\theta - 3\cos\theta)$

Table 2.1: The Legendre polynomials of order 0 up to degree 3, corresponding to the angular part of the monopole, dipole, quadrupole, and octupole.

In the spherical coordinate system, the poloidal magentic field components are given by

$$B_r = \sum_\ell (\ell+1)\frac{C_{\ell,0}}{r^{\ell+2}} P_\ell^0(\mu),$$
$$B_\theta = -\sum_\ell \frac{C_{\ell,0}}{r^{\ell+2}} \sin\theta \partial_\mu P_\ell^0(\mu), \tag{2.7}$$

where $\vec{B} = B_r\hat{r} + B_\theta\hat{\theta}$. The coefficients for each poloidal component can be related to the magnetic field strength on the surface (at the magnetic pole where $\theta = 0$) of the degree ℓ poloidal component, $B_{\text{pole},\ell}$, by

$$C_{\ell,0} = \frac{R_*^{\ell+2}}{(\ell+1)} B_{\text{pole},\ell}, \tag{2.8}$$

where R_* is the radial distance of the NS surface from the centre. This allows for an easy comparison between the relative strengths of the poloidal components in the total magnetic field. In the following, the ratio between a higher-degree poloidal component strength with the dipole component strength, at a distance R_* and at the pole $\theta = 0$, is denoted by Γ.

2.1.1 Magnetic Field Lines

Infalling material, moving with a velocity $\vec{v}$, interacts with the NS magnetic field, $\vec{B}$, through the Lorentz force, $\vec{F} = q\vec{v} \times \vec{B}$, where q is the charge of the species. The

infalling material can be treated in bulk as a plasma fluid and a fluid pressure can be calculated.

The interaction regimes are typically separated: at distances far from the NS, outside of the magnetosphere, where the influence of the NS magnetic field on the dynamics of the infalling material is negligible; at distances close to the NS, inside the magnetosphere, where the magnetic field channels the accretion flow along magnetic field lines. The characteristic distance for the separation of the two regimes is the magnetospheric radius.

At distances closer than the magnetospheric radius, the magnetic pressure dominates over the fluid pressure of the accreting material and so the fluid flows along the magnetic field lines. In this regime, $\vec{v}$ is parallel to the magnetic field direction and so the Lorentz force vanishes. This is the so-called force-free magnetic field approximation.

Because the accretion flow follows the magnetic field lines, their shape determines the geometry of the accreting NS system. Thus, a treatment of the magnetic field lines is required to understand the effects of different magnetic field structures in the magnetically controlled accretion scenario. I lay out a method for this treatment in the following, extending from previous works on the construction of coordinate systems for magnetically controlled accretion by Canalle et al. (2005); Adams & Gregory (2012).

The magnetic field lines are 1-dimensional paths in $\mathbb{R}^3$, where $\vec{B}$ is tangent at every point along the path. This means that the iso-surfaces (in 3D) of the magnetic potential are perpendicular to the magnetic field lines. In general, the magnetic field lines can be constructed from a scalar field q with iso-surfaces perpendicular to the iso-surfaces of ψ so that

$$\nabla\psi \cdot \nabla q = 0. \tag{2.9}$$

Because the iso-surfaces of ψ are a 2-dimensional surface, there is still a degree of freedom in the choice of q, namely the vector field $f\hat{\varphi}$ satisfies (2.9) for a function $f(r,\theta)$, in place of ∇q. By requiring that the vector field ∇q is also perpendicular

to $f\hat{\varphi}$, q can be found from solving the partial differential equations in the vector equation

$$\nabla q = f \nabla \psi \times \hat{\varphi}. \tag{2.10}$$

This results in a scalar field q whose isoclines are the magnetic field lines.

In spherical coordinates, solving equation (2.10) in $\hat{r}$ yields the scalar field

$$q = R_*^2 \sin^2\theta \sum_\ell \frac{1}{\ell(\ell+1)} \left(\frac{R_*}{r}\right)^\ell B_{\text{pole},\ell}\, \partial_\mu P_\ell^0(\mu), \tag{2.11}$$

which can be verified to satisfy the other partial differential equation in $\hat{\theta}$ in equation (2.10) using the fact that the associated Legendre polynomial satisfies the general Legendre equation (2.5). A set of points for a magnetic field line is determined by solving for all points with a constant value of q.

The scalar function q also captures information on the local (magnetic) polarity of the magnetic field. This can be understood by considering the magnetic field in the associated spherical coordinate system. Namely, at certain θ intervals, the polarity can be reversed from that close to the pole at $\theta = 0$. This is true for higher degree poloidal components than a pure dipole. Thus, in order to find all the magnetic field lines that reach out to some maximum radial distance r, it is necessary to consider the values $\pm q$. From the ordering choice in the cross-product in equation (2.10), $q > 0$ everywhere for the pure dipole magnetic field.

Using the framework developed, it is possible to calculate the geometry of an accreting NS system with an arbitrarily complex (poloidal) magnetic field configuration. In the following, I calculate some of the geometric quantities in the pure dipole magnetic field case and I show the difference in the multi-pole (up to octupole) magnetic field case.

2.1.1.1 Magnetospheric Radius

The magnetospheric radius is the characteristic length scale that delineates the region where the magnetic force dominates the accretion flow dynamics from the

region where the magnetic force is negligible to the overall accretion flow dynamics. The physics of the disc-magnetosphere interaction are not well understood, and there are several approaches for calculating the magnetospheric radius, namely through a balance of the magnetic field energy, stress, or pressure with the disc material energy, stress, or pressure respectively (Ghosh & Lamb, 1979).

Each of the calculation methods gives a magnetospheric radius of the order of the Alven radius. This is the distance at which the magnetic energy density is equal to the kinetic energy density of free-falling material (not material accreting from an accretion disc). The magnetic energy density is given by

$$\frac{\vec{B}\cdot\vec{B}}{8\pi} = \frac{1}{8\pi}\nabla\psi\cdot\nabla\psi, \tag{2.12}$$

which for a pure dipole magnetic field evaluates to

$$\frac{1}{8\pi}\left(\frac{B_{\rm pole}R_*^3}{r^3}\right)^2\frac{1}{4}\left(1+3\cos^2\theta\right). \tag{2.13}$$

The kinetic energy density of the free-falling material, assuming radial free-fall and conservation of mass in a spherically symmetric infall, is given by

$$v \sim v_{\rm ff} = \left(\frac{2GM}{r}\right)^{1/2}, \tag{2.14}$$

$$|\rho v| = \frac{\dot{M}}{4\pi r^2}. \tag{2.15}$$

In the case of a pure dipole magnetic field, equating the magnetic energy density with the kinetic energy density of the infalling material at a radius $r = R_A$ and colatitude $\theta = \pi/2$ gives

$$\begin{aligned} R_A &= (128G)^{-1/7}M^{-1/7}B_{\rm pole}^{4/7}\dot{M}^{-2/7}R_*^{12/7} \\ &\approx 9\times10^7\left(\frac{B_{\rm pole}}{10^{12}{\rm G}}\right)^{4/7}\dot{m}^{-2/7}m^{-1/7}r_6^{12/7}\ {\rm cm}, \end{aligned} \tag{2.16}$$

where in the second line $\dot{m} = \dot{M}/\dot{M}_{\rm Edd}$ is the fraction of the mass accretion rate to

the Eddington mass accretion rate, $m = M/1.4M_{\odot}$, and $r_6 = R_*/10^6$cm.

The magnetospheric radius is estimated from the Alven radius as

$$R_m = \Lambda R_A, \tag{2.17}$$

where Λ is a dimensionless parameter that accounts for the accretion mode, in particular $\Lambda = 1$ for wind-fed accretion and $\Lambda \approx 0.5$ for disc-fed accretion (Ghosh & Lamb, 1978).

For a higher degree poloidal magnetic field with a single dominant component, the Alven radius can be given as a closed form solution similar to equation (2.16). This time, the magnetic energy density can be evaluated at a θ value corresponding to the weakest point of the magnetic field for the particular poloidal component (to match the definition for the Alven radius in the pure dipole case). For example, in the case of the pure quadrupole field, the weakest point of the magnetic field is at $\theta = \pi/3$ (and $\theta = 2\pi/3$ by symmetry). Thus, the magnetospheric radius is given by

$$\begin{aligned} R_m &= \Lambda(128G)^{-1/11} M^{-1/11} B_{\rm pole}^{4/11} \dot{M}^{-2/11} R_*^{16/11} \\ &\approx 2\times 10^7 \Lambda \left(\frac{B_{\rm pole}}{10^{12}{\rm G}}\right)^{4/11} \dot{m}^{-2/11} m^{-1/11} r_6^{16/11} \text{ cm}. \end{aligned} \tag{2.18}$$

On the other hand, a multi-polar magnetic field does not provide a simple closed form solution because the magnetic energy density has radial terms of different order. Instead, the Alven radius must be computed numerically. However, because the contribution to the magnetic energy density decays at a much higher rate for higher degree poloidal components, i.e. going at least as $r^{-2(\ell+2)}$ for a degree ℓ poloidal component, equation (2.16) remains a good approximation for all magnetic field configurations (with a dipole component) and mass accretion rates considered in this thesis.

2.1.1.2 Footprint of the Hot-Spot and Accretion Column

The hot-spot and accretion column are structures that result from the release of gravitational potential energy by the infalling material close to the NS surface. The location and dimensions of these structures depend on the footprint (on the NS surface) of the magnetic field lines that confine the accretion flow. For wind-fed accretion, the hot-spot/accretion column is an axially symmetric filled funnel about the magnetic pole because accretion occurs spherically until the flow is redirected by the magnetosphere. Thus, the hot-spot/accretion column is confined by the magnetospheric magnetic field lines only, i.e. magnetic field lines that reach out to $r = R_m$ at $\theta = \pi/2$. For the disc-fed accretion, the hot-spot/accretion column is an axially symmetric filled ring about the magnetic pole because accretion occurs only along the plane of the disc until the infalling material is loaded onto magnetic field lines at the disc-magnetosphere boundary, which is a region of finite width (Ghosh & Lamb, 1979). The hot-spot/accretion column is confined between the magnetospheric magnetic field lines (the outer edge of the boundary region) and the magnetic field lines at the inner edge of the boundary region, i.e. magnetic field lines that reach out to $R_m - \delta$ at $\theta = \pi/2$, where δ is the finite width of the boundary region.

Every point - including the footprint point - of the magnetospheric magnetic field lines and of the boundary region magnetic field lines can be found from equation (2.11). The calculation is done by first finding the corresponding value of q for each magnetic field line, which can be uniquely determined from a single known point that the magnetic field line passes through. This known point is at the magnetospheric radius or boundary region, i.e. $r = R_m$ (and $r = R_m - \delta$), $\theta = \pi/2$.

For a pure dipole magnetic field topology, the scalar field q is given by

$$q = R_*^2 \sin^2\theta \frac{1}{2}\left(\frac{R_*}{r}\right) B_{\text{pole}}, \tag{2.19}$$

which - after substituting for the value of q at $r = R_m,\ \theta = \pi/2$ - can be written as

$$\left(\frac{r}{R_m}\right) = \sin^2\theta. \tag{2.20}$$

Therefore, the colatitude at which the magnetic field line meets the surface, θ_*, is given by

$$\mu_* = \pm\left[1 - \frac{R_*}{R_m}\right]^{1/2}, \tag{2.21}$$

where $\mu_* = \cos\theta_*$. The positive and negative value of μ_* is the cosine of the colatitude of the footprint closest to the pole at $\theta = 0$ and $\theta = \pi$ respectively. The area of the hot-spot/accretion column footprint (closest to the pole at $\theta = 0$ explicitly but by symmetry equal to the area of the other hot-spot/accretion column footprint) is subsequently calculated by integrating between the bounding magnetic field lines, giving

$$\begin{aligned} S_{\rm W} &= R_*^2 \int_{\varphi=0}^{\varphi=2\pi} \mathrm{d}\varphi \int_{\mu=1}^{\mu=\mu_*} \mathrm{d}\mu \\ &= 2\pi R_*^2 \left[1 - \mu_*\right] \approx \pi R_*^2 \left(\frac{R_*}{R_m}\right), \end{aligned} \tag{2.22}$$

$$\begin{aligned} S_{\rm D} &= R_*^2 \int_{\varphi=0}^{\varphi=2\pi} \mathrm{d}\varphi \int_{\mu=\mu_{\rm I}}^{\mu=\mu_*} \mathrm{d}\mu \\ &= 2\pi R_*^2 \left[\mu_{\rm I} - \mu_*\right] \approx \pi R_*^2 \left(\frac{R_*}{R_m}\right)\left(\frac{\delta}{R_m}\right), \end{aligned} \tag{2.23}$$

where $\mu_{\rm I}$ is the cosine of the colatitude at which the magnetic field line from the inner part of the boundary region meets the surface, i.e.

$$\mu_{\rm I} = \left[1 - \frac{R_*}{r_m - \delta}\right]^{1/2}, \tag{2.24}$$

and the approximations are made in the limit where $r_m \gg R_*,\ r_m \gg \delta$.

For a multi-polar magnetic field topology, the scalar field q is a sum of different orders of R_*/r, which means there is no closed form function as in equation (2.20). The value of μ_* must be computed numerically. Unlike in the calculation of the

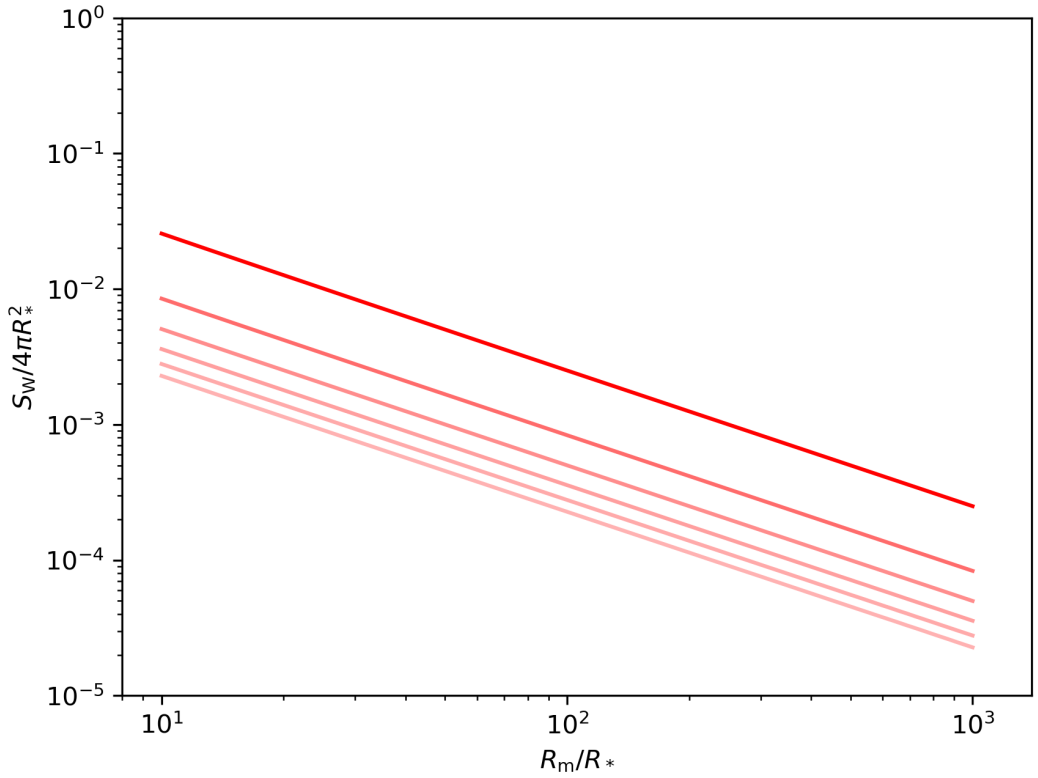

Figure 2.1: S_W, for the pole at $\theta = 0$, as a fraction of the total NS surface area against various magnetospheric radii, R_m, for magnetic fields made up of a dipole component plus quadrupole component. The ratio of the strengths of the quadrupole to dipole components is given by $\Gamma = B_{\text{quad}}/B_{\text{dip}}$. The red lines from top to bottom progressively show the fraction of surface area for magnetic fields with $\Gamma = 0,\ 2,\ 4,\ 6,\ 8,\ 10$.

magnetospheric radius in the multipole case, the pure dipole solution (2.21) is not a good approximation. This can be seen in the figure below, where a comparison is made between the footprint area of the magnetic field lines, which channel material to the pole at $\theta = 0$, of the pure dipole magnetic field with the footprint area of the same magnetic field lines of multi-polar magnetic fields (in this case made up of a dipole component plus quadrupole component).

The picture is further complicated for material channelled to the other poles of a multi-polar magnetic field because the magnetic scalar potential is not necessarily symmetric for θ reflected about $\theta = \pi/2$. In the case of a multi-polar field made up of a dipole component plus quadrupole component, there is an additional pole (which is a ring at the equator from the quadrupole component) that changes the

shape of the footprint of the channelling magnetic field lines. In the following, I discuss the effect in the case of spherical (wind-fed) accretion first to exemplify the additional considerations required to calculate the footprint accurately and then the effect in the case of disc-fed accretion.

For spherical accretion, the accreting material falls radially towards the NS and is deflected from a radial infall by the magnetic field. An example diagram of this is shown in figure 2.2, where the multi-polar field is made up of a dipole component plus quadrupole component. It is possible for the magnetosphere to be made up of non-contiguous regions, which means there are additional magnetospheric radii that apply for infall trajectories from a select subset of the whole domain of θ. This occurs when there is a region outside of the NS surface that is dominated by a higher degree poloidal component than the far field (as $r \to \infty$). For example, a magnetic field with a dipole component plus quadrupole component has an additional quadrupole dominated magnetospheric radius given by equation (2.18), which applies for infall trajectories that start at θ close to $\theta = \pi$, specifically for θ satisfying

$$\cos(\pi - \theta) > \frac{B_{\rm dip}}{B_{\rm quad}} \tag{2.25}$$

which is obtained from solving for the values of θ when $q = 0$ and $r > R_*$.

The magnetic field line that bounds this region of the magnetosphere can be determined using the same method as for the pure dipole case and for the magnetic field lines that connect to the pole at $\theta = 0$ in the multi-polar case, in particular by finding a point at which the magnetospheric field line passes through: $(r, \theta) = (R_m, 2\pi/3)$, and evaluating the corresponding value of q. The footprint of the magnetospheric field line is subsequently given by (R_*, θ_*), where $\mu_* = \cos\theta_*$ is computed numerically. The area of each hot-spot/accretion column footprint is calculated by integrating between the footprint on the surface of the bounding magnetic field lines, as before.

In the disc-fed case, the problem of determining the hot-spot and accretion column footprint is made more complicated by the magnetic field null points, where

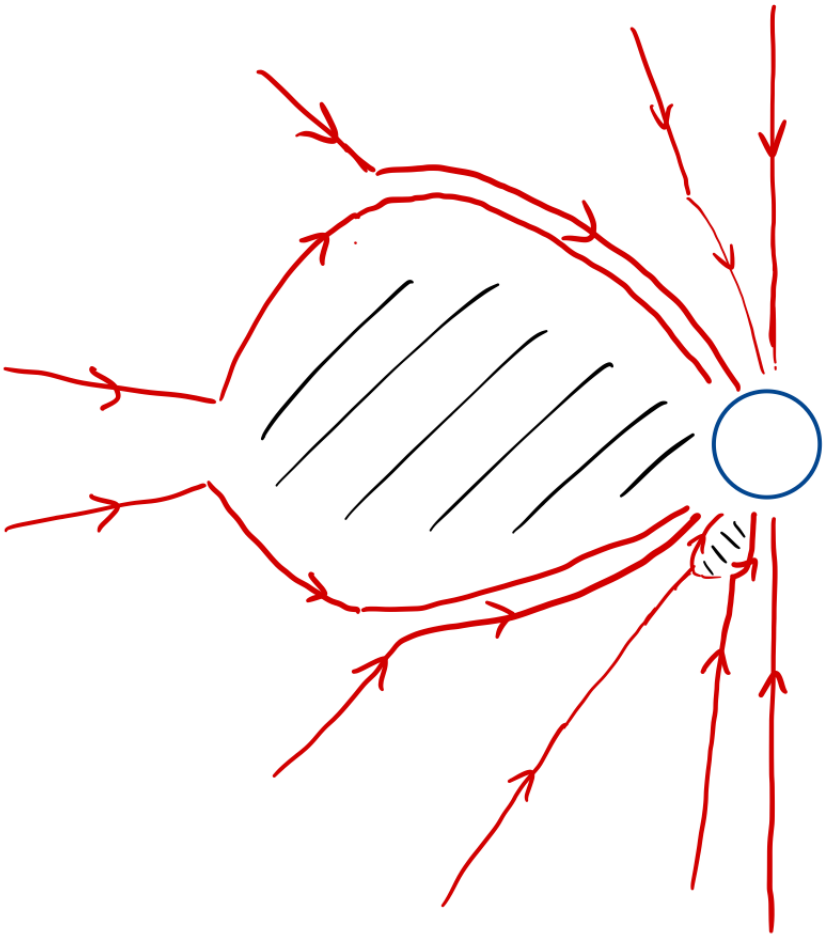

Figure 2.2: A 2 dimensional diagram for the trajectories of (initially radially) infalling charges in the presence of a multi-polar (dipole plus quadrupole) magnetic field. The diagram shows the trajectories in one slice of constant φ for the accreting NS system, the entire surface of trajectories follow from axial symmetry. The red solid lines with arrows show the trajectories of the charges. The black shaded region shows the interior of the magnetosphere, where the magnetic field energy is strong enough to completely deflect all trajectories. The blue circle shows the surface of the NS.

$\vec{B} = \vec{0}$. This means that the magnetic energy density is no longer monotonically increasing while approaching the surface along the field lines. Therefore, it is possible for the kinetic energy density of the infalling material to become larger than the magnetic energy density along the path of a magnetic field line. At this point, the force free approximation breaks down and it may be the case that the infalling material spreads until reaching a region where the magnetic energy density is greater than its kinetic energy density, where it is loaded onto the field lines again. Further work is needed to determine the density distribution of the material among the hot-spots / accretion columns for a multi-polar magnetic field configuration in general.

When the dominant contributions of the multi-polar magnetic field (at the NS surface) are from a dipole degree poloidal component and an additional higher degree poloidal component, which has a pole of the same polarity at $\theta = \pi$ as the dipole component, e.g. a multi-polar magnetic field made up of a dipole component plus octupole component, the calculation of the hot-spot / accretion column footprint is made almost as simple as the pure dipole magnetic field case. For this to be the case, the dipole magnetic field must be sufficiently strong to be the dominating component at the magnetospheric radius. Otherwise, the additional poles introduced by the higher degree poloidal component have to also be taken into account. In the calculation of the accretion column footprint in §3, the magnetic fields satisfy this requirement and so the additional poles introduced by the higher degree poloidal component can safely be ignored for the purposes of calculating the total footprint area.

The difference in the area of the footprint can significantly influence the emission properties. For example, a basic first approximation of the the hot-spot effective temperature can be obtained from the accretion luminosity, using equation (1.4). A change in the area by an order of magnitude, which is possible for $\Gamma \geq 10$, results in a change to temperature of the hot-spot by a factor ~ 2. This can significantly change values of system properties that are inferred from spectral modelling, e.g. the inferred accretion rate. In §3, I show that accounting for the higher degree multipole components changes the accretion column geometry significantly (by an order

of magnitude).

2.1.1.3 Cross-Sectional Area of the Accretion Column

Another geometric quantity that has effects on the properties of the accretion flow and emission, especially in the disc-fed case, is the change in the cross-sectional area of the channelling magnetic field lines. The geometric compression of the accretion flow space is responsible for some heating of the infalling material (Canalle et al., 2005) and changes to the density that affect the radiation transport, which is discussed in more detail in §3. This effect is important particularly when there is an accretion column above the surface because in this case the infalling material releases some of its heat above the surface.

Canalle et al. (2005) quantify the geometric compression with the $\mathscr{H}$-function, which is given by

$$\mathscr{H} = \partial_{\psi} \left[\log h_q h_{\varphi} \right], \tag{2.26}$$

where $h_{\psi},\ h_q,\ h_{\varphi}$ are the metric elements for (ψ, q, φ) coordinates. The metric elements $h_{\psi},\ h_q$ can be expressed as

$$h_{\psi} = \frac{1}{|\nabla \psi|},\ \ h_q = \frac{1}{|\nabla q|}, \tag{2.27}$$

which was implicitly given by Adams & Gregory (2012). This can be more easily computed from the definition of the magnetic potential, ψ, and the scalar field, q, that defines a magnetic field topology.

The $\mathscr{H}$-function is directly used in the mass-continuity equation, namely since

$$\partial_{\psi} \left[\rho v \right] = -\mathscr{H}, \tag{2.28}$$

when using the definitions of the curvilinear coordinates by Canalle et al. (2005). Example values of the $\mathscr{H}$-function, for various fixed colatitude angles, are shown in figure 2.3.

Alternatively, an approximation of the geometric compression can be made

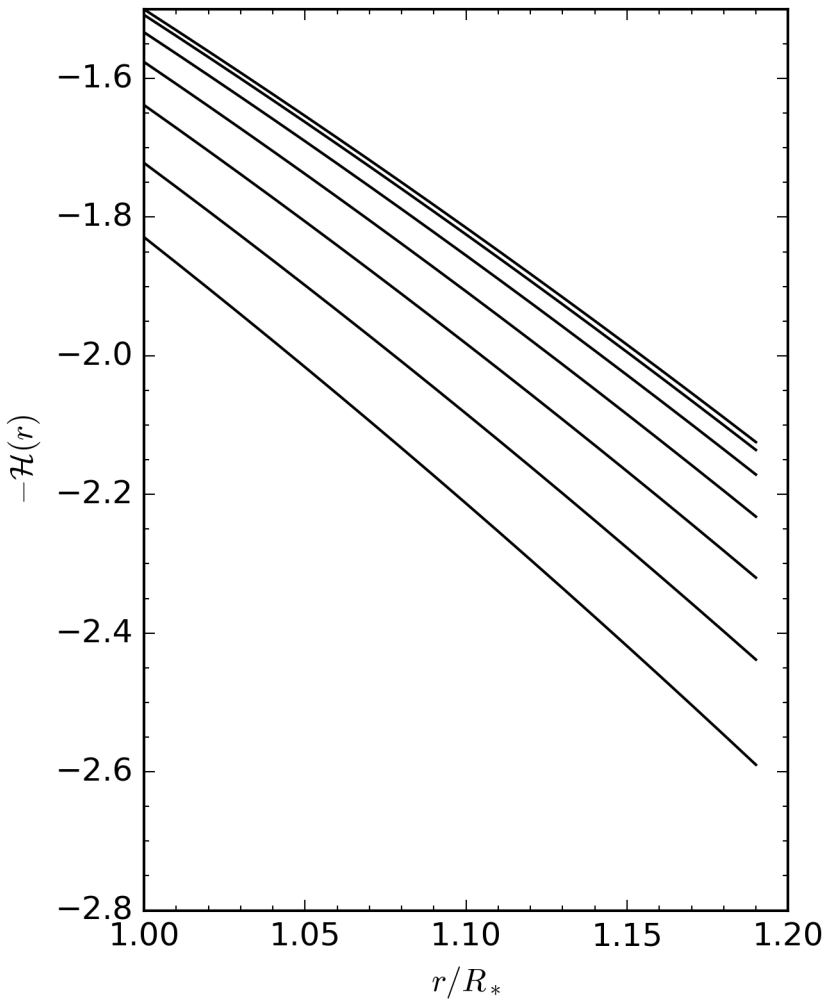

Figure 2.3: The $\mathscr{H}$-function as a function of the radial coordinate. The $\mathscr{H}$-function is plot for various initial colatitudes on the surface. The lines, from top to bottom, correspond to an initial angle of $\theta_0 = 1^\circ,\ 6^\circ,\ 12^\circ,\ 18^\circ,\ 24^\circ,\ 30^\circ,\ 36^\circ$.

by recalculating the accretion column area for various heights above the surface, i.e. $S_D = S_D(h)$. This method is used in §3 (because I didn't know about the $\mathscr{H}$-function when I wrote the paper). The $\mathscr{H}$-function definition can be related directly to this alternative approximate method but I leave this for a future work.

2.2 Radiative Transfer

The theory of radiative transfer provides a framework for decoding the information from the electromagnetic emission of an accreting NS. In particular, the equations of radiative transfer connect the microphysics responsible for the generation and prop-

agation of the X-ray radiation in the vicinity of a NS to the observable phenomena through a statistical description of the interaction processes.

The radiative transfer equations are a particular application of the collisional Boltzmann transport equation, where the phase-space density function is the so-called monochromatic specific intensity $I_j(\nu)$. The specific intensity, $I_j(\nu,\vec{x},\hat{k},t)$, can be understood to be the density of photons (up to a constant factor) of a particular quantum state (here with frequency ν and propagation direction $\hat{k}$) at a position $\vec{x}$ and at a time t (Meszaros, 1992). It is related to the energy $\mathrm{d}E_\nu$ passing through an area $\mathrm{d}A$ with unit normal $\hat{n}$, along a direction $\hat{k}$ within a solid angle $\mathrm{d}\Omega$ of the direction, in a time $\mathrm{d}t$, by

$$\mathrm{d}E_\nu = I_j(\nu,\hat{k},\vec{x},t)\ \hat{k}\cdot\hat{n}\ \mathrm{d}A\ \mathrm{d}\Omega\ \mathrm{d}t. \tag{2.29}$$

The geometry is often pictorially represented as in figure 2.4.

In general, the radiative transfer equations gives the change in intensity of a light beam along a path due to absorption, emission, and scattering processes, i.e due to interactions with charges. From the intensity, the other properties of the radiation field, e.g. energy density, flux, and radiation pressure, can be obtained. Hence, an understanding of how the absorption, emission, and scattering processes affect the intensity is needed to quantify the changes in the properties of the radiation field as it propagates to the observation point.

The X-ray radiation generated from accretion typically interacts with the infalling material (and is subsequently modified by the interaction) before escaping the vicinity of the NS (and hence detected by X-ray telescopes). This occurs due to the geometry of the emission region, in particular a hot-spot is exactly at the footprint of the channelled accreting material so the radiation must pass through in order to escape, and an accretion column is supported vertically above the surface exactly by the locally released radiation from the infalling material.

In the following, I lay out an overview of the analysis of light propagation in a magnetised plasma before returning to the calculation of the radiation field properties through the transport equations. A more detailed treatment of each topic

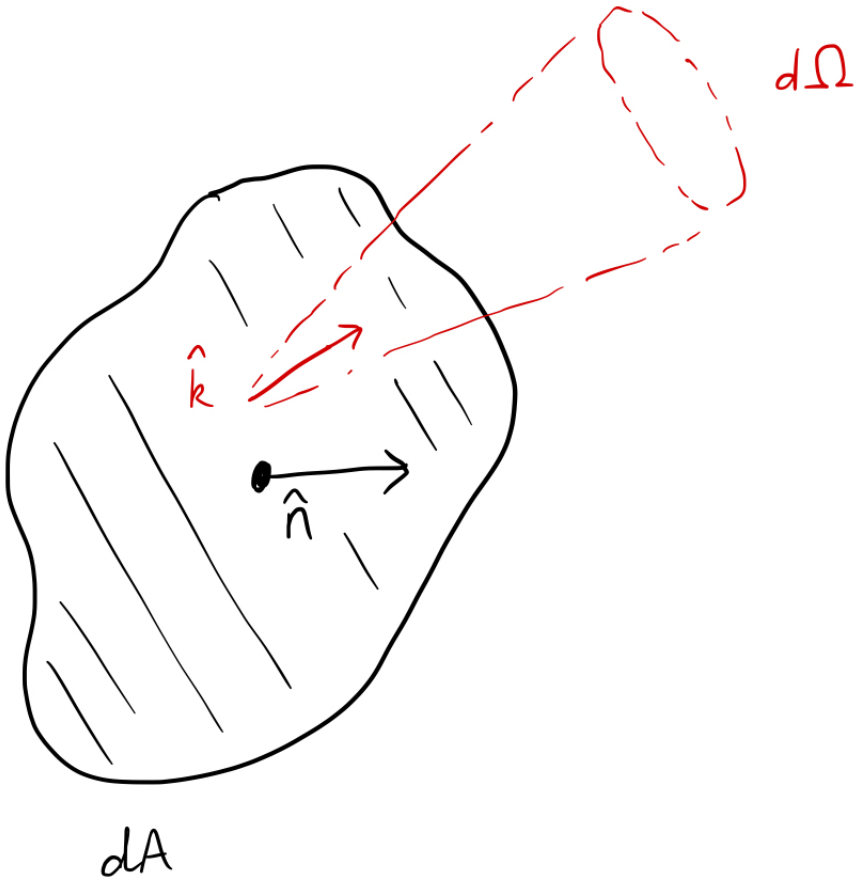

Figure 2.4: A diagram illustrating each of the geometrical components of the relationship between the differential energy $\mathrm{d}E_\nu$ and the specific intensity $I_j(\nu)$. The black shaded region shows a differential area $\mathrm{d}A$ with unit normal $\hat{n}$. The red arrow indicates the radiation intensity unit direction $\hat{k}$ with the cone making a solid angle of $\mathrm{d}\Omega$ around the unit direction. The base of the $\hat{k}$ vector is not coincident with the base of the $\hat{n}$ vector to show that they are affine.

and other topics not covered here can be found in textbooks, e.g. Meszaros (1992). For this thesis, I present the ideas that lead directly to the calculation of the energy, flux, and radiation pressure for a cold, magnetised, dielectric plasma in the optically thick case, i.e. using the Rosseland mean opacity, for the classical regime, starting from the basic Maxwell equations in vacuum. In §3, I discuss modifications to the classical treatment.

2.2.1 Physics of Light Propagation in Magnetised Plasmas

The effects of the properties of the infalling material, which is modelled as a magnetised (dielectric) plasma due to the high magnetic field strengths ($> 10^{12}$G) close the NS surface, on the propagation of electromagnetic waves can be understood by contrasting to the propagation of the electromagnetic waves in a classical isotropic vacuum. In a classical isotropic vacuum, the electromagnetic field is governed by the sourceless microscopic Maxwell equations, which are given by

$$\begin{aligned} \nabla \cdot \vec{E} &= \vec{0}, \\ \nabla \cdot \vec{B} &= \vec{0}, \\ \nabla \times \vec{E} &= -\partial_t \vec{B}, \\ \nabla \times \mu_0^{-1} \vec{B} &= \partial_t \varepsilon_0 \vec{E}, \end{aligned} \tag{2.30}$$

where ε_0 is the vacuum electric permittivity, and μ_0 is the vacuum magnetic permeability. The electric component of the well-known propagating (in vacuum) wave solution to the sourcless microscopic Maxwell equations is given by

$$\vec{E} = \vec{E}_0 \, e^{i(\vec{k}\cdot\vec{x} - \omega t)}, \tag{2.31}$$

where $\vec{k}$ is the propagation direction, $c^2 = (\varepsilon_0 \mu_0)^{-1}$, and $\vec{E}_0$ is a constant vector that describes the plane of oscillation of the electric field, i.e. the polarization state of the wave. The corresponding magnetic component can be obtained from the third

of equations (2.30), giving

$$\vec{B} = \vec{E}_0 \times \hat{k} \frac{1}{\omega} e^{i(\vec{k}\cdot\vec{x} - \omega t)}. \tag{2.32}$$

Thus, the polarization state of an electromagnetic wave is uniquely determined from the electric field oscillation and the propagation direction.

The first of equations (2.30) gives a condition on the possible polarization states, namely

$$\vec{k} \cdot \vec{E}_0 = 0, \tag{2.33}$$

i.e. the polarization is perpendicular to the propagation direction.

The dispersion relation, which gives the speed of the wave propagation through the medium, is obtained from the Fourier transformed latter two equations of (2.30), giving

$$\frac{c^2}{\omega^2} \vec{k} \times \left(\vec{k} \times \vec{E} \right) + \vec{E}_0 = 0. \tag{2.34}$$

The triple cross-product term can be rewritten as

$$N^2 \left[I - \hat{k}\hat{k} \right] \cdot \vec{E}_0, \tag{2.35}$$

where $N^2 = k^2 c^2 / \omega^2$ is the refractive index, $\vec{k} = k\hat{k}$, $\hat{k}\hat{k}$ is a rank $(0,2)$-tensor over the vector space of $\hat{k}$ (and $\vec{E}$), and I is the rank $(0,2)$ identity tensor (over the same vector space). This gives a reformulation of the dispersion relation, in particular

$$\left(I - N^2 \left[I - \hat{k}\hat{k} \right] \right) \cdot \vec{E}_0 = \vec{0}, \tag{2.36}$$

where $\vec{0}$ is the zero vector. This reformulation makes simpler a contrast with the rewritten formulation of the dispersion relation for a wave propagating in a cold, magnetised (dielectric) plasma, provided later.

In a medium that responds to the passing electromagnetic wave, such as a

plasma, the total electromagnetic field is a combination of the propagating electromagnetic wave and the medium response. This response is a result of the constituent charges in the medium interacting with the passing electromagnetic wave. It is characterised by the auxiliary electric and magnetic response fields, given by

$$\begin{aligned} \vec{D} &= \varepsilon_0 \vec{E} + \vec{P}, \\ \vec{H} &= \frac{1}{\mu_0}\vec{B} - \vec{M}, \end{aligned} \tag{2.37}$$

where $\vec{P}$ is the electric polarization field, and $\vec{M}$ is the magnetisation field.

The electric polarisation is defined as the average electric dipole moment per unit volume. The microscopic electric dipoles arise from a small displacement of the charges in the medium because of the applied electromagnetic field. Positive charges experience a force aligned with the direction of the electric field and so are moved in that direction. On the other hand, negative charges experience a force anti-aligned with the direction of the electric field and so are moved in the opposite direction to the positive charges. The so-called bound charges that make up the electric dipoles are unable to freely move throughout the medium but are accounted for in the total charge density distribution in the medium, i.e.

$$\rho = \rho_{\text{free}} + \rho_{\text{bound}}, \tag{2.38}$$

where here ρ denotes the charge density.

The magnetisation is defined as the average magnetic moment per unit volume. The microscopic magnetic moments arise from the magnetic moments intrinsic to the charges themselves. Usually they are randomly oriented and average to no net magnetic moment but they can become aligned with the application of a magnetic field. When averaged on length scales larger than the atomic scale, the magnetic moments can be approximated as being sourced by bound current loops in the medium. These bound currents are distinguished from the free currents generated by freely moving charges and are included in the total current density distribution

in the medium, i.e.

$$\vec{J} = \vec{J}_{\text{free}} + \vec{J}_{\text{bound}}, \tag{2.39}$$

where $\vec{J}$ denotes the usual total charge density.

The equations that govern the behaviour of the macroscopic (response) fields are the macroscopic Maxwell's equations, which are given by

$$\begin{aligned} \nabla \cdot \vec{D} &= \rho_{\text{free}}, \\ \nabla \cdot \vec{B} &= 0, \\ \nabla \times \vec{E} &= -\partial_t \vec{B}, \\ \nabla \times \vec{H} &= \vec{J}_{\text{free}} + \partial_t \vec{D}. \end{aligned} \tag{2.40}$$

These equations resemble the typical (sourced) microscopic Maxwell's equations, except in how they account for the induced effects from an incident electromagnetic wave. Comparison of Gauss' law from the microcopic and macroscopic Maxwell's equations shows that

$$\nabla \cdot \vec{P} = -\rho_{\text{free}}, \tag{2.41}$$

which is similar to Gauss' law for the electric field $\vec{E}$, except that a polarization field generated from the free charge density acts in the opposite sense to an electric field generated by the total charge density. Similarly, comparison of the corrected Ampere's law in each case shows that

$$\nabla \times \vec{M} = \vec{J}_{\text{bound}} - \partial_t \vec{P}, \tag{2.42}$$

which is similar to the corrected Ampere's law for the magnetic field $\vec{B}$.

For the purposes of the works considered in this thesis, the infalling material is modelled as a cold, magnetised, dielectric plasma. In a dielectric medium, there are no free charges ($\rho_{\text{free}} = 0$) and the induced electric polarization is linearly pro-

portional to the incident electric field, i.e.

$$\vec{P} = \alpha \cdot \vec{E}, \tag{2.43}$$

where here α is the electric susceptibility tensor. Similarly, the induced magnetisation is linearly proportional to the incident magnetic field, i.e.

$$\vec{M} = \chi \cdot \vec{B}, \tag{2.44}$$

where here χ is the magnetic permeability tensor. The auxiliary response fields can be written in terms of the electric and magnetic susceptibility:

$$\begin{aligned} \vec{D} &= \varepsilon_0 \varepsilon \cdot \vec{E}, \\ \vec{H} &= \mu^{-1} \cdot \vec{B}, \end{aligned} \tag{2.45}$$

where $\varepsilon = I + \alpha/\varepsilon_0$ is the so-called dielectric tensor, and $\mu^{-1} = 1/\mu_0 - \chi$ is the reciprocated magnetic permeability tensor.

The effects of a dielectric plasma on the propagating electromagnetic wave are entirely encoded in the dielectric tensor and magnetic permeability tensor. In the absence of free charges and free currents, the macroscopic Maxwell's equations give a different condition for the possible polarization states than equation (2.33), namely,

$$\vec{k} \cdot (I + \alpha/\varepsilon_0) \cdot \vec{E}_0 = \vec{0}, \tag{2.46}$$

which reduces to the classical vacuum polarization condition when the there is no induced electric polarization in the plasma (because α vanishes). The dielectric plasma dispersion relation differs from the classical vacuum dispersion relation, namely,

$$\frac{c^2}{\omega^2}\vec{k} \times \left(\mu^{-1} \cdot \left[\vec{k} \times \vec{E}_0\right]\right) + \varepsilon \cdot \vec{E}_0 = \vec{0}. \tag{2.47}$$

The magnetised regime is appropriate when there is an external magnetic field, in this case the NS magnetic field, that is strong enough to influence the motion of the charges in the plasma. The cold approximation is appropriate when the thermal motions of the charges is much smaller than the induced oscillations from an applied electromagnetic field. Under these additional conditions, the magnetic permeability tensor is well approximated as isotropic, so equation (2.47) can be simplified to

$$\left(\varepsilon - N^2\left[I - \hat{k}\hat{k}\right]\right)\cdot\vec{E}_0 = \vec{0}, \tag{2.48}$$

which can be easily compared with equation (2.36) for the dispersion in classical vacuum. A non-isotropic magnetic permeability tensor arises when treating a vacuum or medium response with the theory of QED. The effects of the QED vacuum become important for when the magnetic field strengths come close to or exceed the quantum critical field strength $\approx 4.4\times10^{13}$G. These are important for the NS magnetic field strengths considered in this thesis at $\sim 10^{13}$G, so the modifications are discussed in a later section.

The solutions to the dispersion relations given in equations (2.36) and (2.48), must hold for non-vanishing $\vec{E}_0$ to allow for the existence of a non-trivial electromagnetic wave. Mathematically, the matrix in the dispersion relations must map a subspace of its domain to $\vec{0}$. Such a matrix is not invertible, so the condition can be represented by

$$\det\left(I - N^2\left[I - \hat{k}\hat{k}\right]\right) = 0, \tag{2.49}$$

$$\det\left(\varepsilon - N^2\left[I - \hat{k}\hat{k}\right]\right) = 0, \tag{2.50}$$

for the classical vacuum case and cold, magnetised, dielectric plasma case respectively.

The solution of N^2 to equation (2.49) can be found immediately by representing the matrix in a basis with $\hat{k}$ as one of the basis vectors, e.g. the 3-index basis vector, which in particular I refer to for the rest of this thesis as the propagation reference frame. The determinant equation can be expanded as a quadratic in N^2

given by

$$N^4 - 2N^2 + 1 = 0. \tag{2.51}$$

This equation is satisfied by $N^2 = 1$, i.e. $k^2 = \omega^2/c^2$, which is a degenerate solution.

The corresponding polarization state for each solution of N^2 is obtained from solving for $\vec{E}_0$ in equation (2.36). In the propagation reference frame, the third component of the vector equation is independent of N^2 and is simply $e_3 = 0$. This is consistent with the polarization condition obtained from the microscopic Maxwell's equations given in equation (2.33). The remaining components of the vector equation depend on N^2 and can be rewritten as a 2-dimensional matrix equation

$$\begin{pmatrix} 1-N^2 & 0 \\ 0 & 1-N^2 \end{pmatrix} \cdot \begin{pmatrix} e_1 \\ e_2 \end{pmatrix} = \vec{0}, \tag{2.52}$$

which is satisfied for all possible values of e_1 and e_2 because $N^2 = 1$. Hence, all polarization states travel through the classical vacuum with the same propagation speed.

The solution of N^2 to equation (2.47) can be found following a similar approach to the vacuum case. However, the solution is not as immediate after representing the matrix in the propagation reference frame. Instead, it is expedient to rewrite the components of the vector equation (2.48) as a 2-dimensional matrix equation first. The third component of the vector equation is independent of N^2 and so e_3 can be written as a linear combination of e_1 and e_2, namely

$$e_3 = -\frac{\varepsilon_{31}}{\varepsilon_{33}} e_1 - \frac{\varepsilon_{32}}{\varepsilon_{33}} e_2 \tag{2.53}$$

where ε_{ij} is the ij component of the dielectric tensor. This means that the third component of the vector equation is a linearly dependent equation and the remaining components of the vector equation can be reduced to a 2-dimensional form after

substituting for e_3, namely

$$\begin{pmatrix} \eta_{11} - N^2 & \eta_{12} \\ \eta_{21} & \eta_{22} - N^2 \end{pmatrix} \cdot \begin{pmatrix} e_1 \\ e_2 \end{pmatrix} = \vec{0}, \tag{2.54}$$

where

$$\begin{aligned} \eta_{11} &= \varepsilon_{11} - \frac{\varepsilon_{13}\varepsilon_{31}}{\varepsilon_{33}},\ \eta_{12} = \varepsilon_{12} - \frac{\varepsilon_{13}\varepsilon_{32}}{\varepsilon_{33}}, \\ \eta_{21} &= \varepsilon_{21} - \frac{\varepsilon_{23}\varepsilon_{31}}{\varepsilon_{33}},\ \eta_{22} = \varepsilon_{22} - \frac{\varepsilon_{23}\varepsilon_{32}}{\varepsilon_{33}}. \end{aligned} \tag{2.55}$$

The determinant equation (2.50) can now be equivalently (albient more simply) expanded as a quadratic in N^2 from equation (2.55), given by

$$N^4 - (\eta_{11} + \eta_{22})N^2 + (\eta_{11}\eta_{22} - \eta_{12}\eta_{21}) = 0. \tag{2.56}$$

This has solutions

$$N_{\pm}^2 = \frac{(\eta_{11} + \eta_{22}) \pm \sqrt{(\eta_{11} - \eta_{22})^2 + 4\eta_{12}\eta_{21}}}{2}, \tag{2.57}$$

which in general are non-degenerate.

The corresponding polarization state for each solution of N^2 can now be obtained from equation (2.46) by solving for the ratios of the components of the polarization states from the dimensionally reduced vector equation (2.54) and the equations that relate e_3 to the other components, which gives

$$K_{12,\pm} := \frac{e_1}{e_2} = \frac{N_{\pm}^2 - \eta_{22}}{\eta_{21}}, \tag{2.58}$$

$$K_{32,\pm} := \frac{e_3}{e_2} = -\frac{\varepsilon_{31}K_{12,\pm} + \varepsilon_{32}}{\varepsilon_{33}}. \tag{2.59}$$

The polarization state is given by

$$\hat{e}_{\pm} = C(K_{12,\pm}, 1, K_{32,\pm}), \tag{2.60}$$

where $C = (K_{12,\pm}^2 + 1)^{-1/2}$ is the normalization of the polarization state in the $1-2$ plane. Since the polarization state vector is written in the propagation reference frame, the third component corresponds to the longitudinal electric field, while the first two components correspond to the transverse electric field. Unlike the classical vacuum case, the electric field of the propagating wave is not entirely perpendicular to the direction of propagation, which can be seen from the condition in equation (2.46).

The ratio of the polarization components in the $1-2$ plane, $K_{12,\pm}$, corresponds to the ellipticity of the polarization state. It can be further simplified by substitution of the expression for $N_\pm^2$, which gives

$$K_{12,\pm} = \left[b \pm \left(b^2 + \frac{\eta_{12}}{\eta_{21}} \right)^{\frac{1}{2}} \right], \tag{2.61}$$

where

$$b = \frac{\eta_{11} - \eta_{22}}{2\eta_{21}} \tag{2.62}$$

is the so-called ellipticity parameter of polarization.

The values for the crucial quantities b and $K_{12,\pm}$ can be calculated explicitly once ε for the plasma is known.

2.2.1.1 Dielectric Tensor for a Cold, Magnetised Plasma

The dielectric tensor of a cold, magnetised plasma can be derived by considering the (classical) motion of charges in the plasma under the influence of an applied electromagnetic wave. The motion of the charges differs from the case of charges in a classical vacuum because of the strong magnetic field and the additional damping effects.

The motion induced by the electromagnetic wave sets up a bound current in the dielectric plasma, so

$$\vec{J}_{\text{bound}} = \sum_s q_s n_s \vec{v}_s, \tag{2.63}$$

where the subscript s denotes the charge species, and q_s, n_s, $\vec{v}_s$ are the charge, number density, and velocity of the charges species respectively.

Assuming the magnetisation field averages to zero, which can be done for a non-rotating classical system in thermal equilibrium (according to the Bohr-van Leeuwen theorem), the electric polarisation field is determined from the bound current using equation (2.42), i.e.

$$\vec{J}_{\text{bound}} = \partial_t \left(\vec{D} - \vec{E} \right). \tag{2.64}$$

Because the electric polarisation field is changing in time due to the incident electromagnetic wave, the frequency associated with the change in the polarisation field is the same as the frequency of the passing electromagnetic wave. Hence, a Fourier transform in the time domain gives

$$\vec{D} = \vec{E} + \sum_s \frac{q_s n_s}{\omega} \vec{v}_s = \varepsilon_0 \varepsilon \cdot \vec{E}, \tag{2.65}$$

where ω is the frequency of the electromagnetic wave. Once $\vec{v}_s$ is known, the dielectric tensor is obtained from comparing each component of the vector equation (2.65).

In the case of a magnetised plasma, the non-relativistic equation of motion for a charge species is the Lorentz force law, given by

$$m_s \frac{\mathrm{d}\vec{v}_s}{\mathrm{d}t} = q_s \left(\vec{E} + \vec{v}_s \times \vec{B}_{\text{ext}} \right) + m \nu_s \vec{v}_s, \tag{2.66}$$

where $\vec{E}$ is the electric component of the incident electromagnetic wave, $\vec{B}_{\text{ext}}$ is the external magnetic field (from the NS), and ν_s is a constant of proportionality for damping for each charge species. In this equation of motion, the magnetic component of the incident electromagnetic wave is neglected because the magnetic field of the NS is much stronger. After a Fourier transform in the time domain and using vector product identities, equation (2.66) can be rearranged to obtain the velocity of

the charge species,

$$\vec{v}_s = \frac{iq_s\omega\lambda_s}{m_s(\omega^2\lambda_s^2 - w_s^2)}\left(\vec{E} - \frac{\vec{E}\cdot\vec{w}_s}{\omega^2\lambda_s^2}\vec{w}_s\right) - \frac{q_s}{m_s(\omega^2\lambda_s^2 - w_s^2)}\vec{E}\times\vec{w}_s, \tag{2.67}$$

where $\lambda_s = 1 - i\nu_s/\omega$ is a damping factor, $\vec{w}_s = q_s/m_s\vec{B}_{\text{ext}}$ is a vector with magnitude w_s, which is the cyclotron frequency for the charge species in the external magnetic field.

The total dielectric plasma response is a sum of each of the charge species velocity. The resulting dielectric tensor can be obtained from (2.65) and is given in index form by

$$\varepsilon_{ij} = \delta_{ij}\left(1 + \sum_s \frac{\omega_{p,s}^2\lambda_s}{\zeta_s}\right) - \sum_s \frac{\omega_{p,s}^2\lambda_s}{\zeta_s}\frac{w_{s;i}w_{s;j}}{\omega^2\lambda_s^2} + \varepsilon_{ijk}\sum_s \frac{i\omega_{p,s}^2}{\omega\zeta_s}w_{s;j}, \tag{2.68}$$

where δ_{ij} is the Kronecker delta, $\omega_{p,s}^2 = n_s q_s^2/m_s$ is the plasma frequency for each particular charge species in the plasma, $\zeta_s = \omega^2\lambda_s^2 - w_s^2$, and ε_{ijk} is the Levi-Civita tensor.

The matrix for the dielectric tensor can be written explicitly after choosing a set of orthonormal basis vectors. A natural choice is for one of the basis vectors, in particular the convention is to choose the 3-index basis vector, to be parallel to $\vec{B}_{\text{ext}}$ so that $w_{s;3} = w_s$ and $w_{s;i} = 0$ for $i \neq 3$. I refer to this basis as the magnetic reference frame for the remainder of this thesis. None of the other basis vectors need to be specified (other than forming an orthonormal set with the 3-index basis vector) to obtain the matrix form of the dielectric tensor, given by

$$\varepsilon = \begin{pmatrix} \varepsilon & ig & 0 \\ -ig & \varepsilon & 0 \\ 0 & 0 & \eta \end{pmatrix}, \tag{2.69}$$

where

$$\varepsilon = 1 + \sum_s \frac{\omega_{p,s}^2}{\zeta_s}\lambda_s,$$
$$ig = \sum_s \frac{i\omega_{p,s}^2}{\omega\zeta_s}w_s,$$
$$\eta = 1 - \sum_s \frac{\omega_{p,s}^2}{\omega^2}\frac{1}{\lambda_s}.$$

These expressions can be rewritten with the physically meaningful ratios of the frequencies

$$v_s = \left(\frac{\omega_{p,s}}{\omega}\right)^2,\ u_s = \left(\frac{w_s}{\omega}\right)^2, \tag{2.70}$$

which is the ratio squared of the plasma frequency, and cyclotron frequency to the wave frequency respectively. This gives

$$\varepsilon = 1 - \sum_s \frac{v_s\lambda_s}{\lambda_s^2 - u_s},$$
$$ig = i\sum_s \frac{v_s u_s^{1/2}}{\lambda_s^2 - u_s},$$
$$\eta = 1 - \sum_s \frac{v_s}{\lambda_s}.$$

A diagonal matrix representation of the dielectric tensor can be obtained by using a rotating coordinate system, which is given via a transformation of the magnetic reference frame basis vectors, $\{b_1, b_2, \hat{w}\}$, to the rotating reference frame basis vectors, $\{b_\mathrm{r}, b_\mathrm{l}, \hat{w}\}$, namely,

$$b_\mathrm{r} = \frac{1}{\sqrt{2}}(b_1 + ib_2),$$
$$b_\mathrm{l} = \frac{1}{\sqrt{2}}(b_1 - ib_2). \tag{2.71}$$

In the previous definitions, the subscript denotes the helicity, with r and l being right-handed and left-handed helicity respectively. This gives the diagonal matrix

representation

$$\begin{pmatrix} \varepsilon - g & 0 & 0 \\ 0 & \varepsilon + g & 0 \\ 0 & 0 & \eta \end{pmatrix}. \tag{2.72}$$

In all, the dielectric tensor for a cold, magnetised dielectric plasma is specified entirely by the data for each charge species: $\{m_s,\ q_s,\ n_s,\ \nu_s\}$, the direction of the magnetic field $\hat{w}$ and its strength B, and the electromagnetic frequency ω. The relationship between these quantities, as given by the dielectric tensor, is entirely determined in the classical regime by the Lorentz force law.

For accreting NSs with a surface magnetic field strength between 10^{11}G and 10^{13}G, the proton cyclotron energy ranges from 0.63×10^{-4} keV to 0.63×10^{-2} keV, whereas the X-ray photons produced in the accretion process have energies ranging from 0.1 keV to 100 keV. Hence, in these scenarios, the contribution to the dielectric tensor from protons is negligible, i.e. $\nu_s \ll 1$ and $u_s \ll 1$ for s representing protons. This allows for a simplifying approximation of the dielectric tensor by including only the electron contribution. If the electron damping is also neglected ($\nu_e = 0$ so that $\lambda_e = 1$), the dielectric tensor can be written in matrix form (in the magnetic reference frame) as

$$\varepsilon = \begin{pmatrix} 1 - \frac{v}{1-u} & i\frac{vu^{1/2}}{1-u} & 0 \\ -i\frac{vu^{1/2}}{1-u} & 1 - \frac{v}{1-u} & 0 \\ 0 & 0 & 1-v \end{pmatrix}, \tag{2.73}$$

where $v = \nu_e$ is ratio squared between the electron frequency in the plasma to the wave frequency, and $u = u_e$ is the ratio squared between the electron cyclotron frequency and the wave frequency.

On the other hand, for an accreting NS with a surface magnetic field strength up to 10^{15}G, which is one of the possible models for PULXs, the proton cyclotron energy reaches up to 6.3 keV, which is in the X-ray band. In these cases, the proton contribution to the dielectric tensor is no longer negligible for photons in the soft X-

ray band ($\sim$ 1 keV). A treatment including the ions is necessary for a more accurate description of the radiation field properties. However, as a first approximation, I consider only the electron contribution in future calculations in this thesis. The inclusion of the proton contribution to the dielectric tensor for these calculations is left for future work.

2.2.1.2 Description of the Polarization States

Returning to the dispersion relation condition for the cold, magnetised, dielectric plasma case given in equation (2.50), the matrix can now be represented explicitly in the magnetic reference frame. However, to use the work already done in the analysis of the polarization states in the propagating reference frame in the previous section, in particular the expressions in equations (2.53) - (2.62), the dielectric tensor must first be written in the propagation reference frame.

A simplified form of the dielectric tensor can be obtained by substituting the terms obtained from writing the dielectric tensor in the magnetic reference frame, given in equation (2.69), into the more general form of the dielectric tensor, given in equation (2.68). This gives

$$\varepsilon_{ij} = \delta_{ij}\varepsilon + (\eta - \varepsilon)\hat{w}_i\hat{w}_j + ig\varepsilon_{ijk}\hat{w}_k, \tag{2.74}$$

where $\hat{w}$ is the unit direction of the external magnetic field, i.e. $\hat{w} = \vec{w}_s/w_s$, which is independent of the charge species. In fact, this simplified dielectric tensor is still general, without approximations in its contribution from charge species and damping factor. These approximations are dealt with in the expressions for ε, η, ig.

To write the dielectric tensor in the propagation reference frame requires a calculation of the expression for $\hat{w}$ in the propagation reference frame. The usual way of describing the wave propagation direction in the magnetic reference frame is by specifying an angle θ between the external magnetic field vector and the propagation direction vector, i.e. $\hat{k}\cdot\hat{w} = \cos\theta$. There is a rotational degree of freedom in the choice of the other two orthonormal bases, so choosing the simplest case that the bases for the propagation reference frame, $\{t_1, t_2, \hat{k}\}$, and the magnetic reference

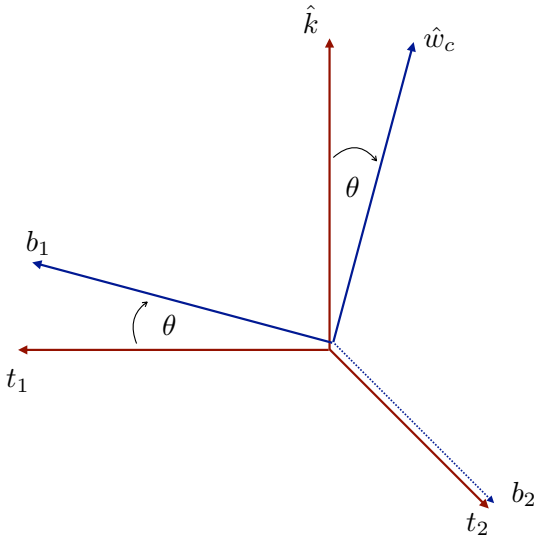

Figure 2.5: A diagram of the relationship between the propagating reference frame, with basis vectors drawn in red, and the magnetic reference frame, with basis vectors drawn in blue.

frame, $\{b_1, b_2, \hat{w}\}$, are related by a single clockwise rotation about b_2, which fixes $b_2 = t_2$ to be perpendicular to the $\hat{k}$-$\hat{w}$ plane, gives the relations

$$\begin{aligned} b_1 &= t_1 \cos\theta + \hat{k} \sin\theta, \\ \hat{w} &= -t_1 \sin\theta + \hat{k} \cos\theta. \end{aligned} \tag{2.75}$$

Figure 2.5 shows a diagram of the basis vectors and the transformation between them. Hence

$$\hat{w} = (-\sin\theta,\ 0,\ \cos\theta) \tag{2.76}$$

in the propagation reference frame.

Using the expression for the dielectric tensor in the propagation reference frame, equation (2.61) for the ellipticity can be simplified further with the anti-symmetries $\varepsilon_{i2} = -\varepsilon_{2i}$ for $i \neq 2$, and with the symmetry $\varepsilon_{13} = \varepsilon_{31}$. In all, this gives

$\eta_{12} = -\eta_{21}$ and thus the ellipticity can be written as

$$K_{12,\pm} = \left[b \pm \left(b^2 - 1 \right)^{\frac{1}{2}} \right], \tag{2.77}$$

where the ellipticity parameter can now also be rewritten in terms of the dielectric tensor components $\varepsilon,\ \eta,\ g$:

$$b = -i \frac{\sin^2 \theta}{2 \cos \theta} \left(\frac{\varepsilon^2 - g^2 - \varepsilon \eta}{g \eta} \right). \tag{2.78}$$

The ellipticity parameter can be simplified further in the approximation that only the electron contribution is significant and there is no damping. This gives the ellipticity parameter in terms of $u,\ v$ as

$$b = i \frac{\sin^2 \theta}{2 \cos \theta} \left(\frac{u^{1/2}}{1 - v} \right). \tag{2.79}$$

The fact that b is a pure imaginary number means that the ellipticity $K_{12,\pm}$ will be a pure imaginary number. Since these are the ratios of the electric field in the transverse (to propagation) direction, the imaginary ellipticity means that the electric field rotates about the propagation direction and the tip of the vector traces out an ellipse. If the damping terms are included, then b is no longer purely imaginary, since the ε and η terms are complex valued.

The ellipticities of the polarization states, as given in equation (2.77), are related by

$$K_{12,+} K_{12,-} = 1. \tag{2.80}$$

This allows for a simplification of the polarization state vectors by the introduction of the ellipticity $i\alpha = K_{12,-} = (K_{12,+})^{-1}$ (Ventura, 1979). The convention to use a factor i in the definition of the ellipticity is to ensure α is a real value when damping terms are neglected. The polarization vectors can now be written in terms of one

ellipticity value, namely

$$\begin{aligned}\hat{e}_+ &= C(1,\ i\alpha,\ \lambda_1),\\ \hat{e}_- &= C(i\alpha,\ 1,\ i\lambda_2),\end{aligned} \tag{2.81}$$

where $C = (1+\alpha^2)^{-1/2}$ is the transverse normalization, and

$$\begin{aligned}\lambda_1 &= -\frac{g\sin\theta}{\varepsilon\sin^2\theta+\eta\cos^2\theta}\left[-\frac{\eta-\varepsilon}{g}\cos\theta+\alpha\right],\\ \lambda_2 &= -\frac{g\sin\theta}{\varepsilon\sin^2\theta+\eta\cos^2\theta}\left[-\alpha\frac{\eta-\varepsilon}{g}\cos\theta-1\right].\end{aligned} \tag{2.82}$$

In the approximation of negligible ion contribution (so only the electrons contribute to the plasma response) and negligible electron damping, the longitudinal polarization components simplify further to

$$\begin{aligned}\lambda_1 &= -\frac{vu^{1/2}}{1-u}\sin\theta\left[u^{1/2}+\alpha\right]\frac{1-u}{1-(v+u\cos^2\theta)},\\ \lambda_2 &= -\frac{vu^{1/2}}{1-u}\sin\theta\left[\alpha u^{1/2}\cos\theta-1\right]\frac{1-u}{1-(v+u\cos^2\theta)}.\end{aligned} \tag{2.83}$$

These expressions show that $\lambda_i \propto v$ and so can be neglected when the electromagnetic frequency is much larger than the plasma frequency, i.e. $\omega_p \ll \omega$. For X-ray radiation > 0.1 keV, this condition is typically met for the accreting plasma (Kaminker et al., 1982), even at the base of the NS accretion column, where the plasma density is greatest.

Finally, the refractive indicies can be more simply expressed as

$$\begin{aligned}N_+^2 &= 1+\frac{1}{i\alpha}\left(\frac{\eta_{21}}{\eta_{22}}\right),\\ N_-^2 &= 1+i\alpha\left(\frac{\eta_{21}}{\eta_{22}}\right),\end{aligned} \tag{2.84}$$

where

$$\frac{\eta_{21}}{\eta_{22}} = -ig\frac{\cos\theta(\varepsilon\sin^2\theta + \eta\cos^2\theta) - ig\sin^2\theta}{\sin^2\theta(\varepsilon^2 - g^2) + \varepsilon\eta\cos^2\theta}. \tag{2.85}$$

Hence $N_\pm$ is complex valued in general, even when the damping term is neglected, except for when the propagation direction is parallel to the magnetic field lines. In this case (and excluding damping), $N_\pm$ is real (except close to the cyclotron resonance $u = 1$, where N_- becomes complex), which indicates that the charge motions parallel to the magnetic field are responsible for extinction, i.e. this induced parallel motion of the charges absorbs some of the incident electromagnetic wave energy.

The real part of the refractive index gives the phase velocity of the associated polarization mode. Hence, the difference in phase velocity for the polarization states is found from

$$|\Re(N_+ - N_-)|, \tag{2.86}$$

which vanishes when $K_+ = K_-$, or equivalently $b = \pm 1$. However, when the damping term is neglected, e.g. as given in equation (2.78), b is purely imaginary. Therefore, damping must be included for the difference in wave speeds to vanish. The condition for differing wave speed for each polarization state is important for the validity of treating the total radiation field as being composed of two radiation fields with their own corresponding polarization state. This approximation, which is referred to as Faraday depolarization, simplifies the radiation transport equations considerably because only the intensity of each normal mode needs to be calculated instead of the full set of 4 Stokes parameters.

Physically, the Faraday depolarization effect is due to the difference in the wave speed of the polarization modes. Propagating electromagnetic waves in a dielectric plasma have a polarization state that is described as a superposition of the polarization modes. The difference in phase velocity results in a rotation of the polarization state.

2.2.1.3 Magnetic Thompson Scattering

So far, the analysis of electromagnetic propagation in a dielectric medium has been restricted to the calculation of the wave speed in the medium (refractive index) and a description of the polarization states. To describe the change in intensity of a light beam as it moves through a medium requires an understanding of how much energy is transmitted or lost (in different directions) because of interactions between the electromagnetic wave and constituent charges in the medium. This is done in the classical regime by calculation of the magnetic Thompson scattering cross-section for the charges, which differs from the usual Thompson scattering cross-section because of the effect of an external magnetic field in constraining the possible motion of the charge. This calculation has been done previously in the context of NS atmospheres but I present the calculation in this thesis as a cohesive whole with the end of obtaining the (magnetised) Rosseland mean opacities for radiative transport in optically thick plasmas.

The differential Thompson scattering cross-section is defined as the fraction of the total incident power of the wave that is transmitted in a direction Ω, i.e.

$$\frac{\mathrm{d}\sigma}{\mathrm{d}\Omega} := \frac{1}{< S >}\frac{\mathrm{d}P}{\mathrm{d}\Omega}, \tag{2.87}$$

where $< S >$ is the time-averaged Poynting flux from the incident wave before scattering and P is the emitted power after scattering in the direction Ω. The magnitude of the Poynting flux from a plane wave in the classical vacuum with electric field $\vec{E}$ is given by

$$|\vec{S}| = \mu_0^{-1}|\vec{E}|^2, \tag{2.88}$$

and represents the electromagnetic energy flux (power per unit area with a specific direction). To calculate the magnetic Thompson scattering cross-section in the case of charges in the dielectric plasma requires expressions for the radiated electromagnetic fields from the charges (due to induced motion by an incident electromagnetic wave).

In classical electrodynamics, an accelerated charge radiates electromagnetic waves. The expressions for the electromagnetic field of a moving charge in general is obtained from the Lienard-Wiechert potentials, which also accounts the finite speed of electromagnetic waves, i.e. special relativistic effects. The fields for a charge at position $\vec{y}$ moving with normalised velocity $\vec{v}/c = \vec{\beta}$ are given by

$$\begin{aligned}\vec{E}(\vec{x},t) &= q\left[\frac{(\hat{r}-\vec{\beta})(1-\beta^2)}{\gamma^3 r^2}\right]_{\text{ret}} + \frac{q}{c}\left[\frac{\hat{r}}{\gamma^3 r}\times\{(\hat{r}-\vec{\beta})\times\dot{\vec{\beta}}\}\right]_{\text{ret}},\\ \vec{B}(\vec{x},t) &= \hat{r}(t_{\text{ret}})\times\vec{E}(\vec{x},t),\end{aligned} \tag{2.89}$$

where t is the time coordinate, $\vec{r} = \vec{x} - \vec{y}$ is the displacement vector between the observation point at $\vec{x}$ and the charge at $\vec{y}$, $\hat{r} = \vec{r}/r$, $\gamma = (1-\beta^2)^{-1/2}$ is the Lorentz factor for the charge at a specific time, and where the expressions in square brackets are evaluated at the (implicitly defined) retarded time $t_{\text{ret}} = t - r(t_{\text{ret}})/c$.

For an observation point of the field in the far-field regime ($r \gg 1$), the electric field expression for the electric field to lowest order in r is given by

$$\vec{E}_{\text{rad}}(\vec{x},t) = \frac{q}{c}\left[\frac{\hat{r}}{\gamma^3 r}\times\{(\hat{r}-\vec{\beta})\times\dot{\vec{\beta}}\}\right]_{\text{ret}}. \tag{2.90}$$

It is worth noting that $\hat{r} \approx \hat{x}$ in the far-field regime and so specifying the observation point $\vec{x}$ is (approximately) equivalent to specifying the unit propagation direction vector $\hat{k}$ of the radiated electromagnetic wave. Hence, the power transmitted by this (far-field) radiated electric field into a direction Ω is given by

$$|\vec{S}| = \frac{\mathrm{d}P}{\mathrm{d}A} = \frac{1}{r^2}\frac{\mathrm{d}P}{\mathrm{d}\Omega} = \mu_0^{-1}|\vec{E}_{\text{rad}}|^2, \tag{2.91}$$

where $\mathrm{d}A = r^2\mathrm{d}\Omega$ is the differential receiving area of the power transmission in the far-field. In the case where the emitted radiation of interest is of a specific polarization state $\hat{e}'$, the polarized emitted power into a direction Ω is given by the

(complex) projection of the radiated electric field on $\hat{e}'$, i.e.

$$\frac{\mathrm{d}P}{\mathrm{d}\Omega} = \frac{r^2}{\mu_0}|\hat{e}'^{*} \cdot \vec{E}_{\mathrm{rad}}|^2, \tag{2.92}$$

where $*$ indicates a complex conjugate operation.

For the scattering of the electromagnetic wave by charges in a magnetised plasma, the expression for each particular radiated electric field is obtained from the expression for the velocity and acceleration of each corresponding charge species. The velocity is given in equation (2.67) but can be rewritten in a more compact form as

$$\vec{v}_s = -\frac{i\omega}{m_s\omega_{p,s}^2}(\varepsilon_s - I)\cdot\vec{E}, \tag{2.93}$$

where ε_s is the dielectric tensor as in equation (2.68) but taking only the contribution from charge species s, and $\vec{E} = \hat{e}Ee^{i(\vec{k}\cdot\vec{y}-\omega t)}$ is the usual wave solution with polarization state $\hat{e}$. The acceleration of the charges is simply obtained from differentiating equation (2.93) with respect to time. Finally, the specific (for a charge species) radiated electric field is given by

$$\vec{E}_{\mathrm{rad},s}(\hat{k}', r, t) = \left[\frac{Ee^{i(\vec{k}\cdot\vec{y}-\omega t)}}{\gamma_s^3 r}\right]_{\mathrm{ret}} \mathbf{S}_s \cdot \hat{e}, \tag{2.94}$$

where

$$\mathbf{S}_s = -\frac{q_s}{m_s c^2}(I - \hat{k}'\hat{k}')\cdot\Pi_s \tag{2.95}$$

is the scattering amplitude matrix for each species s, and where

$$\Pi_s = \frac{1}{v_s}(I - \varepsilon_s) \tag{2.96}$$

is the polarization matrix for each species s.

The polarized emitted power, given in equation (2.92), can now be used together with the Poynting flux of the incident wave to obtain the differential Thomp-

son scattering cross-section for each charge species in the plasma, and assuming non-relativistic motions (so $\gamma_s = 1$), as

$$\frac{\mathrm{d}\sigma_s}{\mathrm{d}\Omega} = |\hat{e}'^{*} \cdot \mathbf{S}_s \cdot \hat{e}|^2. \tag{2.97}$$

For transverse polarization states, i.e. $(1 - \hat{k}'\hat{k}') \cdot \hat{e}' = \hat{e}'$, which is not the general case for the polarization normal modes of a cold, magnetised, dielectric plasma, this simplifies to

$$\frac{\mathrm{d}\sigma_s}{\mathrm{d}\Omega} = r_{0,s}^2 |\hat{e}'^{*} \cdot \Pi_s \cdot \hat{e}|^2, \tag{2.98}$$

where $r_{0,s} = q_s/m_s c^2$ is the classical electromagnetic radius of the charge species. Implicit in the expressions (2.97) and (2.98) is the dependence on the propagation directions of the incoming incident wave $\hat{k}$ and outgoing radiated wave $\hat{k}'$ through the polarization state vectors.

The differential Thompson scattering-cross section as given in (2.98) can be simplified in a suitable reference frame, namely one in which the polarization matrix is diagonal. This is the rotating reference frame, which was introduced in equations (2.71) to diagonalise the dielectric tensor. The polarization matrix in the rotating reference frame with basis vectors $\{b_\mathrm{r}, b_\mathrm{l}, \hat{w}\}$ is given by

$$\Pi_s = \begin{pmatrix} 1/(\lambda_s - u_s^{1/2}) & 0 & 0 \\ 0 & 1/(\lambda_s + u_s^{1/2}) & 0 \\ 0 & 0 & 1/\lambda_s \end{pmatrix}, \tag{2.99}$$

and a general polarization state $\hat{e}$ is expressed in terms of the basis vectors as

$$\hat{e} = e_\mathrm{r} b_\mathrm{r} + e_\mathrm{l} b_\mathrm{l} + e_3 \hat{w}, , \tag{2.100}$$

where $e_\mathrm{r},\ e_\mathrm{l},\ e_3$ are scalar components of the polarization state vector. Hence, the dfferential Thompson scattering cross-section in the rotating reference frame is

given by

$$\frac{\mathrm{d}\sigma_s}{\mathrm{d}\Omega} = r_{0,s}^2 \left| \frac{e_{\mathrm{r}}'^* e_{\mathrm{r}}}{\lambda_s - u_s^{1/2}} + \frac{e_{\mathrm{l}}'^* e_{\mathrm{l}}}{\lambda_s + u_s^{1/2}} + \frac{e_z'^* e_z}{\lambda_s} \right|^2 . \tag{2.101}$$

The differential Thompson scattering cross-section is typically integrated over the incoming and outgoing propagation directions to obtain a total cross-section for the interaction, which is the Thompson scattering cross-section. The integration over the propagation directions is done in spherical coordinates to make explicit some of the symmetries. Hence, an expression for the polarization states in terms of spherical polar coordinates is needed. This expression can be obtained by using a spherical coordinate system in the magnetic reference frame (with basis vectors $\{b_1, b_2, \hat{w}\}$).

For a spherical coordinate system (R, θ, φ) with axis that aligns with $\hat{w}$, the propagation direction of an incoming wave $\hat{k}$ in general is given by

$$\hat{k} = (\sin\theta_{\hat{k}} \cos\varphi_{\hat{k}},\ \sin\theta_{\hat{k}} \sin\varphi_{\hat{k}},\ \cos\theta_{\hat{k}}), \tag{2.102}$$

where $\cos\theta_{\hat{k}} = \hat{k} \cdot \hat{w}$, and the coordinates $\theta_{\hat{k}},\ \varphi_{\hat{k}}$ explicitly show they are related to the propagation direction. The polarization state has so far been calculated in the propagation reference frame corresponding to its own wave. A series of rotation transformations, i.e. the inverse of the one given in equation (2.71) and a second rotation about $\hat{w}$, gives the vector in terms of the basis of the magnetic reference frame. In the magnetic reference frame, it is simple to express in the spherical coordinate system, i.e.

$$\hat{e} = \tilde{e}_1 b_1 + \tilde{e}_2 b_2 + \tilde{e}_3 \hat{w}, \tag{2.103}$$

where $\tilde{e}_i = \tilde{e}_i(\theta_{\hat{k}}, \varphi_{\hat{k}})$ for $i = 1, 2, 3$. From the general form of the dielectric tensor in equation (2.74), it is evident that the expression is invariant under rotation about $\hat{w}$. Thus, by rotating $\hat{k}$ about the $\hat{w}$ axis, i.e. keeping $\theta_{\hat{k}}$ constant and changing $\varphi_{\hat{k}}$, the polarization state of the wave in unchanged, except in its projection along the

corresponding axes perpendicular to $\hat{w}$, i.e.

$$\tilde{e}_1(\theta_{\hat{k}}, \varphi_{\hat{k}}) = \tilde{e}_1(\theta_{\hat{k}}) \cos \varphi_{\hat{k}},$$
$$\tilde{e}_2(\theta_{\hat{k}}, \varphi_{\hat{k}}) = \tilde{e}_2(\theta_{\hat{k}}) \sin \varphi_{\hat{k}}. \tag{2.104}$$

Thus, using the same spherical coordinate system but instead writing in terms of the rotating reference frame basis vectors $\{b_{\mathrm{r}}, b_{\mathrm{l}}, \hat{w}\}$, the polarization state vector is given by

$$\hat{e} = \frac{1}{\sqrt{2}} \tilde{e}_1 e^{i\varphi_{\hat{k}}} b_{\mathrm{r}} + \frac{1}{\sqrt{2}} \tilde{e}_2 e^{-i\varphi_{\hat{k}}} b_{\mathrm{l}} + \tilde{e}_3 \hat{w}. \tag{2.105}$$

The expression for $\hat{e}'$ in spherical coordinates in the rotating reference frame are similar to equation (2.105), except with angles relating to its own wave propagation direction i.e. $\theta_{\hat{k}'},\ \varphi_{\hat{k}'}$.

The differential Thompson scattering cross-section can now be written as

$$\frac{\mathrm{d}\sigma_s}{\mathrm{d}\Omega}(\hat{k} \to \hat{k}') = r_{0,s}^2 \left| \frac{1}{2} \frac{\tilde{e}_1'^* \tilde{e}_1 e^{i(\varphi_{\hat{k}} - \varphi_{\hat{k}'})}}{(1-\sqrt{u_s})+i\Gamma_s} + \frac{1}{2} \frac{\tilde{e}_2'^* \tilde{e}_2 e^{-i(\varphi_{\hat{k}} - \varphi_{\hat{k}'})}}{(1+\sqrt{u_s})+i\Gamma_s} + \frac{\tilde{e}_3'^* \tilde{e}_3}{1+i\Gamma_s} \right|^2, \tag{2.106}$$

where the denominators have been expanded fully with $-\nu_s/\omega = \Gamma$, and the dependence of the components in $\theta_{\hat{k}}$ (or $\theta_{\hat{k}'}$) has been omitted for brevity. By integrating over all of $\varphi_{\hat{k}'}$, i.e. the symmetry of the outgoing radiated wave, the cross-terms of equation (2.106) vanish, leaving

$$\int \mathrm{d}\varphi_{\hat{k}'} \frac{\mathrm{d}\sigma_s}{\mathrm{d}\Omega} = r_0^2 \left[\frac{1}{4} \frac{|\tilde{e}_1'|^2 |\tilde{e}_1|^2}{(1-\sqrt{u_s})^2 + \Gamma_s^2} + \frac{1}{4} \frac{|\tilde{e}_2'|^2 |\tilde{e}_2|^2}{(1+\sqrt{u_s})^2 + \Gamma_s^2} + \frac{|\tilde{e}_3'|^2 |\tilde{e}_3|^2}{1+\Gamma_s^2} \right]. \tag{2.107}$$

The integrations over all incident propagation direction angles, $\theta_{\hat{k}}$ and $\varphi_{\hat{k}}$ gives the Thompson scattering cross-section, which still depends on the angle of the outgoing propagation direction with the magnetic field, as

$$\frac{\sigma_s(\theta_{\hat{k}'})}{\sigma_{\mathrm{T}}} = \frac{A_1 |\tilde{e}_1'|^2}{(1-\sqrt{u_s})^2 + \Gamma_s^2} + \frac{A_2 |\tilde{e}_2'|^2}{(1+\sqrt{u_s})^2 + \Gamma_s^2} + \frac{A_3 |\tilde{e}_3'|^2}{1+\Gamma_s^2}, \tag{2.108}$$

where $\sigma_{\mathrm{T}} = (8\pi/3) r_0^2$ is the non-magnetised Thompson scattering cross-section (for

the particular charge species), and

$$A_{\rm I} = \frac{3}{4}\int_{-1}^{+1} {\rm d}(\cos\theta_{\hat{k}})|\tilde{e}_{\rm I}(\theta_{\hat{k}})|^2 \tag{2.109}$$

for index $\mathrm{I} = 1,2,3$.

The final step in computing the magnetised Thompson scattering cross-section is in giving the explicit expression for the polarization normal modes in the rotating reference frame. Starting from the propagation reference frame, as in equations (2.81), and following the transformation procedure, the polarization normal modes for a cold, mangetised, dielectric plasma are given by

$$\begin{aligned}
\hat{e}_+ &= \frac{C}{\sqrt{2}}\left(\begin{Bmatrix}\cos\theta_{\hat{k}} - \lambda_1\sin\theta_{\hat{k}} \\ -\alpha\end{Bmatrix}, \begin{Bmatrix}\cos\theta_{\hat{k}} - \lambda_1\sin\theta_{\hat{k}} \\ +\alpha\end{Bmatrix}, \sqrt{2}\left\{\sin\theta_{\hat{k}} + \lambda_1\cos\theta_{\hat{k}}\right\}\right), \\
\hat{e}_- &= \frac{iC}{\sqrt{2}}\left(\begin{Bmatrix}\alpha\cos\theta_{\hat{k}} - \lambda_2\sin\theta_{\hat{k}} \\ +1\end{Bmatrix}, \begin{Bmatrix}\alpha\cos\theta_{\hat{k}} - \lambda_2\sin\theta_{\hat{k}} \\ -1\end{Bmatrix}, \sqrt{2}\left\{\alpha\sin\theta_{\hat{k}} + \lambda_2\cos\theta_{\hat{k}}\right\}\right).
\end{aligned} \tag{2.110}$$

Under the approximation of transverse polarization states, when the wave frequency is much larger than the plasma frequency, i.e. $v_s \ll 1$, the components of the polarization normal modes are simplified and satisfy completeness relations given by the sum of polarization states, in particular

$$\sum_{j=+,-}|\tilde{e}_{j;i}|^2 = \frac{1}{2}(1+\cos^2\theta_{\hat{k}}), \quad \sum_{j=+,-}|\tilde{e}_{j;3}|^2 = \sin^2\theta_{\hat{k}}, \tag{2.111}$$

where $i = 1,2$ and $\tilde{e}_{j;i}$ denotes the i-th component of a the j-polarization normal mode. From the completeness relations, the $A_{\rm I}$ satisfy

$$\sum_{j=+,-} A_{\rm I}^j = 1, \tag{2.112}$$

where $I = 1,2,3$ and A_i^j denotes the j-th polarization normal mode of the A_i as given in equation (2.109). Hence, the non-magnetised Thompson scattering cross-section

for unpolarized scattering of each charge species, $\sigma_{\rm T}$, is recovered in the limiting case $v_s \ll 1$.

In all, there are 4 polarization normal mode scattering cross-sections,

$$\begin{aligned} &\sigma_{+\to+},\ \sigma_{+\to-}, \\ &\sigma_{-\to+},\ \sigma_{-\to-}, \end{aligned} \tag{2.113}$$

which will be used in the radiation transport equations to obtain the radiation field properties.

2.2.2 Radiative Transfer Solution

The steady state, polarized radiative transfer equation in the large Faraday depolarization regime (which allows for the intensity to be written in terms of the normal modes) is given by

$$\hat{k}\cdot\nabla_{\vec{x}} I_j(\nu,\hat{k},\vec{x}) = \sum_i \int {\rm d}\Omega' \frac{{\rm d}\sigma_{i\to j}}{{\rm d}\Omega}(\hat{k}'\to\hat{k}) I_i(\nu,\hat{k}',\vec{x}) - \kappa_j(\nu,\hat{k}) I_j(\nu,\hat{k},\vec{x}), \tag{2.114}$$

where $\nabla_{\vec{x}}$ denotes the ∇ operator acting on the coordinate space $\vec{x}$ only, $\int {\rm d}\Omega'$ denotes the integration over all directions $\hat{k}'$,

$$\frac{{\rm d}\sigma_{i\to j}}{{\rm d}\Omega}(\hat{k}'\to\hat{k})$$

is the differential scattering cross-section for an incident beam with polarization state i and propagation direction $\hat{k}'$ scattered to an outgoing beam with polarization state j with propagation direction $\hat{k}$, and

$$\kappa_j(\nu,\hat{k}) = \sum_i \int {\rm d}\Omega' \frac{{\rm d}\sigma_{j\to i}}{{\rm d}\Omega'}(\hat{k}\to\hat{k}').$$

Several different methods exist to solve the radiative transfer equations in general (Meszaros, 1992), such as a transformation to a second-order differential equation, which is the so-called Feautrier method, the Monte Carlo method, and the moments of intensity method. The ideal use cases for each method depend on the

simplifications and symmetries in the problem to be solved. For the work of this thesis, I use the moments of intensity method, which takes an integral of the radiative transfer equation (2.114) over all the directions of the intensity (and its higher moments). This method is suitable for transport through an optically thick medium, where the radiation field can be approximated as in local thermal equilibrium with the medium.

The zeroth moment of the intensity is the total radiation energy density, given by

$$U_i = \int \mathrm{d}\nu \; \mathrm{d}\Omega \; I_i(\nu, \hat{k}, \vec{x}). \tag{2.115}$$

The first moment of the intensity can be understood from the definition (2.29) as the radiation flux vector, given by

$$\vec{F}_i = \int \mathrm{d}\nu \; \mathrm{d}\Omega \; \hat{k} \; I_i(\nu, \hat{k}, \vec{x}). \tag{2.116}$$

Finally, the second moment of the intensity is the radiation pressure tensor, given by

$$P_i = \int \mathrm{d}\nu \; \mathrm{d}\Omega \; \hat{k}\hat{k} \; I_i(\nu, \hat{k}, \vec{x}). \tag{2.117}$$

Hence, taking the zeroth moment of the equation (2.114) gives

$$\nabla_{\vec{x}} \cdot \vec{F}_j = \sum_i \left[\int \mathrm{d}\nu \; \mathrm{d}\Omega \; \mathrm{d}\Omega' \; \frac{\mathrm{d}\sigma_{i\to j}}{\mathrm{d}\Omega}(\hat{k}' \to \hat{k}) I_i(\hat{k}') - \int \mathrm{d}\nu \; \mathrm{d}\Omega \; \kappa_j(\hat{k}) I_j(\hat{k}) \right], \tag{2.118}$$

where the full dependencies of the terms in ν and $\vec{x}$ have been ommitted. This equation can be simplified by expanding the $\kappa_j(\hat{k})$ term and using the forward-backward symmetry of the differential scattering cross section, namely

$$\frac{\mathrm{d}\sigma_{i\to j}}{\mathrm{d}\Omega'}(\hat{k} \to \hat{k}') = \frac{\mathrm{d}\sigma_{j\to i}}{\mathrm{d}\Omega}(\hat{k}' \to \hat{k}), \tag{2.119}$$

to get

$$\nabla_{\vec{x}} \cdot \vec{F}_j = \sum_i \left[\int \mathrm{d}\nu \, \mathrm{d}\Omega \, \mathrm{d}\Omega' \, \left\{ \frac{\mathrm{d}\sigma_{i\to j}}{\mathrm{d}\Omega}(\hat{k}' \to \hat{k}) I_i(\hat{k}') - \frac{\mathrm{d}\sigma_{i\to j}}{\mathrm{d}\Omega}(\hat{k}' \to \hat{k}) I_j(\hat{k}) \right\} \right]. \tag{2.120}$$

Hence, the first and last term of the equation can be integrated with respect to $\mathrm{d}\Omega$ and $\mathrm{d}\Omega'$ respectively, and the polarization states summed over to give

$$\nabla_{\vec{x}} \cdot \vec{F}_j = \bar{\sigma}_{+\to j} \int \mathrm{d}\nu \, \mathrm{d}\Omega (I_+ - I_j) + \bar{\sigma}_{-\to j} \int \mathrm{d}\nu \, \mathrm{d}\Omega (I_- - I_j), \tag{2.121}$$

where $\bar{\sigma}_{i\to j}$ is the intensity mean scattering cross-section, given by

$$\bar{\sigma}_{i\to j} = \frac{\int \mathrm{d}\nu \, \mathrm{d}\Omega \, \sigma_{i\to j}(\Omega)(I_i - I_j)}{\int \mathrm{d}\nu \, \mathrm{d}\Omega \, (I_i - I_j)}. \tag{2.122}$$

Finally, using detailed balance, i.e. $\bar{\sigma}_{i\to j} = \bar{\sigma}_{j\to i}$, equation (2.121) can be written as

$$\nabla_{\vec{x}} \cdot \vec{F}_\pm = \bar{\sigma}_{+\to -}(U_\mp - U_\pm). \tag{2.123}$$

For taking the first moment of intensity of the equation (2.114), it is convenient to first divide by κ_j before integrating. This gives

$$\int \mathrm{d}\nu \, \mathrm{d}\Omega \, \frac{\hat{k}\hat{k}}{\kappa_j(\nu, \hat{k})} \cdot \nabla_{\vec{x}} I_j(\nu, \hat{k}, \vec{x}) = -\vec{F}_j, \tag{2.124}$$

where the first term has vanished after integrating with respect to $\mathrm{d}\Omega$ because it is anti-symmetric in $\hat{k}$ while the differential scattering cross-section has reflection symmetry in $\hat{k}$, i.e.

$$\begin{aligned} \frac{\mathrm{d}\sigma_{i\to j}}{\mathrm{d}\Omega}(\hat{k}' \to \hat{k}) &= \frac{\mathrm{d}\sigma_{i\to j}}{\mathrm{d}\Omega}(\hat{k}' \to -\hat{k}) \\ \implies \kappa_i(\nu, \hat{k}) &= \kappa_i(\nu, -\hat{k}). \end{aligned} \tag{2.125}$$

After projection onto a direction $\hat{n}$, equation (2.124) can be simplified using the

projected pressure mean scattering cross-section, given by

$$\frac{1}{\bar{\kappa}_i} = \frac{\int \mathrm{d}\nu \; \mathrm{d}\Omega \; \frac{\hat{n}\cdot\hat{k}\hat{k}}{\kappa_i(\nu,\hat{k})} \cdot \nabla_{\vec{x}} I_i}{\int \mathrm{d}\nu \; \mathrm{d}\Omega \; \hat{n}\cdot\hat{k}\hat{k}\cdot\nabla_{\vec{x}} I_i}, \tag{2.126}$$

to get the projected first moment of intensity of the radiative transfer equation (in a direction $\hat{n}$)

$$\frac{1}{\bar{\kappa}_j}\hat{n}\cdot(\nabla_{\vec{x}}\cdot P_j) = -\hat{n}\cdot\vec{F}_j. \tag{2.127}$$

The system of equations given by (2.123) and (2.127) is not closed. Taking successive moments of the radiative transfer equation continues to introduce higher moments of the intensity, so a closure condition is needed to relate the moments of intensity to one another. The most relevant closure condition for an optically thick medium comes from the approximation that the radiation field is in local thermal equilibrium. Specifically, this means that the medium is homogeneous on a length scale larger than the mean free path length of the light (given by $\ell \sim 1/\bar{\kappa}_i$), i.e. the light is scattered multiple times in a homogeneous finite element of the medium, and thus the radiation field is isotropic on these length scales. Under local thermal equilibrium, the moments of intensity satisfy

$$\frac{1}{3}U_i \,\mathrm{Id} = P_i, \; \vec{F}_i = \vec{0}, \tag{2.128}$$

where Id is the isotropic tensor. This closure condition is referred to as the Eddington closure condition.

Applying the Eddington closure condition to the system of equations gives the closed system:

$$\begin{aligned} \nabla_{\vec{x}}\cdot\vec{F}_\pm &= \bar{\sigma}_{+\to-}\left(U_\mp - U_\pm\right), \\ \frac{1}{\bar{\kappa}_\pm}\frac{1}{3}\hat{n}\cdot\mathrm{Id}\cdot\nabla_{\vec{x}}U_\pm &= -\hat{n}\cdot\vec{F}_\pm, \end{aligned} \tag{2.129}$$

which once solved specifies the radiation energy density field. The flux is non-

vanishing in these equations because it is implicit that $\nabla_{\vec{x}}$ measures the change in each quantity over a large enough length scale, i.e. the quantity of interest is the flux between homogeneous finite elements of the medium. To obtain a solution requires the computation of the intensity mean scattering cross-section, $\bar{\sigma}_{+\to-}$ given in equation (2.122), and the pressure mean scattering cross-section, $\bar{\kappa}_j$ given in equation (2.126).

From the local thermal equilibrium assumption, the intensity in each homogeneous finite element is approximately that of a blackbody, i.e. $I_j(\nu,\hat{k},\vec{x}) = B_\nu(T(\vec{x}))$, where B_ν is the Planck function and $T(\vec{x})$ is the temperature field. Hence, the intensity mean scattering cross-section can be approximated by the Planck mean, given by

$$\bar{\sigma}^P_{i\to j} = \frac{\int \mathrm{d}\nu\ \mathrm{d}\Omega\ \sigma_{i\to j}(\Omega)B_\nu}{4\pi \int \mathrm{d}\nu\ B_\nu}, \tag{2.130}$$

and the pressure mean scattering cross-section can be approximated by the Rosseland mean, given by

$$\frac{1}{\bar{\kappa}^R_i} = \frac{\int \mathrm{d}\nu\ \mathrm{d}\Omega\ \frac{\hat{n}\cdot\hat{k}\hat{k}}{\kappa_i(\nu,\hat{k})}\cdot\nabla_{\vec{x}}T(\vec{x})\frac{\partial B_\nu}{\partial T}}{\int \mathrm{d}\nu\ \mathrm{d}\Omega\ \hat{n}\cdot\hat{k}\hat{k}\cdot\nabla_{\vec{x}}T(\vec{x})\frac{\partial B_\nu}{\partial T}}. \tag{2.131}$$

For the problem of radiative transfer in the optically thick accretion column, the Rosseland mean scattering cross-section can be simplified further. This is done by choosing a coordinate system to specify $\vec{x} = (x,y,z)$ so that the basis vector for the z-direction aligns with the magnetic field lines, and by choosing the spherical coordinate system to specify $\hat{k}$ so that the spherical axis also aligns with the magnetic field lines. A projection $\hat{n}$ parallel to the magnetic field lines gives

$$\hat{n}\cdot\hat{k}\hat{k}\cdot\nabla_{\vec{x}} = \cos\theta\left[\cos\varphi\sin\theta\partial_x + \sin\varphi\sin\theta\partial_y + \cos\theta\partial_z\right] \tag{2.132}$$

as the operator acting on $T(\vec{x})$. This operator can be integrated with respect to $\mathrm{d}\Omega$, resulting in the first two terms vanishing by anti-symmetry in domain of $\mathrm{d}\varphi$. Hence

the parallel Rosseland mean scattering cross-section is given by

$$\frac{1}{\bar{\kappa}^R_{i,\parallel}} = \frac{\int \mathrm{d}\nu \; \mathrm{d}\mu \; \frac{3}{2}\frac{\mu^2}{\kappa_i(\nu,\mu)}\frac{\partial B_\nu}{\partial T}}{\int \mathrm{d}\nu \; \frac{\partial B_\nu}{\partial T}}, \tag{2.133}$$

where $\mu = \cos\theta$, and the symmetry of κ_i in φ was used, i.e. $\kappa_i(\nu,\hat{k}) = \kappa_i(\nu,\mu)$.

Similarly, a projection $\hat{n}$ perpendicular to the magnetic field lines, in particular along the x-axis, gives

$$\hat{n}\cdot\hat{k}\hat{k}\cdot\nabla_{\vec{x}} = \cos^2\varphi\sin^2\theta\,\partial_x + \sin\varphi\cos\varphi\sin^2\theta\,\partial_y + \cos\varphi\sin\theta\cos\theta\,\partial_z \tag{2.134}$$

as the operator acting on $T(\vec{x})$. This operator can be integrated with respect to $\mathrm{d}\Omega$, which results in the second term vanishing by anti-symmetry in the domain of $\mathrm{d}\varphi$ and the third term vanishing by anti-symmetry in the domain of $\mathrm{d}\mu$. Hence the perpendicular Rosseland mean scattering cross-section is given by

$$\frac{1}{\bar{\kappa}^R_{i,\perp}} = \frac{\int \mathrm{d}\nu \; \mathrm{d}\Omega \; \frac{3}{2\pi}\frac{\mu_\perp^2}{\kappa_i(\nu,\mu)}\frac{\partial B_\nu}{\partial T}}{\int \mathrm{d}\nu \; \frac{\partial B_\nu}{\partial T}}, \tag{2.135}$$

where $\mu_\perp^2 = \cos^2\varphi(1-\mu^2)$. By symmetry of κ_i in φ and that $\int \mathrm{d}\varphi \;\sin^2\varphi = \int \mathrm{d}\varphi \;\cos^2\varphi$, the result is exactly the same for a projection in the y-axis. Hence, the perpendicular Rosseland mean scattering cross-section is sufficient to specify the system of radiative transfer equations under the Eddington closure condition.

In general, without further assumptions on the temperature field, the system of radiative transfer equations with the Eddington closure condition can be written out fully as

$$\begin{aligned}
\nabla_{\vec{x}}\cdot\vec{F}_\pm &= \bar{\sigma}^P_{+\to-}(U_\mp - U_\pm),\\
\frac{1}{\bar{\kappa}^R_{\pm,\parallel}}\frac{1}{3}\partial_\parallel U_\pm &= -F_{\pm,\parallel},\\
\frac{1}{\bar{\kappa}^R_{\pm,\perp}}\frac{1}{3}\partial_\perp U_\pm &= -F_{\pm,\perp},
\end{aligned} \tag{2.136}$$

where $\partial_\parallel$ and $\partial_\perp$ is the partial derivative parallel and perpendicular to the magnetic

field lines respectively; $F_{\pm,\parallel}$ and $F_{\pm,\perp}$ is the flux vector projected parallel and perpendicular to the magnetic field lines respectively.

Chapter 3

Maximum Luminosity

The work presented in this chapter was also published in Brice et al. (2021).

There has been a resurgence of interest on the question of the maximum luminosity of an accreting NS due to the discovery of a new sub-population of accreting NSs (Bachetti et al., 2014; Fürst et al., 2016; Israel et al., 2017b,a; Carpano et al., 2018; Wilson-Hodge et al., 2018; Sathyaprakash et al., 2019; Rodríguez Castillo et al., 2020) - persistent super-Eddington ($> 10^{39}$erg s^{-1}) accreting X-ray pulsars, called Pulsating Ultra-Luminous X-ray sources (PULXs) or Ultra-luminous Pulsars (ULPs), which exceed the NS Eddington luminosity by at least an order of magnitude. How accreting NSs are able to produce persistent super-Eddington luminosities is still an open question (King et al., 2023). In this thesis, I consider the scenario of accretion by NSs with magnetar-like strength magnetic fields ($> 10^{13}$G at the surface) [1], as a continuation of the models of magnetically funnelled accretion.

Basko & Sunyaev (1976) were the first to provide a detailed calculation of the maximum luminosity in the magnetically funnelled accretion model. These authors were attempting to explain X-ray pulsars observed with luminosities of $\sim$

[1] The alternative scenario put forward by King et al. (2023) is an extension of the models of black hole accretion to the super-Eddington accretion rates (Gladstone et al., 2009), in which the persistent super-Eddington luminosities are only apparent to an observer due to geometric beaming by optically thick outflows from the accretion disc. Evidence for this model in the context of black hole accretors has recently been obtained from IXPE observations of Cyg X-3 (Veledina et al., 2023). However, the model remains a qualitative description with only phenomonelological modelling of the luminosity amplification (King, 2009). The quantification of the luminosity amplification is still an open question.

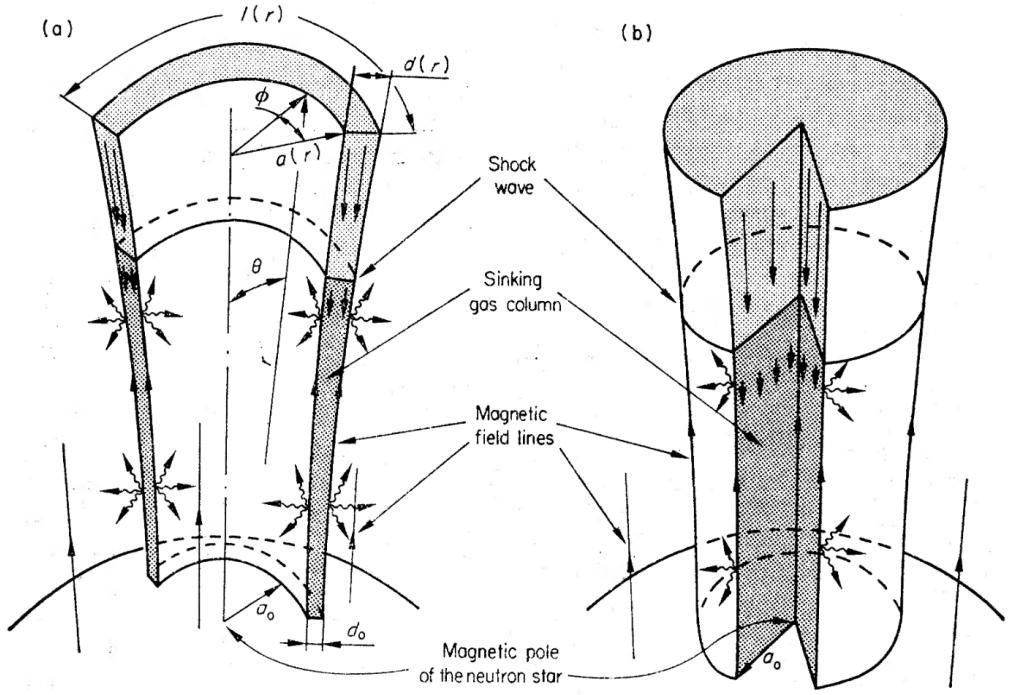

Figure 3.1: Reprint of Fig.1 from Basko & Sunyaev (1976), which shows the geometry of the accretion flow in the cases: (a) a narrow wall surrounding the magnetic pole, (b) a filled column above the cap. In both cases, a radiative shock is present above the NS surface and a slowly sinking column of gas manifests below the shock.

few $\times 10^{38}$erg s^{-1}, which are already above the NS Eddington luminosity. In their model, the change in geometry of the accretion flow from the magnetic funnelling (by a dipole magnetic field), and the presence of a radiative shock above the NS surface were crucial to the increase in maximum luminosity above Eddington. In particular, they argued that accreting material funnelled from a disc was confined to a narrow wall surrounding the magnetic pole, rather than filling the entire space above the pole.

Figure 3.1, which is a reprint from Basko & Sunyaev (1976), illustrates the geometry of the flow. In both cases, the flow below the radiative shock is slowly sinking and optically thick to the radiation. The geometry of the flow in the narrow wall case means a lower optical depth perpendicular to the flow direction than in the filled column case. This results in the perpendicular flux of escaping radiation to be greater than the the locally Eddington limited parallel flux.

In the narrow wall case, Basko & Sunyaev (1976) obtained an analytical ex-

pression of the maximum luminosity, given by

$$L_{\max} \approx 8 \times 10^{38} \left(\frac{l_0/d_0}{40}\right) \left(\frac{\kappa_{\rm T}}{\kappa}\right) \left(\frac{M}{M_\odot}\right) \text{erg s}^{-1}, \tag{3.1}$$

where l_0 is the circumference of the footprint of the wall on the NS surface, and d_0 is the width of the wall on the NS surface. Several simplifying assumptions were used to obtain the result in equation (3.1). Namely, the equations of hydrodynaics and radiation transport were solved only for the radial coordinate in a spherical coordinate system, the changes in plasma opacities induced by the strong magnetic field were neglected (although the authors noted the potential for a further increase to the maximum luminosity by this effect), and the magnetic field topology was assumed to be dipolar.

Later, Lyubarskii & Syunyaev (1988) reconsidered the narrow wall model and provided an estimate of the height of the slowly sinking region across the width of the wall. These authors argued that because the slowly sinking region was radiation pressure supported, the rapid decrease in radiation pressure from the centre of the region resulted in a drop in height. However, a detailed calculation of radiation pressure across the width of the wall, in addition to an estimate of the escaping radiation, was only provided later by Mushtukov et al. (2015). I give the details of this model, with the inclusion of a more general magnetic field topology, in the following section.

Mushtukov et al. (2015) computed the maximum luminosity, using the 2D model of Lyubarskii & Syunyaev (1988) as a basis, including the magnetically induced changes to the plasma opacities for the first time. The new maximum luminosity was high enough to explain the luminosity of M82 X-2 at $\sim 10^{40}$ erg s^{-1} (Bachetti et al., 2014) - the first PULX discovered - provided the presence of an ultra-strong (10^{14}G) magnetic field at the NS surface. Tsygankov et al. (2016) found evidence for an ultra-strong dipole field from the transitions between states with luminosities differing by a factor of 40. However, with the discovery NGC5907 ULX-1 - the brightest PULX known to date - the required dipole magnetic field strength to explain a luminosity of $\sim 10^{41}$ erg s^{-1} would place this source deep in

the propeller regime (Israel et al., 2017a), where the accretion process is thought to be halted completely.

A resolution to this issue was proposed in the discovery paper by Israel et al. (2017a), namely that higher order multipole moments of the magnetic field dominate close to the surface while a weaker strength dipole component would avoid the propeller regime. There is a precedent for this kind of magnetic field topology in magnetars (e.g. Tiengo et al. 2013), isolated NSs (e.g. Borghese et al. 2015, 2017), and millisecond pulsars (e.g. Bilous et al. 2019).

The contribution of this thesis is in constructing a model of the accretion column (the slowly sinking region constituent of the narrow wall) that relaxes the assumption of a pure dipole magnetic field topology. The model of Mushtukov et al. (2015) is used as a basis. In this particular model, the equations of hydrodynamics and radiation transport are treated in a (flat) Cartesian coordinate system with the curvature of the field lines given an approximate treatment in the change of the width and arc-length of the wall with increasing height above the NS surface.

A more accurate treatment of the hydrodynamic equations using a curvilinear coordinate system has been done for a pure dipole magnetic field topology by Canalle et al. (2005) and a dipole plus octupole topology by Adams & Gregory (2012). However, these authors treat the hydrodynamics in an accretion regime where the infalling plasma is optically thin throughout the infall. [2] The plasma velocity profile is solved while the radiation transport is approximated as a cooling mechanism for the flow.

Separately, Becker & Wolff (2022) provide a model for the optically thick (radiation supported) accretion column regime that solves for the plasma velocity profile with the final aim of quantifying the emergent spectra from the accretion column. These authors treat of the coupled equations of hydrodynaics and radiative diffusion in 2D, which follows from the previous work by Becker & Wolff (2007) and taking the model in Becker (1998) as a basis. However, the model gives an inconsistent treatment of the optical depth of the accretion column, namely in the

[2] In contrast, for super-Eddington accretion rates, the infalling plasma is optically thick for almost all of the infall (e.g. see §4.2.1 on the regime of validity).

context of the radiative transfer equations by assuming the local thermal equilibrium closure condition while neglecting the use of the Rosseland mean opacity.

In contrast, the work of this thesis accounts for the optical depth self-consistently in the radiation transport equations. This allows for an accounting of the effects of the magnetic field strength in the computation of the maximum luminosity. On the other hand, the treatment of the plasma velocity profile is by ansatz (with consideration of the qualitative results from Becker & Wolff 2007) for simplicity. Combining the two approaches of using a curvilinear coordinate system to account for the magnetic field topology, e.g. Canalle et al. (2005); Adams & Gregory (2012), with the hydrodynamics in an optically thick radiation supported accretion column, e.g. Becker & Wolff (2022), is beyond the scope of this thesis and is left for a future work.

3.1 Accretion Column Model

In this section, I derive the equations of hydrodynamics and radiation diffusion that are used in the calculation of the maximum luminosity, following the original model developed by Basko & Sunyaev (1976), although the derivation more closely follows the work of Mushtukov et al. (2015) by solving in 2D. My contribution is in the calculation of the accretion column geometry for multipolar magnetic field topologies.

For the equations, a flat Cartesian coordinate system is used with coordinates (x,h), where the h-axis is along the magnetic field lines, $x=0$ is at the centre of the accretion column, and $h=0$ is at the NS surface. The curvature of the magnetic field lines is neglected in the coordinates, i.e. the metric is approximated as isotropic, because the accretion column is local to the magnetic poles, where the curvature is not large. [3] However, the effect of the curvature of the magnetic field lines on the plasma density profile and accretion column geometry is taken into account. In particular, the corresponding changes for a multipolar magnetic field topology are calculated.

[3]The effects of the curvature were found to still be as important as the radiative cooling and gravity in the momentum equations for the hydrodynamics (Canalle et al., 2005).

The accretion column geometry is specified by H for the maximum height of the radiative shock, d_0 for the width of the accretion column base, H_x for the height of the shock at width x along the base, and d_h for the width of the sinking region at height h above the surface. Figure 3.2 shows a cross-section of the accretion column with the geometric quantities labelled. In addition, the footprint of the accretion column on the surface is an annulus [4] with arc length l_0 and width d_0 (see figure 3.1), where l_0 and d_0 are determined by the specifics of the disc-magnetosphere interaction and the magnetic field configuration (detailed later). Finally, the total area of the accretion column base is given by $S_D = l_0 d_0$.

In the accretion column (slowly sinking region), the plasma sinks to the NS surface with a velocity much smaller than the free-fall velocity and liberates its gravitational potential energy locally as X-ray radiation. The flow is approximated as a steady-state flow, with velocity directed along the magnetic field lines only and no momentum transport perpendicular to the magnetic field lines. Further, the fluid pressure is assumed to be negligible compared to the radiation pressure. Following Mushtukov et al. (2015), the equations are simplified by assuming the density and velocity profiles are independent of x, and coincide with the profiles at the centre of the column. [5] Finally, the energy diffusion is assumed to be mediated by the radiation flux between fluid elements and the radiation field is in local thermal equilibrium with the fluid.

[4] This is only applicable for magnetic field configurations in which the magnetic field is sufficiently strong to contain the accretion flow everywhere.

[5] This assumption is not physically motivated in the modelling, because the deceleration from free-fall velocity occurs at the radiatiative shock. A self-consistent velocity and density profile does depend on x, e.g. because of the dependence of the shock height with x when following the prescription of the velocity profile given here. The more accurate computation of the hydrodynamical quantities is beyond the scope of this analysis (of the maximum luminosity) and I leave it as future work.

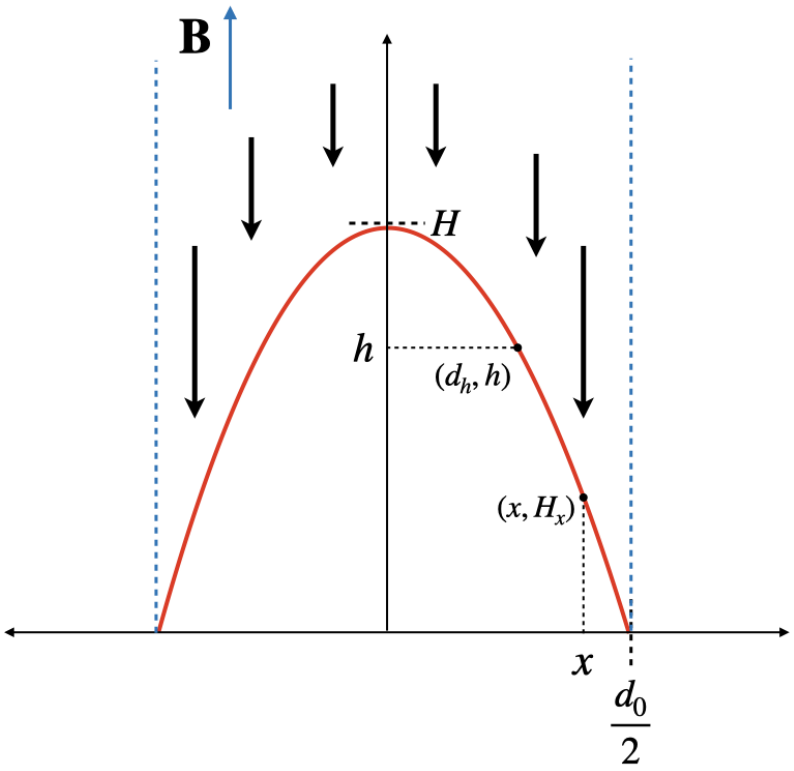

Figure 3.2: A diagram of the cross-section of the sinking region in the accretion column. The red lines show the location of the radiation shock. The blue-dashed lines show the magnetic field lines that confine the accretion flow. The blue arrow indicates the direction of the magnetic field and the black arrows indicate the direction of the accretion flow. The maximum shock height is labelled H and half of the column base width is labelled $d_0/2$. For a given x, the coordinates of the shock boundary in Cartesian coordinates are (x, H_x). Alternatively for a given $y = h$, the coordinates of the shock boundary in Cartesian coordinates are (d_h, h). Reprinted from Brice et al. (2021).

Accordingly, the simplified equations of hydrodynamics are given by

$$\rho v = \frac{\dot{M}}{2S_D}, \tag{3.2}$$

$$\frac{\partial P_{\rm rad}}{\partial h} = -\rho \frac{GM}{(R+h)^2}, \tag{3.3}$$

$$\frac{\partial F_{\parallel}}{\partial h} + \frac{\partial F_{\perp}}{\partial x} = 0, \tag{3.4}$$

where ρ is the plasma density; v is plasma velocity; $\dot{M}$ is the mass accretion rate; $P_{\rm rad}$ is the radiation pressure, which is isotropic due to the local thermal equilibrium assumption; M, R are the mass and radius of the NS respectively; $F_{\parallel}$, $F_{\perp}$ is the

parallel and perpendicular radiation flux respectively, which are obtained from the first moment of the radiative transfer equation and given by

$$F_{\parallel} = -\frac{c}{\bar{\kappa}_{\parallel}^{R}\rho}\frac{\partial P_{\rm rad}}{\partial h}, \tag{3.5}$$

$$F_{\perp} = -\frac{c}{\bar{\kappa}_{\perp}^{R}\rho}\frac{\partial P_{\rm rad}}{\partial x}, \tag{3.6}$$

where $\bar{\kappa}_{\parallel}^{R}$, $\bar{\kappa}_{\perp}^{R}$ are the angle and energy averaged Rosseland mean opacities in the direction parallel and perpedicular to the magnetic field lines respectively.

The parallel radiative flux in hydrostatic equilibrium is immediately obtainable from equations (3.3) and (3.5) together, namely

$$F_{\parallel}(x,h) = \frac{c}{\kappa_{\parallel}}\frac{GM}{(R+h)^2}, \tag{3.7}$$

which is consistent with the definition of the local Eddington flux. The perpendicular radiative flux is obtained by integrating the energy balance equation (3.4) with the boundary conditions

$$F_{\perp}(h)|_{x=0} = 0,\ F_{\perp}(h)|_{x=d_h/2} = F_{\perp,\rm esc}(h), \tag{3.8}$$

and applying the approximation $\partial_h F_{\parallel}$ is constant in x, which gives

$$F_{\perp} = F_{\perp,\rm esc}(h)\frac{2x}{d_h}. \tag{3.9}$$

Hence, the expressions for the radiation pressure are obtained by integrating the partial differential equations (3.5) and (3.6) with the boundary conditions

$$\begin{aligned} P_{{\rm rad},\parallel}(x)|_{h=H_x} &= \frac{2}{3}\frac{F_{\parallel}(x,H_x)}{c}, \\ P_{{\rm rad},\perp}(h)|_{x=d_h/2} &= \frac{2}{3}\frac{F_{\perp,\rm esc}(h)}{c}, \end{aligned} \tag{3.10}$$

which come from the assumption of negligible radiation flux entering the accretion column, i.e. for the boundary points, the moments of intensity are only integrated

over a hemisphere. This gives

$$P_{\mathrm{rad},\parallel}(x,h) = \int_h^{H_x} \rho \frac{GM}{(R+h)^2} \mathrm{d}y + \frac{2}{3}\frac{F_\parallel(H_x)}{c}, \tag{3.11}$$

and

$$P_{\mathrm{rad},\perp}(x,h) = \frac{F_{\perp,\mathrm{esc}}(h)}{c}\left[\frac{2}{d_h}\int_x^{d_h/2} \rho\,\kappa_\perp z \mathrm{d}z + \frac{2}{3}\right], \tag{3.12}$$

which are non-linear integral equations due to the dependence of the opacity terms, $\kappa_\parallel$ and $\kappa_\perp$, on the temperature.

3.1.1 Density profile

The equations for the radiative pressure (3.11) and (3.12) depend on the plasma density, which is obtained from the mass continuity equation (2.15) once the velocity profile is known. However, the velocity profile is undetermined in the simplified equations of hydrodynamics used to model the accretion column. Instead, following Mushtukov et al. (2015), a prescription is given, specifically the velocity profile is approximated by a power law in height:

$$v(h) = \frac{v_{\mathrm{ff}}}{7}\left(\frac{h}{H}\right)^{\xi}, \tag{3.13}$$

where the condition at the shock boundary is a deceleration from the free fall velocity, v_{ff}, to $v_{\mathrm{ff}}/7$, and in the later analyses $\xi = 1$ is used a fiducial value. By the mass continuty equation, the density profile is given by

$$\rho(h) = \frac{\dot{M}}{2S_D}\left(\frac{GM}{R}\right)^{-\frac{1}{2}}\left(\frac{49}{2}\right)^{\frac{1}{2}}\left(1+\frac{H}{R}\right)^{\frac{1}{2}}\left(\frac{H}{R}\right)^{\xi}\left(\frac{h}{R}\right)^{-\xi}. \tag{3.14}$$

The velocity vanishes at the NS surface, which results in an infinite density. Thus, this prescription is inadequate at close distances to the surface. In particular, at some point, the gas pressure becomes dominant over the radiation pressure. For the purposes of calculating the luminosity, the lowest point above the surface can be taken as the height where radiation pressure equals the gas pressure, since the

contribution to the total escaping flux from lower heights becomes negligible.

3.1.2 Accretion column geometry

Expressions for the plasma density through equation (2.15) and the radiation pressure in equations (3.11) and (3.12) depend on the accretion column geometry, in particular the quantities S_D, H_x, and d_h. In turn, since the accretion flow is channelled by the magnetic field lines, the accretion column geometry depends on the magnetic field topology close to the NS surface and the specific processes of the material loading from the disc onto the magnetic field lines at the magnetosphere, which I refer to in the following as the disc-magnetosphere interaction model.

The simplest disc-magnetosphere interaction model by Ghosh & Lamb (1978) proposes that the disc is not sharply truncated at the magnetosphere. Instead, due to magnetic turbulence, the disc penetrates into the magnetosphere resulting in a boundary region of finite width δ, whereupon the material is loaded onto the magnetic field lines and channelled to the magnetic poles. A diagram of the model is shown in figure 3.3.

Ghosh & Lamb (1978) give $\delta \sim H_m$, where H_m is the height of a thin Shakura & Sunyaev (1973) disc at the magnetosphere. This is the prescription used by Mushtukov et al. (2015) in their calculations of the maximum luminosity. However, for much of the model parameter space considered in this thesis (as is shown later in Fig. 3.14), the Shakura & Sunyaev (1973) disc is geometrically thick ($H_m \sim R_m$) and the prescription $\delta \sim H_m$ gives a boundary region width comparable to the magnetospheric radius. Such a disc-magnetosphere interaction model is unlikely to be physically realised because the assumptions made for the physical mechanism are not valid on these length scales.

To account for the geometrically thick disc without calculating the boundary region width self-consistently (which is beyond the scope of the work presented here), I introduced a parameterised upper limit to the boundary region width (Brice et al., 2021). Specifically, the boundary region width is limited so that $\delta < \zeta_{\max} R_m$, where $\zeta_{\max}$ is the parameter in question. The effects of changing $\zeta_{\max}$ to the accretion column geometry and maximum luminosity were studied in detail in Brice

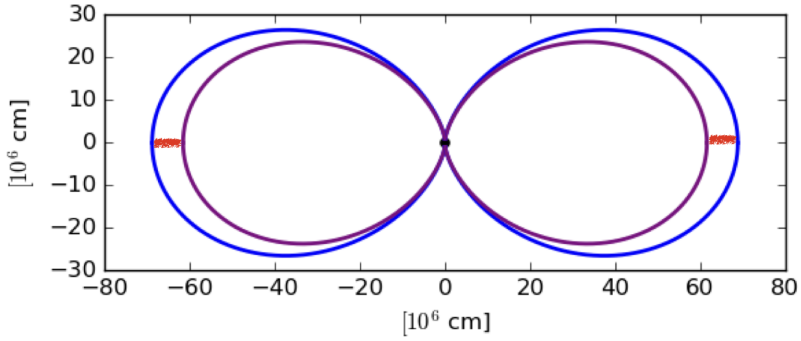

Figure 3.3: A cross-section plot of the magnetic field lines. The magnetic field consists of a dipole component and an octupole component with $\Gamma = 3$. The outer solid blue lines show the magnetic field lines that reach out to the magnetospheric radius. The inner purple solid lines show the magnetic field lines that reach to the inner radius of the boundary region. The red segments in between represent the disc that enters the boundary region. Reprinted from Brice et al. (2021)

et al. (2021) and is summarised in a later section.

After specifying the disc-magnetosphere interaction model, the accretion column geometry can be calculated by following the magnetic field lines from the outer and inner edge of the boundary region to the NS surface. The footprint of the magnetic field lines on the surface gives the accretion column base width, d_0, and the arc-length around the magnetic pole, l_0. The topology of the magnetic field lines close to the surface, i.e. $0 \leq h \leq R$, determines the expansion of the width and arc-length above the surface. For example, in the case of a pure dipole magnetic field, the accretion column width and the arc-length at height h above the surface are given by

$$d = d_0 \left(1 + \frac{h}{R}\right)^{3/2}, \; l = l_0 \left(1 + \frac{h}{R}\right)^{3/2} \tag{3.15}$$

respectively (Basko & Sunyaev, 1976; Mushtukov et al., 2015). In the case of a multipolar magnetic field, a numerical computation is required to obtain the appro-

priate indicies, which for a larger Γ differs more from the pure dipole case. Figure 3.4 shows examples for various magnetic field topologies of the numerically computed relationship between the accretion column dimensions and the height above the NS surface, which give the indicies α and β for l and d respectively. For these cases, the magnetic field topology is axisymmetric, thus the indicies satisfy $\alpha = \beta$. In general, the total surface area at a height h above the surface is given simply by

$$S_D = l_0 d_0 \left(1 + \frac{h}{R}\right)^{\alpha+\beta}. \tag{3.16}$$

3.1.3 Scattering opacity

The radiation pressure equations (3.11) and (3.12) depend on the Rosseland mean opacities $\bar{\kappa}^R_{\parallel}$ and $\bar{\kappa}^R_{\perp}$. In a strongly mangetised plasma, and assuming large Faraday depolarization, the radiation intensity is characterised by two normal modes: the ordinary (O) and extraordinary (X) mode, which have different scattering opacities that depend on the temperature and magnetic field strength. In this calculation of radiation field, the two normal mode treatment is approximated by neglecting mode exchange from scattering - treated by the first of equations (2.136). Instead, the intensity is assumed to be in a fixed ratio throughout the accretion column, namely a fraction f of the total radiation is in the X-mode. Hence, the Rosseland mean opacities for the total radiation field is obtained from summing the last two of equations (2.136), which gives

$$\frac{1}{\bar{\kappa}^R} = \frac{f}{\bar{\kappa}^R_-} + \frac{1-f}{\bar{\kappa}^R_+} \tag{3.17}$$

for each direction $\parallel$, $\perp$.

In principle, the equation of mode exchange from scattering can be used to calculate the coupled radiation fields and obtain the polarization degree, f, of the accretion column self-consistently. However, this would require changes to the computation scheme, which is beyond the scope of this study and would obfuscate the comparisons with the previous work of Mushtukov et al. (2015). For this rea-

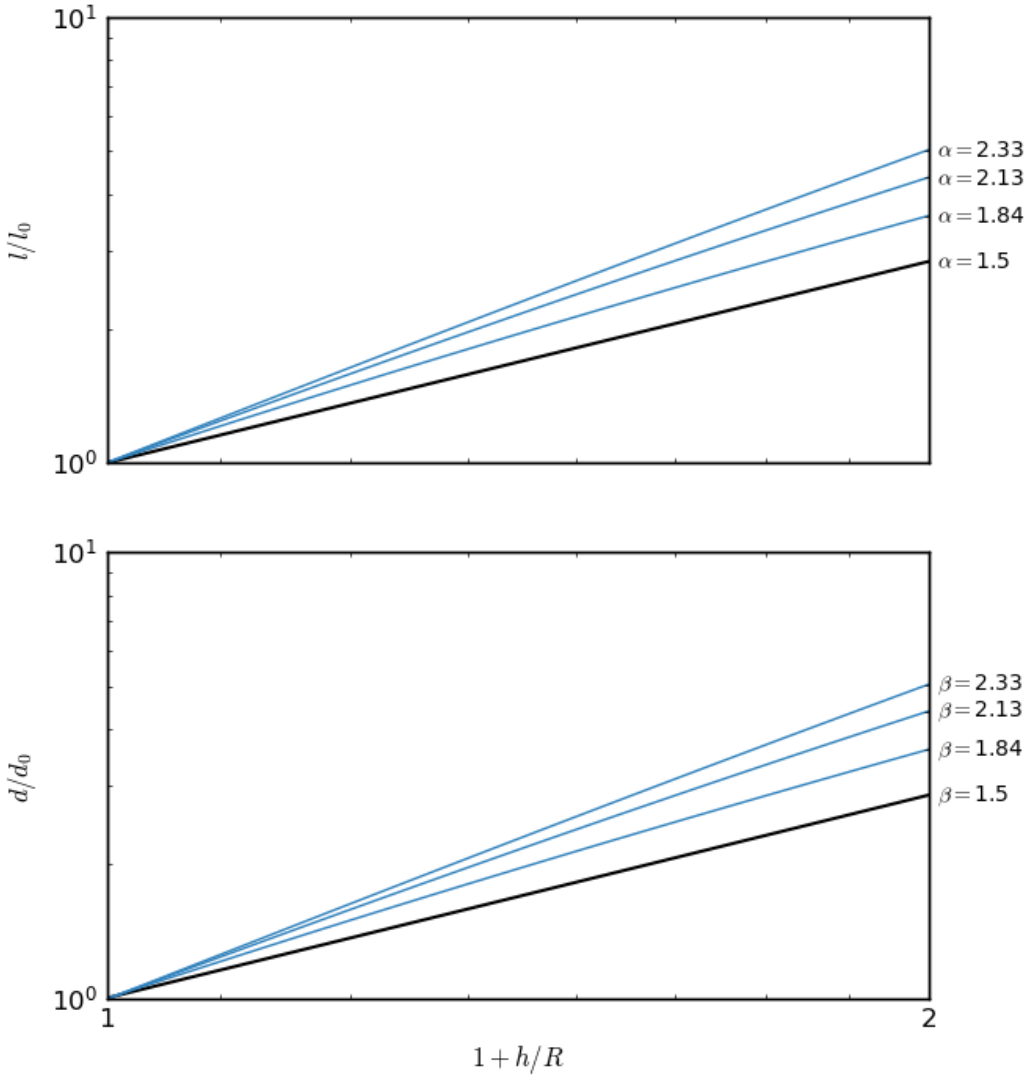

Figure 3.4: Plots of the (normalised) accretion column dimensions, l/l_0 and d/d_0, with respect to the height above the NS surface h. The black line in each plot shows the normalised dimensions in the case of a pure dipole magnetic field topology. The blue lines, from bottom to top in each plot, show the normalised dimensions in the case of a multipolar magnetic field comprised of a dipole component and octupole component with $\Gamma = 1,\ 3,\ 10$ respectively. Reprinted from Brice et al. (2021).

son, the approximate treatment of fixed polarization fraction was chosen. In §3.2.2, I discuss how a variation in the X-mode fraction affects the accretion column properties.

As previously mentioned, the Rosseland mean opacities $\bar{\kappa}_{\parallel}^{R}$ and $\bar{\kappa}_{\perp}^{R}$ depend on the temperature. Because the accretion column is optically thick, the assumption of local thermal equilibrium is used. In this case, the radiation pressure is related to the temperature by

$$P_{\rm rad} \approx \frac{u}{3} \approx \frac{aT^4}{3}, \tag{3.18}$$

where a is the radiation constant. This means that the equations (3.11) and (3.12) are implicit equations of the radiation pressure, which need an iterative computation to get a convergent solution. This is given in detail in §3.1.5.

Each step of the iterative computation involves a calculation of the Rosseland mean scattering cross-section, which is determined from the differential scattering cross-section. Mushtukov et al. (2015) use the magnetic Compton differential scattering cross-section to include the effects of higher cyclotron resonances (Harding & Lai, 2006). Alternatively, I use the magnetic Thompson differential scattering cross-section, neglecting both ion and vacuum contributions for simplicity as a first step (Brice et al., 2021), which can be easily included in future work. There is some loss in accuracy from neglecting the higher cyclotron resonances, although this is mitigated by the low number of energetic photons that would be scattered above the fundamental resonance for the magnetic field strengths of interest in the PULX models. In addition, the energy redistribution in the Compton differential scattering cross-section are neglected anyway by assumption of local thermal equilibrium for the radiation field.

3.1.4 Model estimates

An estimate of the radiation pressure, shape, and luminosity of an accretion column can be made for a sinking region with constant density profile $\rho(h) = \rho$, and constant opacities $\bar{\kappa}_{\parallel}^{R}$, $\bar{\kappa}_{\perp}^{R}$. In this case, the radiation pressure equations (3.11) and

(3.12) can be integrated analytically to give

$$P_{\mathrm{rad},\parallel}(x,h) = \rho \frac{GM}{R}\left[\frac{H_x/R - h/R}{(1+h/R)(1+H_x/R)} + \frac{2}{3}\frac{1}{\rho\bar{\kappa}_{\parallel}^{R}R}\frac{1}{(1+H_x/R)^2}\right] \tag{3.19}$$

and

$$P_{\mathrm{rad},\perp}(x,h) = \frac{F_{\perp,\mathrm{esc}}(h)}{c}\left[\rho\bar{\kappa}_{\perp}^{R}d_h/4\left(1-(2x/d_h)^2\right)+2/3\right], \tag{3.20}$$

where only the functions H_x and d_h are left to be determined. In equations (3.19) and (3.6), the vertical optical depth of the accretion column is given by $\rho R\bar{\kappa}_{\parallel}^{R}$, while the horizontal optical depth of the accretion column is given by $\rho\bar{\kappa}_{\perp}^{R}d_h/2$.

The expression for the normalized escaping flux can be obtained from $P_{\mathrm{rad},\parallel}(x=0,h) = P_{\mathrm{rad},\perp}(x=0,h)$. For $h=0$, this gives

$$\frac{F_{\perp,\mathrm{esc}}(h=0)}{c} = \rho\frac{GM}{R}\left[\frac{\frac{H/R}{(1+H/R)}+\frac{2}{3}\frac{1}{\rho\bar{\kappa}_{\parallel}^{R}R}\frac{1}{(1+H/R)^2}}{\rho\bar{\kappa}_{\perp}^{R}d_h/4+2/3}\right]. \tag{3.21}$$

As done by Mushtukov et al. (2015), assuming $H_x/R \ll 1$ gives the relation

$$H_x/R \propto -x^2. \tag{3.22}$$

Thus, the shape of the shock in this simplified case is approximately quadratic near the base of the column and becoming less so near the top.

The luminosity of the column is obtained by integrating the escaping flux over the surface of the column, which gives

$$L = 4l_0\int_0^H\left(1+\frac{h}{R}\right)^{\beta}F_{\perp,\mathrm{esc}}(h)\mathrm{d}h, \tag{3.23}$$

which is not integrable analytically due to the dependence of d_h on h. However, a lower bound for the luminosity can be obtained by setting $d_h = d$, i.e. approximating the horizontal optical depth of the accretion column to be its maximum at all heights. Because the accretion column is optically thick, i.e. $\rho\kappa_{\perp}d_h \gg 1$ and $\rho\kappa_{\parallel}R \gg 1$, then

the lower bound luminosity is approximately given by

$$L \approx \frac{4}{\pi}\left(\frac{l_0}{d_0}\right)\left(\frac{\kappa_\perp}{\kappa_\parallel}\right) f(H/R) L_{\rm Edd}, \tag{3.24}$$

where

$$f(H/R) = \frac{1}{1+H/R}\left[(1+H/R)\log(1+H/R) - H/R\right]. \tag{3.25}$$

This result was obtained previously by Mushtukov et al. (2015). However, in this work, I have recovered the result for any magnetic field configuration that satisfies $\alpha = \beta$, which is true for any axially symmetric magnetic fields. Equation (3.24) gives an approximate relation between the luminosity and the accretion column base geometry, which was noted by Basko & Sunyaev (1975). In addition, as previously discussed by Mushtukov et al. (2015), the function $f(H/R)$ grows only logarithmically for large H/R, which sets a natural scale for the maximum luminosity for when $H/R = 1$, i.e. the maximum luminosity is defined as the accretion luminosity for which $H = R$.

3.1.5 Computation scheme

A particular accretion column model is specified by its input parameters, which are the NS mass M, the NS radius R, the accretion luminosity $L_{\rm acc} = GM\dot{M}/R$, the velocity power-law index ξ, the polarization degree f, the disc boundary region width upper bound $\zeta_{\rm max}$, and the strength of the magnetic field components at the NS surface.

The output of the computation for a particular model is a radiation pressure profile and the accretion column geometry, in particular the accretion column height H. If $H < R$, the accretion luminosity parameter for the model is considered below the maximum luminosity, conversely if $H > R$, the accretion luminosity parameter is considered above the maximum luminosity.

The procedure for computing a radiation pressure profile for the accretion column model is to numerically integrate the radiation pressure equations (3.11) and

(3.12). However, because of the dependence of the opacity terms, $\bar{\kappa}_{\parallel}^{R}$ and $\bar{\kappa}_{\perp}^{R}$, on the temperature - which itself depends on $P_{\rm rad}$ through equation (3.18) - the numerical integration must be done iteratively until convergence of the radiation pressure profile. The initial temperature distribution is taken from the estimated model, as in §3.1.4, with a guess height H' and with the opacity set to the (unmagnetised) Thompson scattering opacity.

Convergence of the radiation pressure profile is checked by proxy: the luminosity given by equation (3.23) is within 1 per cent of the previous calculated luminosity. The calculated luminosity is not checked against the accretion luminosity because these are different unless the guess height is the height of the accretion column. An outer iteration on the guess height H' is needed until the (converged) calculated luminosity matches the accretion luminosity input parameter.

3.2 Numerical Results

3.2.1 Effects of the magnetic field strength and topology

In this section, I describe how changes in the magnetic field strength and topology affect the accretion column properties, due to the changes they produce in the opacities. The model has a magnetic field configuration made up of two components: a dipole component and higher-degree multipole component. As a first step for this work, I examine only magnetic field configurations that consist of a dipole component plus an octupole component. The octupole degree was chosen over the quadrupole degree to better localize the change to the magnetic field topology to the NS surface and avoid potential problems with null points of the magnetic field above the magnetic poles. In principle, other multipole degrees can be used in the model.

To understand the effects of a change in the magnetic field strength, I computed a series of models with different octupole component strengths while keeping other model input parameters fixed. The effects due to an induced change in the accretion column geometry are separated from the induced change in opacity by first using only the accretion column base quantities l_0 and d_0 from a pure dipole magnetic field

topology (irrespective of the contribution from the octupole component). For these models, the curvature of the magnetic field lines is also neglected, i.e. $\alpha = \beta = 0$.

The numerical results for two sets of models, which correspond to different values used for the accretion luminosity parameter and the dipole component strength, are shown in black in figures 3.5 and 3.6. In particular, figure 3.5 shows the shock height above the surface as a function of the depth, i.e. half of the vertical cross-section of the accretion column. Figure 3.6 shows the profiles (in height above the surface) of the central internal temperature, the effective temperature, and the perpendicular mean opacity in the accretion column. These properties were chosen in particular for easy comparison with Mushtukov et al. (2015), in which the magnetic field topology was assumed to be a pure dipole.

For a more self-consistent treatment of the effects of a multipolar magnetic field, l_0 and d_0 must be calculated according to the magnetic field topology. In general, the base size and depth of the accretion column differs from those of a pure dipole topology (as previously discussed in §3.1.2). This difference affects the plasma density, the internal temperature, the escaping flux, and the maximum shock height. I computed a second set of models to study the effects from a change in the accretion column base size and depth (using the approach detailed in §3.1.2). For these models, the curvature of the magnetic field lines is taken into account through the parameters α and β. The numerical results are shown by the red lines in figures 3.5 and 3.6, alongside the results for models with fixed accretion column base geometry.

Comparison of the computed maximum shock height H with those from Mushtukov et al. (2015) show that the values of H presented in this work are smaller. This may be due to a difference in the calculation of the opacity (see §3.1.3). However, the trends in the internal temperature profile, the effective temperature profile, and the opacity profile of this model are similar to the trends shown by Mushtukov et al. (2015), even when accounting for the magnetic field topology in the accretion column geometry. This indicates that the introduction of multipole components affects the quantitative details of the results without introducing new physical effects from

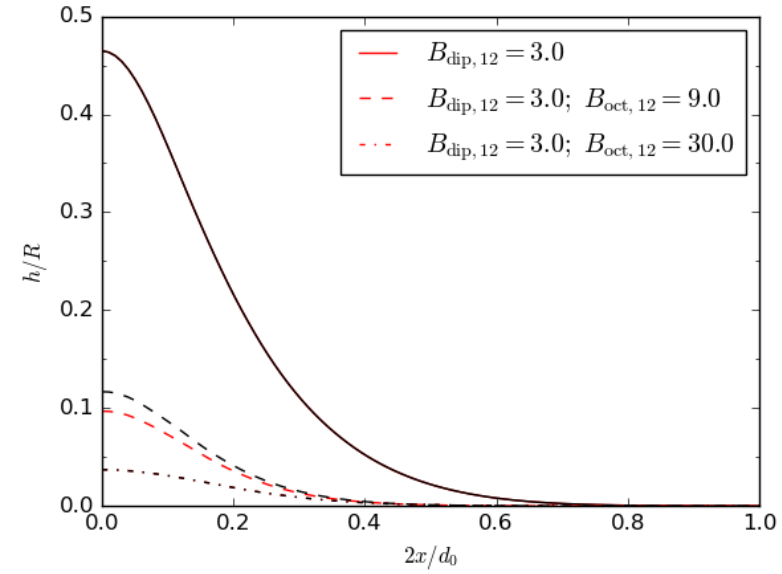

(a)

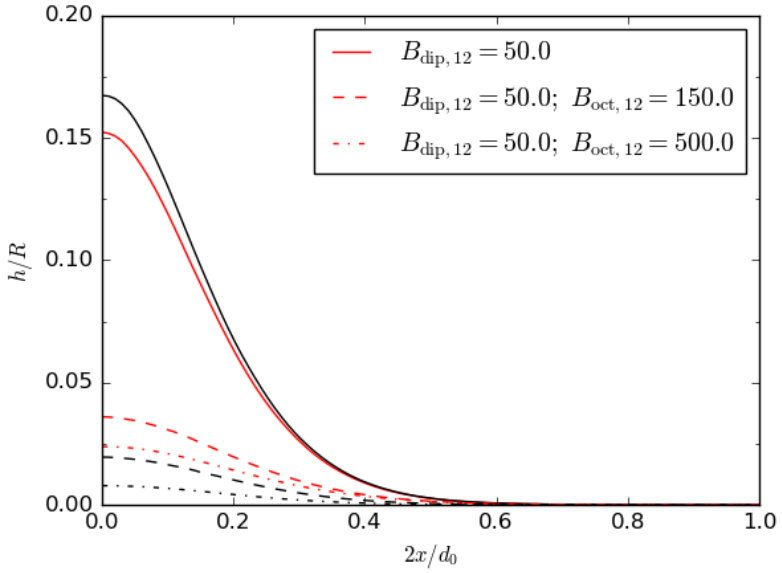

(b)

Figure 3.5: The normalised shock height of the accretion column as a function of the normalised accretion column width. In (**a**), the models used $L_{39} = 1.0$. The black lines show results for models with fixed accretion column base geometry variables $l_0 = 7.6 \times 10^5$cm and $d_0 = 1.4 \times 10^4$cm, which corresponds to a surface dipole field strength of 3×10^{12}G. In (**b**), the models used $L_{39} = 10.0$ and the black lines show results for models with fixed accretion column base geometry variables $l_0 = 4.7 \times 10^5$cm, and $d_0 = 4.5 \times 10^4$cm, which corresponds to a surface dipole field strength of 5×10^{13}G. For both subfigures, the other model parameters used were $\xi = 1$ and $f = 1.0$. The red lines show results for models with accretion column base geometry variables that are consistent with the corresponding magnetic field topology.

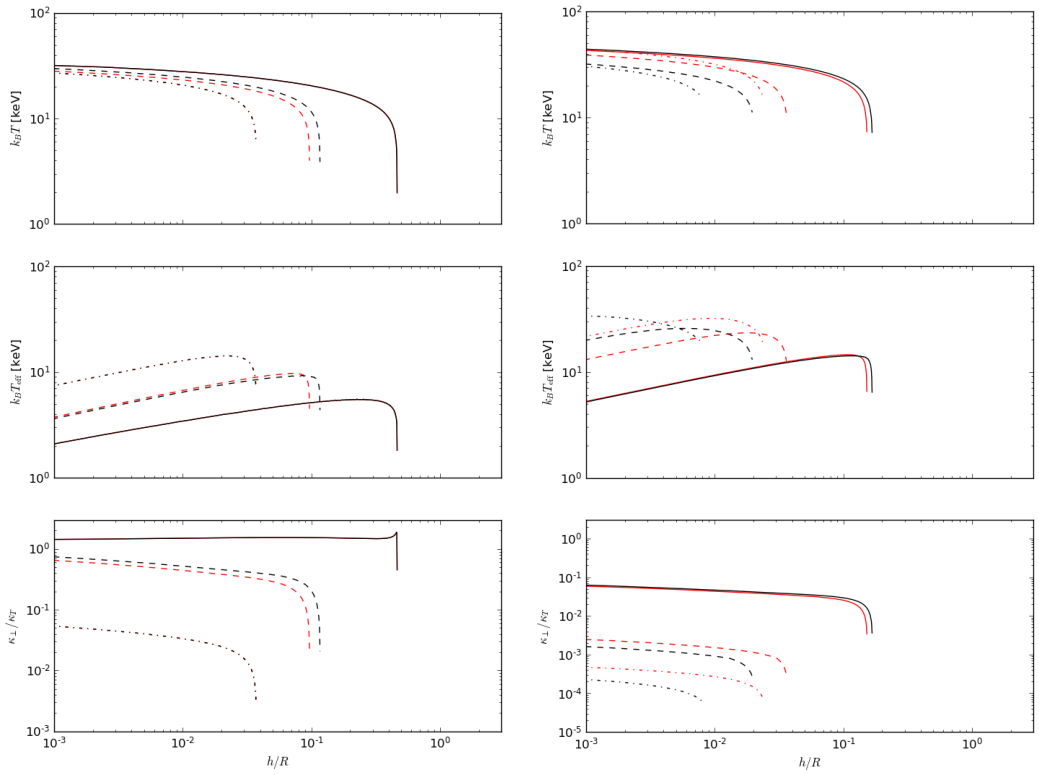

(a) **(b)**

Figure 3.6: Values for various properties of the accretion column as a function of normalised height above the NS surface. The set of models in each subfigure correspond to the models in figure 3.5. From top to bottom, the plots show the internal ($x = 0$) temperature profile, the effective temperature of the emitted radiation, and the perpendicular mean opacity $\bar{\kappa}_\perp^R$ (see text for details).

the geometric compression of the accretion column.

The first observation from figure 3.5 is that the shape of the shock is not quadratic in x [6] but instead the accretion column is quite narrow. The height of the shock above the surface drops to practically zero at a certain width $\tilde{x}$, which I refer to as the sinking region width. This is the width at which the radiation pressure at the base becomes equal to the Eddington flux pressure, i.e. $P_{\rm rad}(\tilde{x}, h_0) = \frac{2}{3} F_{\rm Edd}(h_0)/c$. For $x > \tilde{x}$, the radiation pressure at the base is smaller than the Eddington flux pressure and no shock above the surface can be supported.

[6] This was noted by Mushtukov et al. (2015).

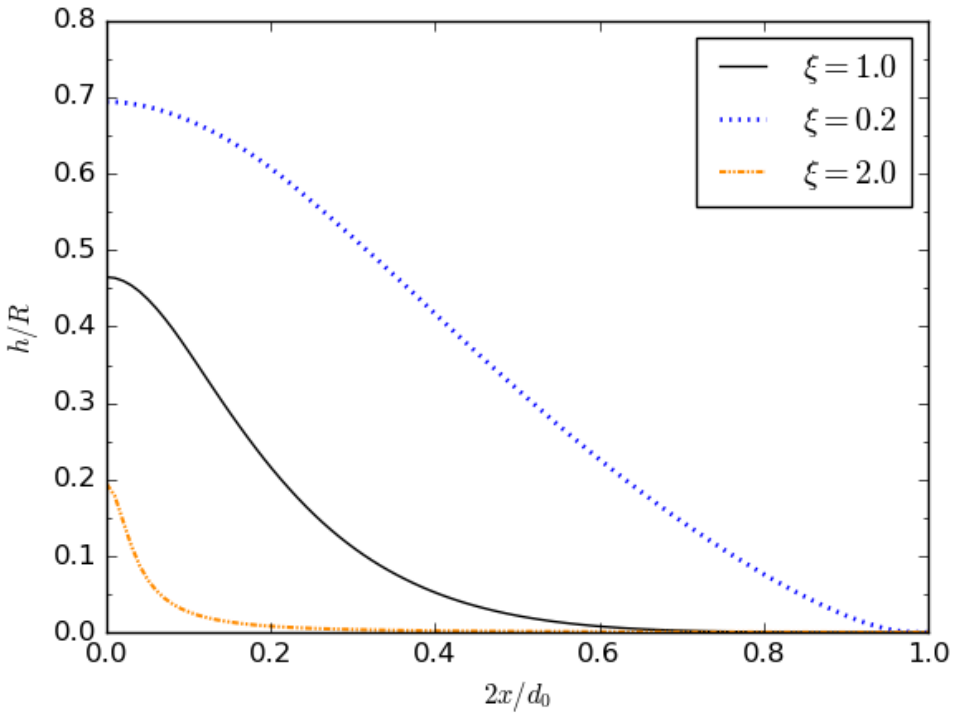

Figure 3.7: The normalised shock height of the accretion column as a function of the normalised accretion column width. The black solid line, blue-dotted line, and orange dot-dashed line correspond to models with $\xi = 1.0,\ 0.2,\ 2.0$ respectively. The models used $L_{39} = 1.0$, $B_{\rm dip} = 3 \times 10^{12}$G and $B_{\rm oct} = 0$, $f = 1.0$.

The radiation pressure at coordinates (x, h_0), i.e. some distance along the accretion column base, determines the height of the shock at x, H_x, by equation (3.11). Thus, the radiation pressure profile along the column base determines the shape of the shock. $P_{\rm rad}(x, h_0)$ is determined by equation (3.12), in which the function $F_\perp$ was assumed to be a linear function in x. A different choice for $F_\perp$ gives a different shock shape.

Because $F_\perp$ depends on the density profile, one way to modify this function is by changing the velocity index ξ. Figure 3.7 shows a series of models with varying velocity index. As expected, the shallow velocity profile results in a similar shock shape to the analytical model, which predicts a quadratic shock shape from a constant density profile. On the other hand, when a velocity index $\xi > 1$ is used, the sinking region becomes narrower. This is a consequence of the greater deceleration of the particles in the lower layers of the accretion column. The upshot is that the

radiation energy released by the particles is concentrated in the lower layers, which results in a lower shock height.

Figure 3.5 shows that the maximum shock height H decreases for an increasing surface magnetic field strength. By reversing the argument, for a mixed maximum shock height, a higher luminosity can be obtained by increasing the strength of the multipolar component. In turn, this reduces the X-mode opacity, which allows for radiation to more readily escape from the sides of the accretion column. As a result, a smaller maximum shock height is sustained from the vertical radiation pressure.

The internal central radiation temperature profile is also anti-correlated with the magnetic field strength (e.g. see the top plots of figure 3.6). This is because models with a stronger magnetic field have a lower H, which means the accreting material is decelerated closer to the NS surface by the shock. Hence, by continuity, the density in the sinking region is lower, and in turn the internal radiation temperature is lower.

The effective temperature, $T_{\rm eff}$, obtained from the escaping flux using $F_{\perp,\rm esc} = \sigma T_{\rm eff}^4$, is shown in figure 3.6. As already noted by Mushtukov et al. (2015), this quantity does not reflect the radiation temperature directly. Instead, $T_{\rm eff}$ increases with increasing height above the NS surface and drops near the top of the accretion column. At the bottom of the accretion column, both the density, ρ, and the geometrical thickness of the sinking region, d_h, are large, which results in a large horizontal optical depth and a smaller escaping flux in that direction. Higher up, the accretion column becomes smaller in size, and the horizontal layers have a lower optical depth. The optical depth reduces more than the central temperature. This is why the effective temperature generally increases with height in the deeper regions. In fact, the peak of the effective temperature profile identifies the altitude at which the escaping flux is greatest, and in turn this depends on the prescription for the density profile. For the accretion columns with velocity index $\xi = 1$, the effective temperature peak is close to the maximum shock height, where the optical depth is lower. For $\xi < 1$, the peak in $T_{\rm eff}$ is at a lower altitude than when $\xi = 1$.

The perpendicular Rosseland mean opacity $\bar{\kappa}_\perp^R$, (shown in figure 3.6) is cal-

culated at the central plane of the sinking region, $x = 0$. This quantity depends on both the total magnetic field strength in the accretion column and the temperature. In general, a higher magnetic field strength or lower temperature reduces the perpendicular Rosseland mean opacity. However, it is not a monotonic increasing function of temperature or magnetic field strength. In fact, it is largest when the photons in the sinking region have energies close to the electron cyclotron resonance energy.

Comparing the models with fixed column base geometry (the black lines in figures 3.5 and 3.6) and models including the curvature calculation (the red lines in figures 3.5 and 3.6), it is evident that there are no simple trends, which explain the changes from the black cures to the red ones. This is because the change in the accretion column base geometry (which decreases when the strength of the multipole component is increased) results in a geometric compression of the accretion column into a smaller area, whereas the change in the curvature of the mangetic field lines results in an increase of the accretion column area higher up in the accretion column. For each model, the overall outcome of these competing effects is different. However, the change in the accretion column properties is modest and does not affect the qualitative behaviour discussed so far.

The effect of including the column geometry is easier to explain in the models with multipolar magnetic fields, shown in figures 3.5(b) and 3.6(b), which are low enough in height that the curvature does not make a substantial difference and the main effect is the reduction in the base size. For these models (in red), the internal temperature at a given height in the sinking region is increased compared with the fixed base geometry models (in black), since the same amount of energy is produced in a smaller area, and the perpendicular mean opacity rises following this increase in the internal temperature. In addition, the density of the sinking region is increased, which makes it more difficult for the radiation to escape from the sinking region, hence decreasing the effective temperature.

On the other hand, the effect of the curvature alone can be understood by comparing the purely dipole models with $B_{\rm dip} = 5 \times 10^{13}$G [figures 3.5(a) and 3.6(b)]. In this case, the accretion column base area is unchanged, since there are no mul-

tipolar magnetic fields, and the density is sufficiently high that the change in area due to the curvature is a significant factor. For this model (in red), the density of the accreting plasma is lower near the top compared with the fixed base geometry model (in black), and this subsequently decreases the perpendicular mean opacity, allowing for more radiation to escape. Hence, a lower maximum shock height is sustained. At lower field strengths, [as for $B_{\rm dip} = 3 \times 10^{12}$G, figures 3.5(a) and 3.6(b)], the density inside the column is not high enough, hence this effect is not substantial.

3.2.2 Mixed polarization

So far, only the models with polarization degree $f = 1$ have been considered. However, a more complete description of the radiation field in the accretion column includes a mix of X-mode and O-mode photons as well as scattering between the normal modes. Solving this problem self-consistently requires a complete angle and frequency-dependent solution of the radiative transfer problem, which is not the purpose of this work. Instead, to understand whether super-Eddington emission is possible when there is a substantial fraction of O-mode photons, I compute a series of models with various fixed polarization degree f throughout the entire accretion column.

In general and as expected, when a fixed fraction of O-mode photons is introduced (and all other model parameters are held constant in the comparison), the total opacity increases (as shown in the bottom plot of figure 3.9). However, even with a significant fraction of O-mode photons ($f = 0.3$), the average perpendicular mean opacity is still well below the Thomson scattering opacity in the cases considered here. Solutions with a luminosity well above the Eddington limit are still possible but a higher shock height H is sustained because the opacity is greater. This results in a higher internal temperature and lower effective temperature. A set of fixed X-mode fractions, $f = 1, 0.7, 0.3$, was used to illustrate the effect of changing polarization degree. Figure 3.8 shows the accretion column shock shape and figure 3.9 shows the internal temperature, effective temperature, and perpendicular effective opacity profiles respectively for the corresponding model.

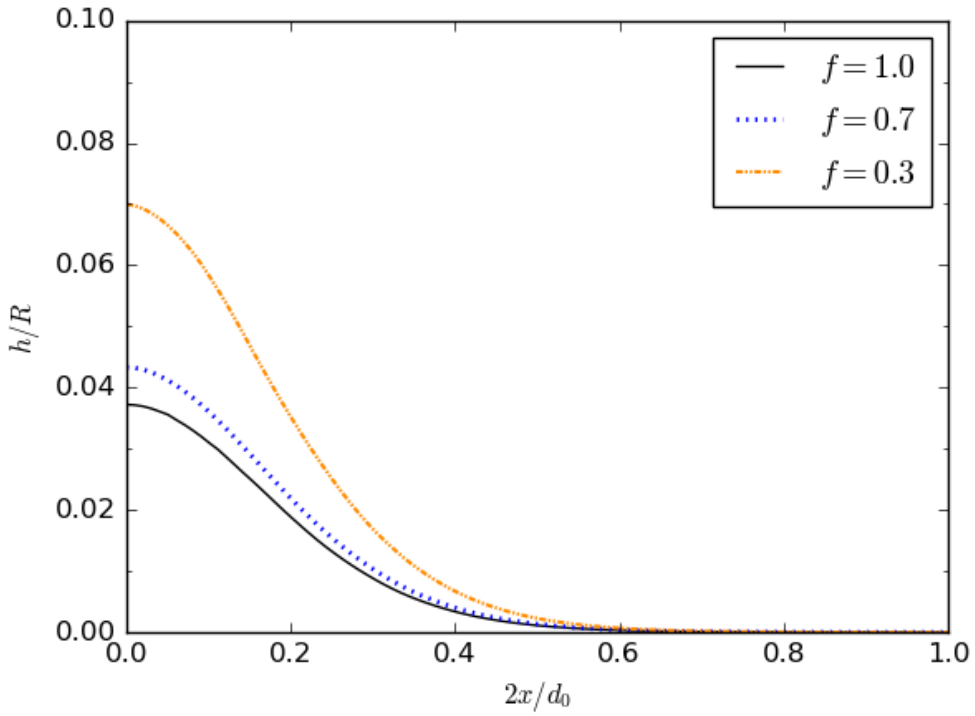

Figure 3.8: The normalised shock height of the accretion column as a function of the normalised accretion column width. From top to bottom, the curves correspond to different values of the polarization degree: $f = 0.3$ (orange dot-dashed line), $f = 0.7$ (blue dot-dashed line), $f = 1.0$ (the black solid line). The models used $L_{39} = 1.0$, $B_{\rm dip} = 3 \times 10^{12}$G, $B_{\rm oct} = 3 \times 10^{13}$G, and $\xi = 1.0$.

For low magnetic field strengths ($B < 10^{13}$G), the opacity decreases when a fraction of O-mode photons is included. This occurs when a large portion of the photons have energy close to or higher than the electron cyclotron resonance energy, $E_{\rm cycl} \approx 11.6\ B_{12}$ keV. However, this work focuses on modelling an environment with high magnetic field strengths ($B > 10^{13}$G), in which case most photons have energies well below $E_{\rm cycl}$.

3.2.3 Disc-magnetosphere interaction

In these models, the magnetospheric radius depends on a dimensionless parameter Λ, and the width of the boundary region depends on the prescription for ζ (see section §3.1.2 for details). However, both the value of Λ and the expression for ζ are poorly known, especially in the novel context of super-Eddington mass transfer rates. Thus, to test the robustness of the model results, I examined the response of

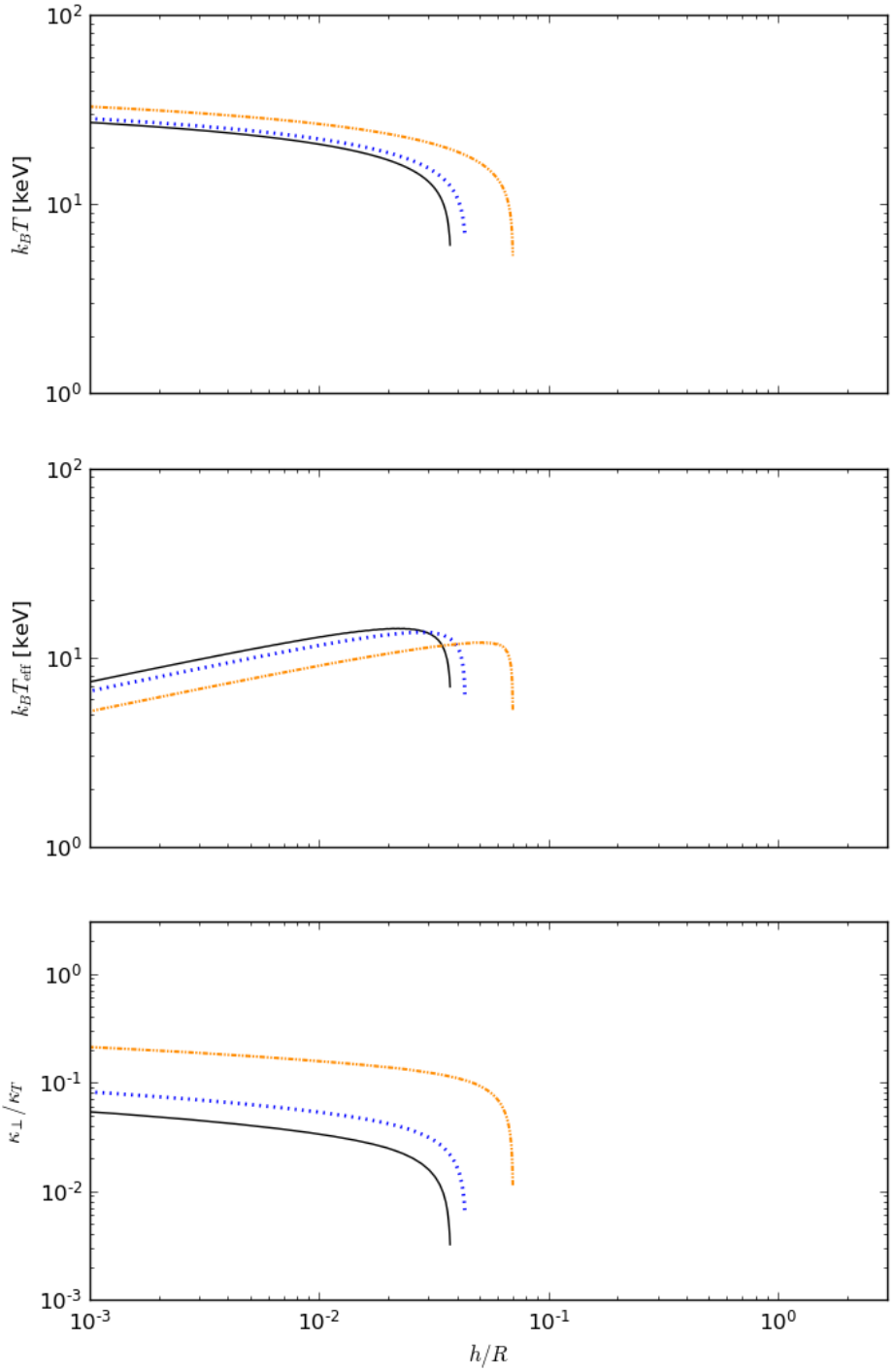

Figure 3.9: Values for various properties of the accretion column as a function of the normalised height above the NS surface. The set of models correspond to the set in figure 3.8. From top to bottom, the plots show the central internal temperature, the effective temperature profile of the emitting radiation, and the perpendicular mean opacity, respectively.

the accretion column base geometry quantities, l_0 and d_0, to changes in Λ and ζ.

For the models presented prviously, the canonical disc accretion value of $\Lambda = 0.5$ (Ghosh & Lamb, 1978) was used. However, the exact value of Λ depends on the extent to which the NS magnetic fields threads the accretion disc (Wang, 1987) and for example Dall'Osso et al. (2016) suggest Λ in the range $0.3 - 1.0$ as a conservative estimate of the possible values. By varying the value of Λ across this range, l_0 changes by less than an order of magnitude. Since $L \propto l_0$ and $\rho \propto S_D^{-1}$, the accretion column properties are not very sensitive to different values of Λ.

With regards to ζ, the boundary region width was assumed to be proportional to the disc height, as done by Mushtukov et al. (2015). According to this prescription, ζ is given by

$$\zeta = \frac{\kappa_{\rm T}}{c}\frac{3}{8\pi}\frac{\dot{M}}{R_m} \approx 0.2 L_{39}^{9/7} B_{\rm d,12}^{-4/7}. \tag{3.26}$$

However, since many of the models studied in this work have a large accretion luminosity (with $L_{39} \sim 10$) and low dipole magnetic field strengths (with $B_{\rm d,12} \sim 1$), the value of ζ can be close to or in excess of unity. These values of ζ correspond to a boundary region width of the size of the entire magnetosphere, which is a physically unlikely scenario. Thus, I introduced a maximum value of ζ by hand, i.e. $\zeta_{\rm max}$, which constrains d_0 as a result. For $\zeta < \zeta_{\rm max}$, the value of ζ is governed by equation (3.26).

Alternatively, a self-consistent approach is to introduce a new prescription for ζ based on some set of physical principles, such as was done by Li & Wang (1999). However, this would require extending disc-magnetosphere interaction models to the case of a geometrically thick disc, which is not the purpose of this work. Hence, as a substitute to considering many different prescriptions, I tested the response of d_0 to variations in ζ, without assuming a particular prescription as in equation (3.26). To do this, d_0 is calculated for various ζ in the range from $0.0 - 1.0$. In each case, the accretion luminosity and magnetic configuration are fixed. The models had fixed input parameters: $L_{39} = 1.0$, $B_{\rm d,12} = 3$, $B_{\rm oct} = 0$. The results are shown in figure 3.10.

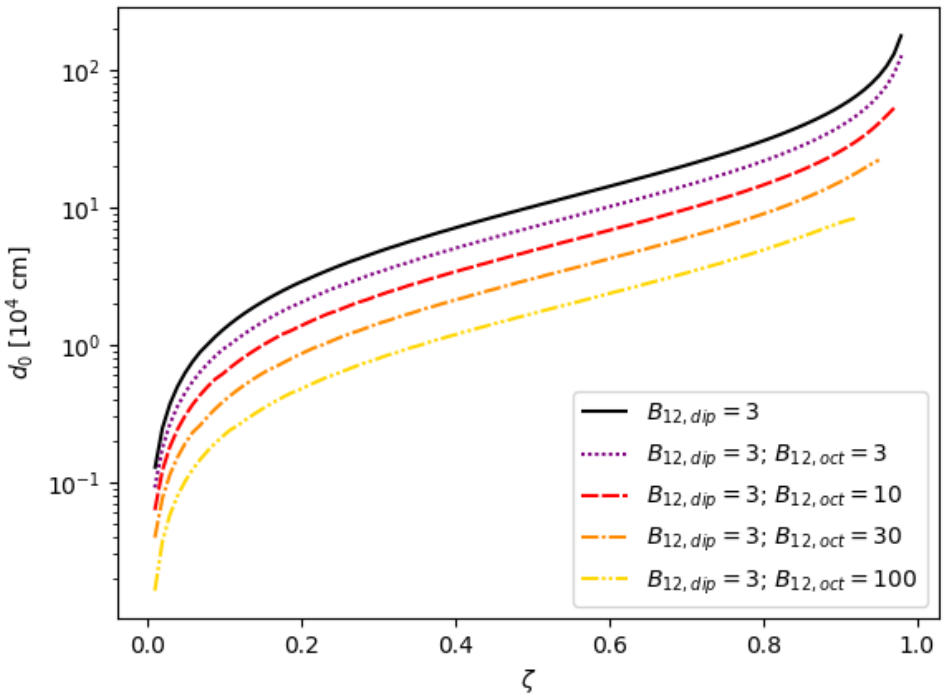

Figure 3.10: The accretion column base width, d_0, in units of 10^4cm as a function of ζ. The lines correspond to different magnetic field configurations, as specified in the legend. The model used $L_{39} = 1.0$.

Across the range of ζ, the change in d_0 can be an order of mangitude or more. Since $F_{\perp,\mathrm{esc}} \propto d_0^{-1}$ (see §3.1.4), the luminosity of the accretion column is sensitive to the changes in ζ. Hence, different prescriptions for ζ can lead to dissimilar results for the accretion column properties, in the particular the maximum luminosity.

3.2.4 Maximum luminosity

The central aim of this work is to calculate the maximum luminosity from a highly magnetised, accreting NS, given a set of assumptions (e.g. the magnetic field configuration). In order to calculate the maximum luminosity that can be sustained in the accretion column, the maximum accretion luminosity, L_{acc}, is computed for a model while fixing the maximum shock height $H = R$. In fact, at higher accretion column heights, the luminosity still increases but the growth is logarithmic (see §3.1.4) and the curvature of the magnetic field lines affects the vertical pressure balance equation (3.3), making the approximations unsuitable. Here, the calculation

for the maximum luminosity is repeated for several magnetic field configurations, namely a pure dipole field, a field with $B_{\rm oct} = 3B_{\rm dip}$, and a field with $B_{\rm oct} = 10B_{\rm dip}$, while other model parameters have been fixed at $\xi = 1$, $f = 1$, $\zeta_{\rm max} = 0.2$.

In agreement with the findings of Mushtukov et al. (2015), the value of the maximum luminosity is mainly dictated by the accretion column geometry for models with total magnetic field strengths $B < 10^{13}$G. This is because at the internal temperatures typical of the accretion column and for these low magnetic field strengths, most of the photons have $E > E_{\rm cycl}$ and therefore are not subject to reduction in opacity induced by the magnetic field. For higher total magnetic field strengths, $B > 10^{13}$G, the scattering opacity of the X-mode is instead significantly reduced, such that this becomes the determining factor in constraining the maximum luminosity. This can be seen from the change in slope of the maximum luminosity line in figure 3.11.

The (initial) decreasing trend in the maximum luminosity for increasing magnetic field strengths up to 10^{13}G can be explained by an increase in the temperature of the accretion column. Since the accretion column becomes thinner for higher magnetic field strengths (due to the choice of $\zeta_{\rm max} = 0.2$, the temperature increases, which also increases the overall scattering opacity.

As expected, when a multipole component is included that is stronger than the dipole component, the maximum luminosity is increased. This is because of the increase in the total magnetic field strength at the surface (i.e. in the accretion column). The maximum luminosity for a multipolar magnetic field is similar to the maximum luminosity for a pure dipole field with the same total surface magnetic field strength. Thus, the change to the accretion column geometry due to the presence of a higher order multipole does not affect the maximum luminosity in a significant way (at least for the models presented in this work). Instead, the maximum luminosity is more sensitive to the change in accretion column geometry due to the disc-magnetosphere interaction model.

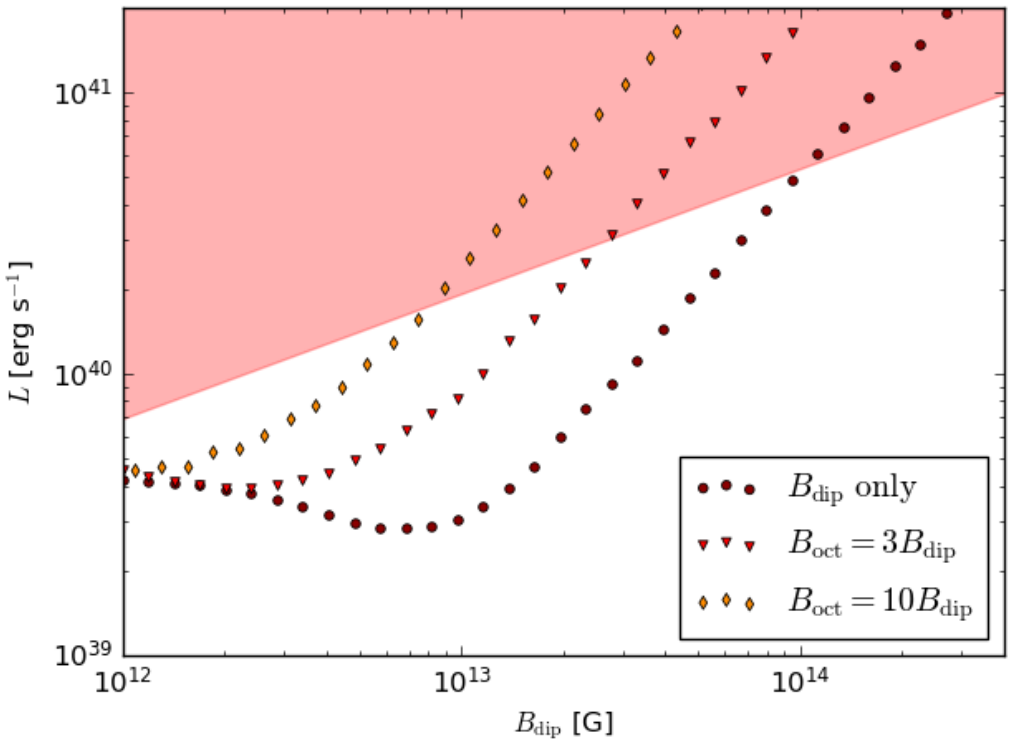

Figure 3.11: Maximum luminosity as a function of the dipole component strength at the NS surface. The circle, triangle, and diamond points show the computed maximum luminosity for models with a fixed magnetic field configuration: pure dipole, $\Gamma = 3$, and $\Gamma = 10$ respectively. The red-shaded area indicates the region for which the accretion luminosity exceeds the NS Eddington luminosity, i.e. when the accretion flow is super-Eddington.

3.2.4.1 Maximum luminosity with mixed polarization

Models with a mixture of polarization modes has different accretion column properties from models with $f = 1$. Thus, the maximum luminosity is also calculated for a models with a fixed polarization degree $f = 0.7$, which is expected in a more realistic case for scattering dominated models). Figure 3.12 shows the results. As the maximum shock height is typically increased, the maximum luminosity is lower than in the pure X-mode case. However, this trend is reversed for the magnetic field strengths below $\sim 10^{13}$G because the O-mode photons decrease the average Rosseland mean opacity when a large portion of the photons have energy close to or higher than the electron cyclotron energy, $E_{\rm cycl}$.

Otherwise, from figure 3.12, the (interpolated) relation between the maximum

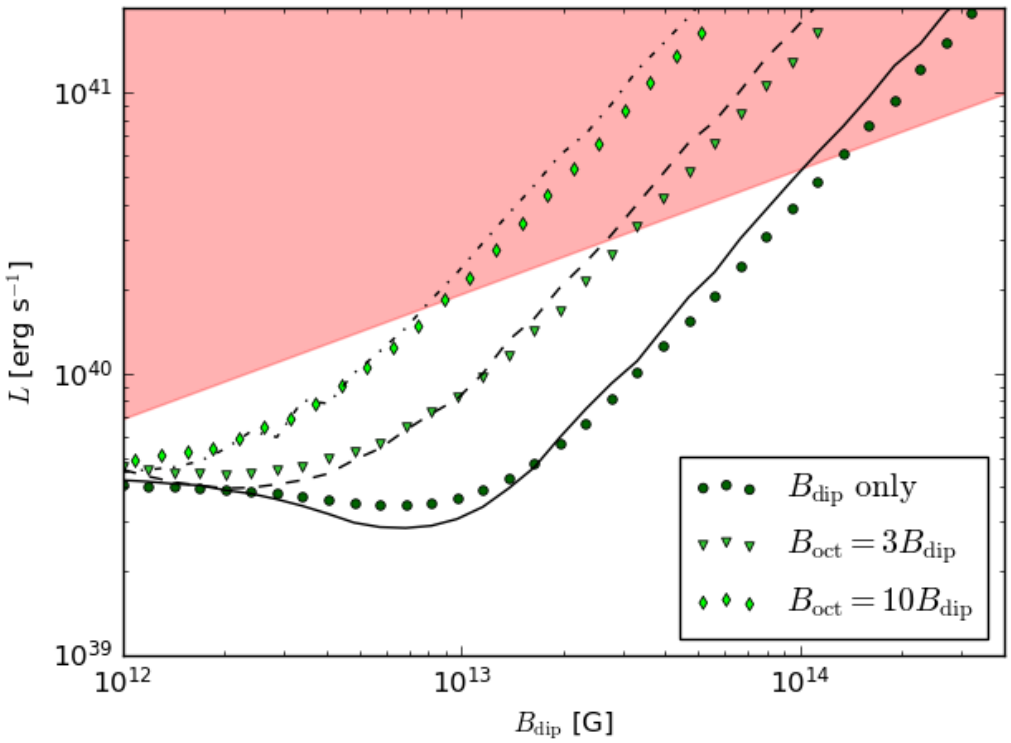

Figure 3.12: The maximum luminosity as a function of the dipole component strength at the NS surface. The circle, triangle, and diamond points in green show the computed maximum luminosity for models with a fixed magnetic field configuration: pure dipole, $\Gamma = 3$, and $\Gamma = 10$ respectively, and with a fixed polarization degree $f = 0.7$. The solid, dashed, and dot-dashed black lines show the (interpolated) maximum luminosity for models with the same configurations but with $f = 1$.

luminosity and the surface dipole field strength follows a shallower gradient than for the models with $f = 1$, as predicted. However, the difference of the maximum luminosity is less than a factor of 2 between models with $f = 1$ and models with $f = 0.7$ (for the same magnetic field configuration). This is because in the diffusion approximation, the flux that supports the accretion column vertically is from X-mode photons. Thus, the effective mixed mode opacity, calculated in the Rosseland approximation, is dominated by the X-mode opacity.

3.2.4.2 Comparison with previous models

Compared with the model from Mushtukov et al. (2015), this work uses a different method for calculating the scattering opacity and a different disc-magnetosphere

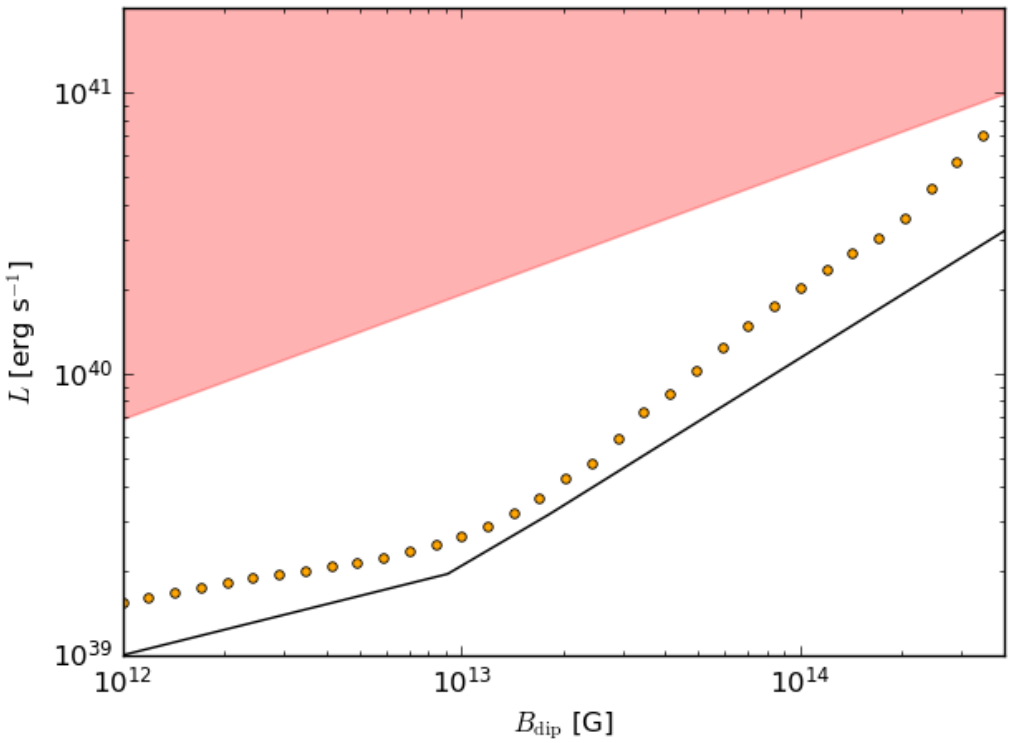

Figure 3.13: The maximum luminosity as a function of the dipole component strength at the NS surface. The orange circles show the computed maximum luminosity for a model with a pure dipole magnetic field configuration, and with $\zeta_{\rm max} \sim 1$. The black line is the maximum luminosity according to the relation given in Mushtukov et al. (2015).

interaction model. Figure 3.13 shows the maximum luminosity for models assuming the same disc-magnetosphere interaction model as in Mushtukov et al. (2015), namely by setting $\zeta_{\rm max} \sim 1$. In this case, the maximum luminosity differs only by a factor of a few, indicating a good agreement between the codes.

3.2.5 Constraints on the parameter space

Before an application of this accretion column model to diagnose observed PULXs, there are several conditions for a self-consistent physical description of a source that constrain the parameter space. First, the assumption of a geometrically thin accretion disc means that

$$H_m < R_m, \tag{3.27}$$

where H_m is the disc height at the magnetospheric radius and it depends on the assumed disc model. For a standard Shakura & Sunyaev (1973) thin accretion disc model at the accretion rates of interest in this model ($L > 10^{39}$erg s^{-1}), the inner disc is radiation-pressure dominated. Thus, the disc height is given by

$$H_m = \frac{\kappa_{\rm T}}{c}\frac{3}{8\pi}\dot{M}, \tag{3.28}$$

which is independent of the radius.

Using (3.27) and (3.28), the condition $H_m < R_m$ is equivalent to a lower bound on the dipole component strength, above which this model is valid. This condition is given by

$$B_{\rm d,12} > 0.034 L_{39}^{9/4} R_6^{-3/4} m^{-2} \Lambda^{-7/4}. \tag{3.29}$$

For magnetic configurations with a weaker dipole component, the thickness of the disc becomes large at the magnetospheric boundary, causing it to envelop the magnetosphere. In this case, the estimates used in this model for the accretion column geometry and the assumptions made on the distribution of infalling plasma are no longer applicable. A proper analysis of this scenario requires a new disc-magnetosphere interaction model, which is beyond the scope of this work.

Secondly, as PULXs are rotating NSs, the strength of the dipole component must be sufficiently small so the propeller effect is avoided. This means the magnetospheric radius must be smaller than the Keplerian corotation radius, which is given by

$$R_{\rm co} = \left(\frac{GMP^2}{4\pi^2}\right)^{1/3} \approx 1.5\times 10^8 m^{1/3} P^{2/3} {\rm cm} \tag{3.30}$$

where P is the NS spin period. The condition $R_m < R_{\rm co}$ is equivalent to an upper bound for the dipole component strength, namely

$$B_{\rm d,12} < 4.57 \Lambda^{-7/4} m^{-1/12} R_6^{-5/2} L_{39}^{1/2} P^{7/6}. \tag{3.31}$$

For models with a stronger dipole component, the propeller effect prevents accretion onto the poles Illarionov & Sunyaev (1975).

Thirdly, I assume the spin period derivative to be dominated by the accretion torque. A simple accretion torque model, where the angular momentum of the accreting matter is transferred to the NS at the corotation radius (i.e. an over-estimate of the accretion torque), gives an upper bound for the accretion luminosity, namely

$$L_{\rm acc} > 0.66 \dot{P}_{-10} P^{-7/3} 10^{39} \text{erg s}^{-1}, \tag{3.32}$$

where $\dot{P}_{-10} = 10^{-10}\dot{P}$ and P is in seconds. A lower accretion luminosity is incapable of explaining the spin period derivative.

3.2.6 Applications

Working with the parameter space restrictions derived in §3.2.5, I diagnose the necessity for higher order multipole components in observed PULXs. The model and parameter space constraints is applied to two PULXs, for which the application of the model by Mushtukov et al. (2015) has led to the suggestion of the presence of multipolar magnetic fields, namely NGC 5907 ULX1 (Israel et al., 2017a) and NGC 7793 P13 (Israel et al., 2017b). The luminosity of these sources vary by a factor of ~ 8, which is large but unlikely to be from a transition to the propeller effect, unlike in M82 X-2 (Tsygankov et al., 2016). Hence, I apply the upper bound for the dipole component strength given by equation (3.31) to the range of luminosities.

3.2.6.1 NGC 5907 ULX-1

NGC 5907 ULX-1 (Israel et al., 2017a) is the brightest PULX found to date, with a peak luminosity of $(2.3 \pm 0.3) \times 10^{41}$erg s^{-1} and an observed luminosity variation between 2.6×10^{40}erg s^{-1} to 2.3×10^{41}erg s^{-1}. Observations from *XMM-Newton* in 2003 and 2014 have shown a decrease in the pulse period from ~ 1.43s to ~ 1.137s, which corresponds to a secular spin period derivative $\dot{P} \approx -8 \times 10^{-10}$ s s^{-1}.

Israel et al. (2017a) suggested the presence of multipole components of the magnetic field when examining the source with the model by Mushtukov et al. (2015). To test this argument using the computed maximum luminosity from the

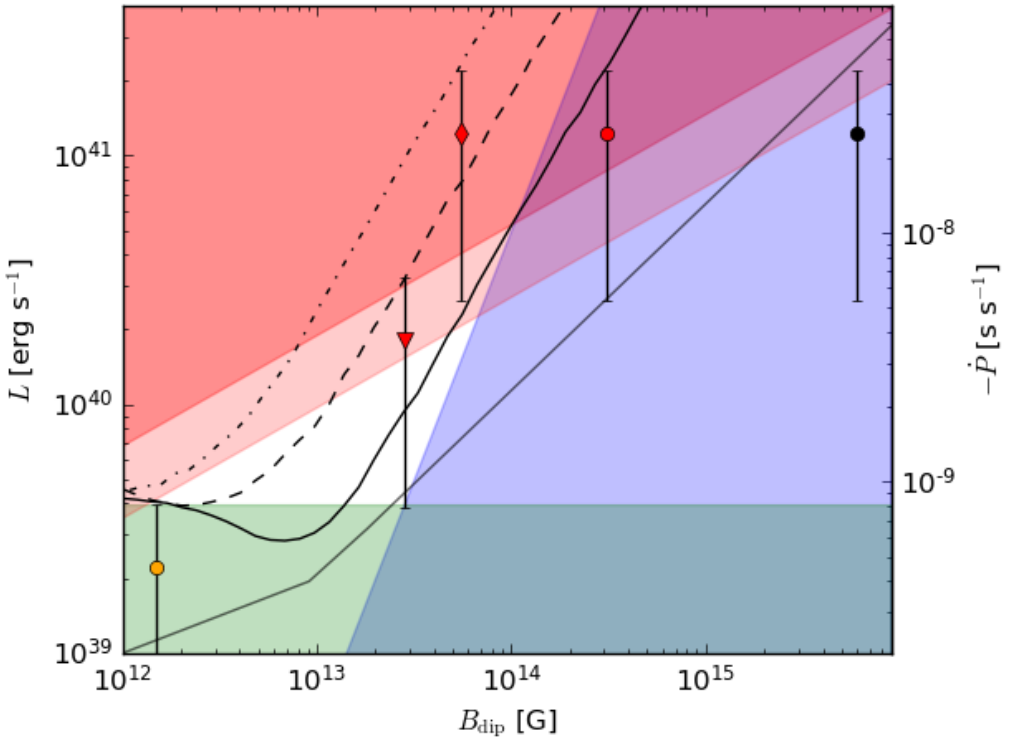

Figure 3.14: A plot of the model parameter space - accretion luminosity and dipole component strength at the NS surface - for the source NGC5907 ULX-1. Several example models (and the corresponding model parameter values) of the source are shown by the black, red, and orange shapes, where the associated vertical line represents the range of accretion luminosities from observations of the source in a high-luminosity state Israel et al. (2017a). In particular, the models shown by the red triangle and orange circle assume a luminosity amplification by a factor of ≈ 6.8 and > 50 respectively. The light red and dark red shaded areas show the region of parameter space for which the accretion luminosity exceeds the thick disc and NS Eddington luminosity respectively at the magnetospheric boundary. The blue shaded area shows the region for which the source in in the propeller regime. The green shaded area shows the region for which the accretion rate (calculated from the accretion luminosity) is too low to provide sufficient secular spin period derivative $\dot{P} = -8 \times 10^{-10}$ s s^{-1}. From right to left, the grey, solid, dashed, dot-dashed lines show the maximum luminosity relation given by the calculation done by Mushtukov et al. (2015), and models from Brice et al. (2021) with $\Gamma = 0, 3, 10$ respectively.

model of this work, a figure analogous to fig. 3 of Israel et al. (2017a) is shown. Figure 3.14 shows the parameter space constraints in the $L - B_{\rm dip}$ plane and a few example models for NGC 5907 ULX-1.

In agreement with the previous findings, in order to explain the whole range of observed luminosities up to the peak luminosity of NGC 5907 ULX-1 while

assuming a pure dipole magnetic field topology, a strong magnetic field strength is necessary, i.e. $B > 10^{14}$G from this model and $B > 10^{15}$G from the model by Mushtukov et al. (2015). Specifically, the model presented here suggests a pure dipole magnetic field with a surface strength $B_{\rm dip} \approx 3.1 \times 10^{14}$G can give rise to a luminosity of 2.3×10^{41}erg s^{-1}. Although the strength of this magnetic field is an order of magnitude lower the inferred from the model by Mushtukov et al. (2015), the source is still in the propeller regime in this case.

For the PULX to be emitting with its peak luminosity without being in the propeller regime, a multipolar magnetic field is required, in particular a dipole component strength of $B_{\rm dip} \approx 5.5 \times 10^{13}$G and octupole component surface strength of $B_{\rm oct} > 5.5 \times 10^{14}$G (see figure 3.14). However, for all observed luminosities, this configuration falls within the thick disc regime, i.e. the dipole magnetic field strength is lower than the bound given in equation (3.29). While it can not be excluded that this contradiction may be resolved once a different and less simplified disc model is adopted, to answer this question would require a thorough treatment of the disc accretion and disc-magnetosphere interaction, which is beyond the scope of this work.

Both the super-Eddington disc accretion rate and the propeller regime can be avoided by introducing a moderate beaming factor of $b \leq 0.15$. In this case, a model with a multipole mangetic field configuration consisting of a dipole component with strength $B_{\rm dip} \approx 2.8 \times 10^{13}$G and an octupole component with strength $B_{\rm oct} > 8.4 \times 10^{13}$G can explain the range of observed luminosities up to b times the peak luminosity.

Stronger beaming factors $b < 0.02$ allow for a reduced accretion luminosity and therefore make a pure dipole configuration possible again. However, in this case, the average accretion luminosity falls below the minimum set by the observed secular spin period derivative, i.e. equation (3.32). Hence, according to this model, the most favourable configuration for NGC 5907 ULX-1 includes a moderate beaming factor and a multipolar magnetic field.

3.2.6.2 NGC 7793 P13

NGC 7793 P13 was observed to have a peak luminosity of 1.6×10^{40}erg s^{-1} and an observed luminosity variation between $\sim 2.0 \times 10^{39}$erg s^{-1} and 1.6×10^{40}erg s^{-1}. A spin period of ~ 0.42s was measured and a secular spin period derivative $\dot{P} \sim -4.0 \times 10^{-11}$s s^{-1}. The constraints on the possible values of L and $B_{\rm dip}$ are shown in figure 3.15, together with some example configurations for this source.

In this case, the whole range of observed luminosities (up to the peak luminosity) can be achieved by a configuration with a multipolar magnetic field consisting of a dipole component of strength $B_{\rm dip} \approx 7.3 \times 10^{12}$G and a much stronger octupole component of strength $B_{\rm oct} > 7.3 \times 10^{13}$G (this is shown as the red triangular point in figure 3.15). Under these conditions, the source is not in the propeller regime and no beaming is required to avoid the super-Eddington disc regime. This particular configuration has the advantage of being above the lower luminosity bound required to explain the observed spin period derivative. However, the largest observed flux levels are not compatible with the assumption of a geometrically thin disc, which again may demonstrate that the disc model is overly-simplistic.

When a mild beaming factor of $b < 0.25$ is introduced, the accretion luminosity is small enough that it can be explained by a pure dipole configuration with a surface strength of $B_{\rm dip} \sim 1.4 \times 10^{12}$G. This conclusion is different to the one from the model by Mushtukov et al. (2015). The only downside is that the lowest observed luminosities fall below the bound required to explain the observed spin period derivative. On the other hand, the secular spin period derivative may be the cumulative result of alternative accretion phases and may have been accumulated during epochs of larger mass transfer. Thus, this particular configuration cannot be ruled out entirely from the simplified accretion torque model used here.

3.3 Discussion

Motivated by the recent discovery of pulsating ULXs (Bachetti et al., 2014; Fürst et al., 2016; Israel et al., 2017b,a; Carpano et al., 2018; Wilson-Hodge et al., 2018; Sathyaprakash et al., 2019; Rodríguez Castillo et al., 2020) and their interpretation

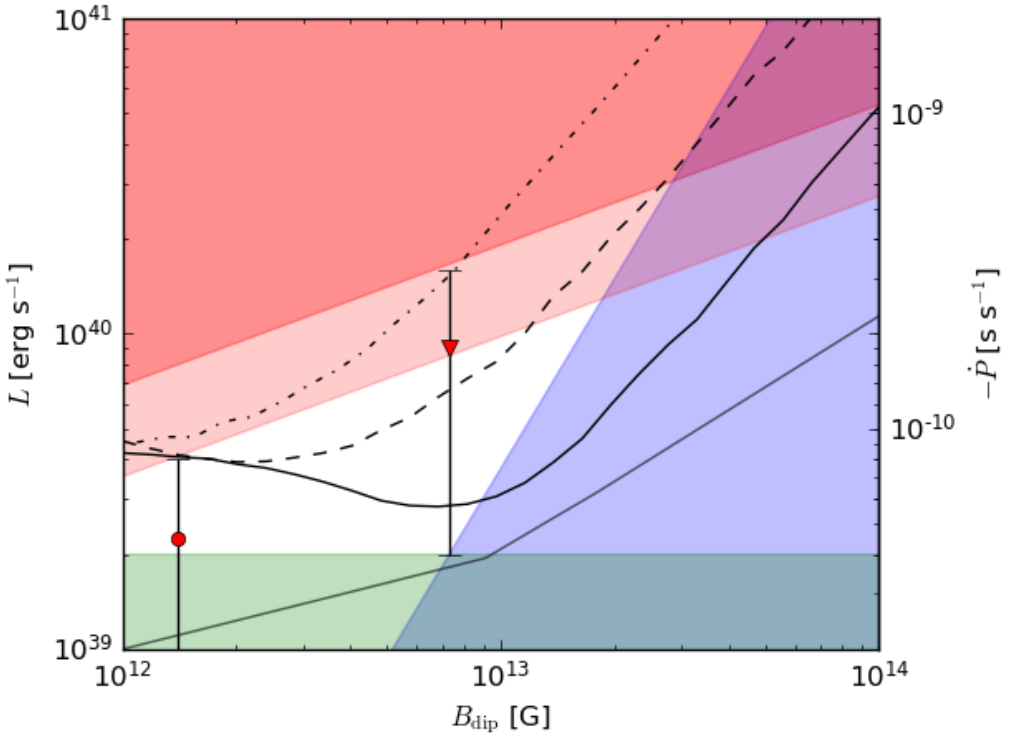

Figure 3.15: A plot of the parameter space for the source NGC7793 P13. The two example models (and corresponding model parameter values) are shown by the red triangle and red circle, where the latter assumes a luminosity amplification factor of 4. The shaded areas show the region of parameter space as in Fig. 3.14, except using $\dot{P} = -4.0 \times 10^{-11}$ s s^{-1}. The lines show the maximum luminosity relations for the magnetic field configurations as in figure 3.14.

as accreting magnetars (see Tong & Wang 2019), I have reconsidered the model of columnated accretion onto a highly magnetised NS. The main aim was to find models capable of producing a super-Eddington luminosity while avoiding the propeller regime for the spin periods typcial of PULXs, i.e. $P \sim 1$s. This was done by calculating the maximum luminosity for a given set of model parameters and taking into account other constraints of the parameter space.

The model considered in this work is similar to the one by Mushtukov et al. (2015) but with the assumption of a purely dipole magnetic field topology relaxed. In particular, the magnetic field configuration was made up of a dipole component and octupole component. I chose this topology for study because of the fall-off in the octupole component strength with distance from the surface and the polarity

alignment (unlike for a dipole plus quadrupole topology).

To investigate the possibility of super-Eddington emission, I computed a series of models, characterised by either a pure dipole magnetic field with strength of $\sim 3 \times 10^{12}$G, or a magnetic field consisting of a dipole component with a stronger ($\sim 3, 10$ larger) octupole component. First, the accretion column was assumed to be dominated by the lower opacity X-mode photons. In this case, a super-Eddington solution with luminosity 10^{39}erg s^{-1} – 10^{40}erg s^{-1} is always possible.

In models with a pure dipole topology, the accretion column height was higher than the accretion column height in models that included the stronger octupole component. As a result, the effective temperature of the accretion column, $T_{\rm eff}$, is larger. Typically, $T_{\rm eff} \approx 3 - 15$keV, with the peak temperature higher in the accretion column. This thermal emission is not observed directly because of reprocessing from the optically thick free-falling material surrounding the sinking region. Further reprocessing from an optically thick envelope surrounding the magnetosphere is possible (see the next chapter and Mushtukov et al. 2017).

I investigated the impact of the polarization degree on the other accretion column properties by substituting a fixed fraction of X-mode photons to O-mode photons, which changes the effective mean opacity. Although the accretion properties changed as a result, there was no significant variation in the maximum luminosity.

In general, the opacity local to the NS surface was a decisive factor for the possibility of NS super-Eddington emission ($L > 10^{39}$erg s^{-1}), as observed in ULXs. However, the geometry of the accretion column footprint on the NS surface is an additional factor in determining the accretion column properties, which had not been investigated until this work. In particular, the thickness of the accretion column has a significant effect on the luminosity. The greater maximum luminosity for a given magnetic field strength that was calculated in this work compared with that by Mushtukov et al. (2015) was partly due to the different approach to calculating the accretion column thickness.

In principle, solutions for models with a luminosity $L \sim 10^{41}$erg s^{-1} are obtainable. However, in order to avoid the propeller regime for a source with pulse

period of the order $\sim$ 1s, the dipole component strength must be sufficiently low ($\sim 10^{13}$G). A low dipole component strength together with high accretion luminosity results in a geometrically thick accretion disc, as already noted by Israel et al. (2017a). In this scenario, the model is no longer valid. Consequently, there is still an upper limit to the luminosity related to the dipole component strength.

The restriction to a thin accretion disc comes from the use of the Ghosh & Lamb (1978) disc-magnetosphere interaction model, specifically to obtain estimates for the truncation radius of the disc and the boundary region width, i.e. the disc penetration into the magnetosphere. Ideally, a disc-magnetosphere interaction model more suitable for super-Eddington accretion would be used, e.g. by Chashkina et al. (2017), but this was beyond the scope of this work. Instead, to address some of these limitations, I investigated the extent to which this disc-magnetosphere interaction model affects the accretion column properties (and more generally the existance of a solution given a set of model parameters). I found an accurate value of the truncation radius is largely irrelevant, whereas the boundary region width is crucial. In particular, a variation of 30 percent in the boundary region width decreases the accretion column base size by an order of magnitude.

Another limitation in this model is in the treatment of the hydrodynamics equations. The curvature of the magnetic field lines that constrain the accretion flow. In principle, it is possible to account for the curvature in the equations of hydrodynamics, e.g. as in Canalle et al. (2005) and Adams & Gregory (2012).

This model was applied to the two sources NGC 5907 ULX-1 and NGC 7793 P13 (see §3.2.6). The necessity for a multipolar configuration is different in each case, once beaming is taken into account.

For NGC 7793 P13, the observed luminosity is $\approx 1.6 \times 10^{40}$erg s^{-1}. When taken at face value, this luminosity is too large to be compatible with the model by Mushtukov et al. (2015) since it requires a magnetic field strength so high that the source would be deep in the propeller regime. On the other hand, according to the model in this work, the lowest observed luminosity is compatible with a pure dipole magnetic field configuration, where the dipole component strength is

$B_{\rm dip} \approx 7.3 \times 10^{12}$G. The addition of a stronger octupole component with surface strength $B_{\rm oct} > 7.3 \times 10^{13}$G explains the whole range of observed luminosities, even up to the peak luminosity of 1.6×10^{40}erg s^{-1}.

The multipolar configuration does not conflict with the propeller effect, nor with the super-Eddington accretion rate condition. Furthermore, it is compatible with the simple treatment of the spin period derivative (see §3.2.5). However, the observed peak luminosity is not compatible with the geometrically thin disc assumption (which gives further credence that the disc model is over-simplified).

Other possibilities include moderate beaming, in which case the observed luminosity is reachable for the case of a pure dipole magnetic field with strength $B_{\rm dip} \approx 1.4 \times 10^{12}$G. However, this case is unlikely when considering the observed spin period derivative because the average mass accretion rate is barely above the minimum accretion luminosity of the overly-simplified estimate (which gives an unrealistic lower bound).

The PULX NGC 5907 ULX-1 has a much higher peak luminosity of 2.3×10^{41}erg s^{-1}. In this case, both a super-Eddington disc accretion regime and the propeller regime can be avoided by invoking a moderate beaming factor of $b < 0.15$. If the source has a magnetic field configuration consisting of a dipole component with strength $B_{\rm dip} \approx 3.2 \times 10^{13}$G and a stronger octupole component strength $B_{\rm oct} > 9.6 \times 10^{13}$G, the entire range of observed luminosities is under the maximum. A pure dipole configuration is only possible with a stronger beaming factor $b < 0.02$. However, this case is ruled out by the minimum luminosity of the overly-simplified estimate.

There remains open questions that need to be addressed before arriving at a self-consistent explanation of PULXs. As mentioned previously, the presence of multipole magnetic field components can change the properties of the accretion column significantly. The maximum shock height, H, is reduced in comparison to case of a pure dipole magnetic field topology. This in turn results in a higher effective temperature, which may manifest in the spectral data. In principle, a sufficiently strong magnetic field would lower the shock height close to the surface

so that $H \ll R$. However, since this model assumes the radiation pressure pimarily perpendicular to the sinking region, its validity becomes dubious as $H \to 0$. In addition, as the maximum shock height of the column is lowered, the temperature of the sinking region may exceed 100keV, whereupon the electron-positron pair creation and annihilation play an increasingly important role in limiting the temperature of the accretion column while simultaneously increasing the gas pressure (Mushtukov et al., 2019). A calculation of the gas pressure as well as the pair creation and annihilation process is necessary for a more accurate description. This has started to be addressed by Suleimanov et al. (2022).

Several other simplifying assumptions were made in the model presented in this work. First, the radiation pressure dominates over the gas pressure of the sinking region of the accretion column. From computing several models, I found that the assumption breaks down at the lower layers of the sinking region. Because a power-law ansatz was used for the velocity profile, the model is not expected to give an accurate picture in the lower layers of the sinking region, where the accretion flow becomes stagnant and hence the density becomes infinite. However, the contribution to the luminosity from these lower layers is negligible compared with higher in the column, where the radiation pressure remains dominant.

Secondly, the calculation of the scattering opacity in this work neglected the contribution from the ions and vacuum polarization effects, which are both expected to become significant exactly in the strong magnetic field regime considered here ($B > 10^{13}$G). Additionally, a fixed fraction of X-mode photons made up the radiation field throughout the accretion column. A more physically realistic calculation would include the scattering between polarization modes as well as including mode switching from resonant scattering. This is left as future work.

Finally, the role of energy advection was not taken into account, nor cooling via neutrino emission. These processes were studied in Mushtukov et al. (2018) and are expected to be relevant in the case of very luminous sources $L \sim 10^{41}$erg s^{-1}. In §3.2.6, a beaming factor was assumed instead.

3.4 Summary

I developed a simplified model of the accretion column for strongly magnetised NSs, building on and altering the model by Mushtukov et al. (2015). Crucially, the assumption of a purely dipole mangetic field is relaxed. This allows for a larger maximum luminosity.

When a magnetic field configurations with a significantly strong multipole component is assumed, the luminosity released in the accretion column is limited only by the accretion rate from the disc. This, in turn, calls for a more refined model of the disc accretion and disc-magnetosphere interaction for super-Eddington accretion, e.g. as investigated by Chashkina et al. (2017, 2019).

I applied the model to two PULXs, NGC 5907 ULX-1 and NGC 7793 P13, and discussed how their observed properties (e.g. luminosity and spin period derivative) can be explained in terms of different magnetic field configurations, either with or without multipolar components. For both sources, the case with a multipolar component is favoured. Although it may be difficult to differentiate further, the strong multipole components may manifest in the spectra or polarization signal, an issue that is left for investigation in a future work.

Chapter 4

Pulsed Fraction

The work presented in this chapter was also published in Brice et al. (2023).

The observed sinusoidal pulses from PULXs identifies their central engine as a NS. These pulsations was first discovered in M82 X-2 (Bachetti et al., 2014) and subsequently observed in the PULXs NGC 7793 P13 (Fürst et al., 2016; Israel et al., 2017b) and NGC 5907 ULX-1 (Israel et al., 2017a). The observed pulse profile of these sources remains sinusoidal throughout the whole energy range, but the pulsed fraction increases with increasing energy, e.g. from $\sim 12\%$ for < 2.5keV to $\sim 20\%$ for > 7keV for NGC 5907 ULX-1 (Israel et al., 2017a).

Mushtukov et al. (2021) showed that pulsed fractions $> 20\%$ make the interpretation of PULXs as strongly beamed X-ray sources via optically thick outflows unlikely. However, no similar quantitative study has been done for the pulsed fraction in the super-Eddington accretion rate scenario.

Mushtukov et al. (2017) investigated some of the observational implications of the super-Eddington accretion scenario otherwise, in particular focusing on the absence of cyclotron resonance features (CRFs) in PULXs with super-strong magnetic fields. The authors found that an optically thick envelope around a NS forms when there is a sufficiently large ($> 10^{19}\mathrm{gs}^{-1}$) mass accretion rate, resulting in a reprocessing of the accretion column emission. Hence the disappearance of CRFs. Moreover, this reprocessed emission is thermal due to multiple scatterings as the radiation travels through the optically thick envelope walls, and appears as a multicolour blackbody to an observer. Koliopanos et al. (2017) tested these predictions

by fitting the spectra of ULXs (and some PULXs) to a dual thermal emission component model, which was found to be in good agreement.

In this work, I study the observational properties of the radiation emitted by an optically thick envelope in more detail. The main aim is to calculate the pulse profile using an approximation of the physics and compare it with observations.

4.1 Envelope Model

In the standard picture of accretion onto a highly magnetised NS, the accretion disc is assumed to be truncated at the magnetospheric radius, given by

$$R_m \approx 7 \times 10^7 \Lambda M^{1/7} R_6^{10/7} B_{\mathrm{d},12}^{4/7} L_{39}^{-2/7} \mathrm{cm}, \tag{4.1}$$

where Λ is a dimensionless parameter that depends on the mode of accretion (typically $\Lambda = 0.5$ for accretion via thin disc), $B_{\mathrm{d},12}$ is the surface dipole field strength at the magnetic poles in units of 10^{12}G, and L_{39} is the accretion luminosity in units of 10^{39}erg s^{-1}. In addition, the disc penetrates into the magnetosphere by some length, here indicated as P_m. However, the exact physical process and hence an expression for P_m is poorly known. In this model, the expression for P_m is extrapolated from the thin accretion disc model to the scenario with a thick disc as

$$P_m \approx H_m, \tag{4.2}$$

where H_m is the height of the disc at the magnetospheric radius. An upper limit is imposed so that $P_m/H_m < 0.2$.

For simplicity, the boundary region is assumed to be bounded by dipole magnetic field lines that extend to a maximum radius of R_m and P_m. Inside the boundary region, the accreting material is channelled onto the NS surface, which is shown by the diagram in figure 4.1.

If the accretion rate is $> 10^{19}$gs^{-1}, the accreting material forms an optically thick envelope, which encloses the magnetosphere cavity (filled with only radiation). As the envelope is optically thick, the radiation injected into the inner cavity

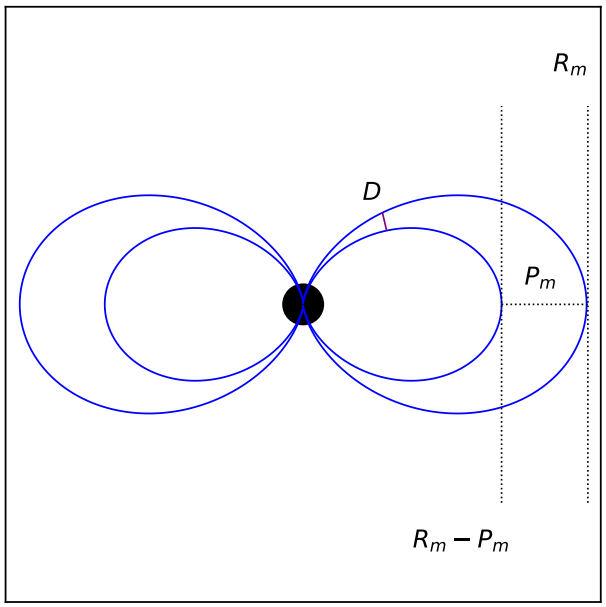

Figure 4.1: A diagram of the bounding dipole magnetic field lines (solid blue curves), reaching out to a radii R_m and $R_m - P_m$. The purple line shows the path of radiation diffusion in the envelope. It is annotated by the path length D. The centre black circle represents the NS.

cannot immediately escape and hence thermalises. The spectrum is given by the Planck function at temperature $T_{\rm in}$ (Mushtukov et al., 2017).

The spectrum of the thermal radiation that emerges from the envelope, and is observed at infinity, depends on the temperature of its outer boundary, $T_{\rm in}$, which at first approximation is related to $T_{\rm out}$ and to the local optical depth of the envelope, τ, by

$$T_{\rm in} = T_{\rm out}\tau^{-1/4}. \tag{4.3}$$

As the local optical depth is determined by the dynamics of the accretion flow, and the velocity field is not necessarily uniform inside the envelope, $T_{\rm out}$ varies along the envelope wall as well. Thus, the spectrum of the escaping radiation is expected to be approximately a multicolour blackbody, rather than a Planckian at a single temperature.

The relationship between the cavity temperature, $T_{\rm in}$, and the luminosity is obtained after integrating the local flux $\sigma T_{\rm out}^4$ (where σ is the Stefan-Boltzmann

constant), over the surface of the envelope. Using equation (4.3), this gives

$$L_{\rm acc}/2 = 2\sigma T_{\rm in}^4 \int_{\varphi=0}^{\varphi=2\pi} \int_{\theta=\pi/2}^{\theta_f} \tau^{-1} {\rm d}A, \tag{4.4}$$

where $L_{\rm acc}$ is the accretion luminosity, ${\rm d}A = {\rm d}A(\varphi,\theta)$ is the area element of the envelope in spherical coordinates (with the zenith aligned in the direction of the magnetic moment), and θ_f is the latitute at which the same mangetic field line terminates at the surface of the NS. In equation (4.4), only half of the accretion luminosity is accounted for because the geometry of the accretion column results in half of the emission first entering the cavity and thermalising before escaping, whereas the other half of the emission directly escapes through the exterior envelope wall, i.e. does not contribute to the cavity temperature. The photons that directly escape through the exterior envelope wall may be reprocessed from multiple scatterings, which would result in spectral changes.

4.1.1 Local optical depth

In order to estimate the optical depth of the envelope, the path length of radiation diffusion through the envelope wall is needed. The path length of escape is denoted by D and its direction is assumed to be normal to the envelope surface. Hence, the local optical depth is approximated by

$$\tau = \kappa_e \rho D, \tag{4.5}$$

where κ_e is the electron scattering opacity, and ρ is the local electron density along D (which is approximated as constant).

The local density is given by

$$\rho = \frac{\dot{M}}{v_{\parallel}} \frac{1}{A_c}, \tag{4.6}$$

where $\dot{M}$ is the total mass accretion rate onto the NS, $v_{\parallel}$ is the velocity of the charges along the field lines (which is assumed to be constant along the photon escape path), and A_c is the cross-sectional surface area perpendicular to the magnetic field lines,

i.e. perpendicular to the velocity direction for the charges. In this case, the mass transfer rate to each hemisphere is assumed to be equally distributed for all magnetic field lines, which may not be the case in general.

Finally, A_c is calculated from the geometry of the envelope cross-section, and for a purely dipole magnetic field topology is given by

$$A_c = 2\pi \left(R_m - \frac{1}{2} P_m \right) \mu^3 D, \tag{4.7}$$

where θ is the magnetic latitude and $\mu = \cos\theta$. The calculation is laid out explicitly in appendix 4.4.1.

4.1.2 Dynamics

To obtain an expression for $v_{\parallel}$, the dynamics of a charge moving along a dipole field line of a NS, which rotates around a spin axis with angular velocity Ω, need to be studied. The NS magnetic moment is misaligned from the spin-axis by an angle ξ. In the following, an orthonormal coordinate system in which the z-axis is aligned with the magnetic moment is used. This coordinate system is referred to as the magnetic reference frame.

The radial coordinate of the dipole field lines, in spherical polar coordinates, is given by

$$r(\theta, \varphi) = R \cos^2\theta, \tag{4.8}$$

where θ and φ are the latitude and the azimuthal angle in the magnetic axis reference frame, and R is the maximal distance that the field line reaches from the source. In this model, $R = R_m - 1/2 P_m$ is used for all φ (e.g. see appendix 4.4.1).

The charge moves under the influence of gravitational and centrifugal forces. The gravitational force contributes a potential field

$$V_{\text{grav}}(r) = \frac{R^3 \Omega_K^2}{r}, \tag{4.9}$$

where $\Omega_K = (GM/R^3)^{1/2}$ is the Keplerian angular velocity at a distance R from the

point mass. The centrifugal force is taken into account by introducing a constraint to the Lagrangian:

$$V_{\rm ang}(r,\theta,\varphi) = d^2\Omega^2, \tag{4.10}$$

where $d = d(r,\theta,\varphi)$ is the distance of the moving charge from the spin-axis (see appendix 4.4.2 for a derivation of the full expression). Hence, the total Lagrangian of a charge with mass m moving on the dipole field line given by equation (4.8), under the influence of gravitational and centrifugal forces is

$$\mathscr{L} = \frac{1}{2}mR^2\dot{\theta}^2\left[4\mu^2 - 3\mu^4\right] - \frac{1}{2}md^2\Omega^2 + m\frac{1}{\mu^2}R^2\Omega_K^2. \tag{4.11}$$

The parallel velocity of the charge is defined as

$$v_\parallel = R\dot{\theta}\left[4\mu^2 - 3\mu^4\right]^{1/2}, \tag{4.12}$$

and thus the effective potential is given by

$$V_{\rm eff} = -\frac{1}{2}d^2\Omega^2 + \frac{1}{\mu^2}R^2\Omega_K^2. \tag{4.13}$$

As the effective potential includes the gravitational and rotational potentials, the NS spin effects the velocity along the field lines. Furthermore, the effective potential is conservative and thus the Euler-Lagrange equations can be integrated to obtain an analytic expression for the parallel velocity, which is given by

$$v_\parallel(\mu,\varphi) = \left[\left(d^2 - d_0^2\right)\Omega^2 + \left(\frac{2}{\mu^2} - \frac{2}{\mu_0^2}\right)R^2\Omega_K^2 + v_0^2\right]^{1/2}, \tag{4.14}$$

where $\mu_0 = \cos\theta_0$ is the cosine of the initial latitude angle of the charge, d_0 is the distance of the charge from the spin-axis at $\theta = \theta_0$, and v_0 is the initial velocity of the charge. The derivation of the initial angle expression for a geometrically thin disc is given in appendix 4.4.3.

Following Mushtukov et al. (2017), the initial velocity of the charge at any disc

height is approximated by the characteristic thermal velocity of the protons at the inner disc radius (for a geometrically thin disc). This gives

$$v_0 \approx 0.056 \left(\frac{1-\gamma}{1+X}\right)^{1/2} \Lambda^{-1/2} m^{3/7} L_{39}^{1/7} B_{\mathrm{d},12}^{-2/7} \left|1 - \frac{\Omega}{\Omega_K}\right| c, \tag{4.15}$$

where c is the speed of light, γ is the adiabatic index, and X is the hydrogen mass fraction of the accreting material.

4.1.3 Calculation of the pulsed fraction

Once T_{in} and τ are known, T_{out} can be calculated for every point p on the outer boundary of the envelope using equation (4.3). For each p, the specific flux along a particular line of sight (LOS) is given by

$$F_{E,p}(\ell) = (\mathbf{n}_p \cdot \ell)\, B_E(T_{\mathrm{out}}(p)) \Delta A_p, \tag{4.16}$$

where $\mathbf{n}_p$ is the normal to the surface of the envelope at p, ℓ is the LOS unit directional vector, $B_E(T)$ is the Planck function at temperature T, and ΔA_p is the area element of the envelope surface at p. The value of $\mathbf{n}_p \cdot \ell$ changes according to the NS phase of rotation, denoted by ϕ.

The total specific flux along a particular LOS, F_E, is obtained by summing over all the points on the surface of the envelope that are in view, i.e.

$$F_E = \sum_{p \text{ inview}} F_{E,p}(\ell). \tag{4.17}$$

In particular, and depending on the viewing geometry, the points of the envelope can be obscured by other parts of the envelope and/or by the accretion disc. Hence, the points in view are dependent on ϕ and thus $F_E = F_E(\phi)$.

To obtain the flux over an energy interval, Δ_E, the specific flux is integrated in energy to give

$$F_{\Delta_E} = \int_{E \in \Delta_E} F_E \mathrm{d}E. \tag{4.18}$$

The total flux from the NS includes a contribution from the disc emission. This is accounted for in a similar way to equation (4.16), where the disc temperature and disc angular area element at a point is used instead of $T_{\rm out}$ and ΔA_p respectively. For this model, the standard multi-colour disc temperature profile (of a thin disc) is used (Makishima et al., 1986), which is given by

$$T(r) = \left[3GM\dot{M}/8\pi\sigma r^3\right]^{1/4}. \tag{4.19}$$

For simplicity, the disc points from the inner disc radius at R_m to infinity are considered.

Finally, the pulsed fraction for the energy interval Δ_E is calculated using the definition

$$\mathrm{PF} = \frac{F_{\Delta_E,\max} - F_{\Delta_E,\min}}{F_{\Delta_E,\max} + F_{\Delta_E,\min}} \tag{4.20}$$

where $F_{\Delta_E,\max} = \max_\phi F_{\Delta_E}$ and $F_{\Delta_E,\min} = \min_\phi F_{\Delta_E}$ denote the maximum and minimum values of F_{Δ_E} during a NS rotation period.

4.2 Numerical Results

The model in this work uses the standard Shakura & Sunyaev (1973) thin accretion disc that is perpendicular to the spin axis. The accreting material subsequently flows through the envelope as described in §4.1.

For each particular LOS, the phase-dependent spectrum and pulsed fraction is calculated by ray-tracing the thermally emitting points on the envelope and the accretion disc to an observer at infinity.

To this end, this work re-adapts the numerical ray-tracing code described in Taverna & Turolla (2017), which was developed to calculate the spectra of mangetar bursts originating from a magnetically trapped fireball. The code was modified to allow for magnetic field lines reaching several hundred NS radii and a planar disc geometry was added. The code takes into account the visibility of the envelope and disc surface points by checking for (self-)shadowing by envelope and disc.

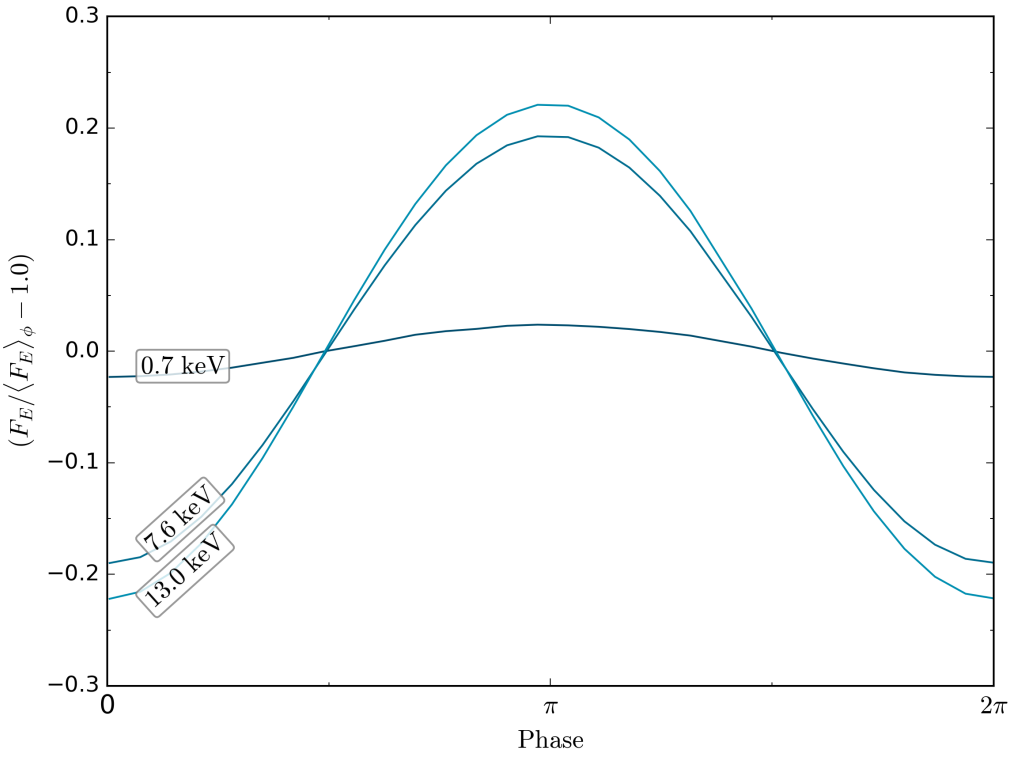

Figure 4.2: The normalised specific flux in phase. The phase-resolved specific flux is normalised with the phase-averaged specific flux, $\langle F_E \rangle_\phi$. The pulsed profile was taken from the phase-resolved synthetic spectrum of a model with $L_{39} = 10$, $B_{12} = 0.55$, $P = 0.4$ s, $\xi = 10°$, $i = 45°$.

I considered a set of models, each one being characterised by the following parameters: the accretion luminosity in units of 10^{39}erg s^{-1}, L_{39}, the (surface dipole) magnetic field strength at the pole in units of 10^{12}G, B_{12}, the tilt of the dipole magnetic moment with respect to the spin axis, ξ, the observer LOS angle (i.e. the inclination) with respect to the spin-axis of the NS, i, and the spin period of the NS, P.

The synthetic spectrum in the $0.1 - 20$keV energy range is calculated for 60 grid-points in phase. For every model, the phase-resolved synthetic spectrum varies sinusoidally in each energy interval. An example of the energy resolved profile, corresponding to a model for NGC 7793 P13 considered in §4.2.2, is shown in figure 4.2. I analysed the phase-averaged synthetic spectrum by using the IDL routine MPCURVEFIT to fit to a multi-colour disc plus blackbody model (mcd + bb). In each case, a statistically good fit was found.

In the following, the characteristic temperatures of the components from a best-fit spectral model are indicated by $T_{\rm mcd}$ for the mcd component and $T_{\rm bb}$ for the bb component, which I refer to collectively as the best-fit component temperatures. In addition, I calculated the maximum temperature on the envelope wall, $T_{\rm max}$, which I refer to as the envelope temperature, and the inner disc temperature, $T_{\rm disc}$, as diagnostic measures that are independent of the ray-tracer and spectral fitting.

Figures 4.3 and 4.4 show the results of varying the luminosity and dipole magnetic field strength on the envelope temperature and inner disc temperature alongside the best-fit component temperatures for the same models. These plots confirm that the best-fit component temperatures in the mcd+bb spectral fit (of the phase-averaged spectra), $T_{\rm mcd}$ and $T_{\rm bb}$, accurately track the underlying model variables $T_{\rm disc}$ and $T_{\rm max}$. Otherwise, the changes in ξ, i, and P did not significantly alter the best-fit component temperatures nor the underlying model variables.

Figures 4.5, 4.6, 4.7, and 4.8 show the results of varying the luminosity, dipole magnetic field strength, ξ, and i respectively on the pulsed fraction profile in energy. Otherwise, there was no change to the pulsed fraction when P was varied within its valid range for the model. All the models shared a common characteristic in their pulsed fraction profile with energy, namely a change in the gradient of the pulsed fraction profile, which I refer to as a "break" in the pulsed fraction profile.

Below, I discuss the response on the synthetic spectrum and pulsed fraction profile when varying each of the model parameters in turn. I describe how each parameter relates to the underlying model variables as a result of the choices made in the modelling.

In the first case, the reason that a variation in the accretion luminosity parameter leads to a change in the underlying model variables can be understood from equations (4.19) and (4.4). Namely, the inner disc temperature depends directly on the accretion rate in equation (4.19) and the envelope temperature is determined by the cavity temperature and minimum optical depth, both of which are related to the accretion luminosity and accretion rate in equations (4.4) and (4.6) respectively.

The synthetic spectra show that the best-fit temperature trends are aligned with

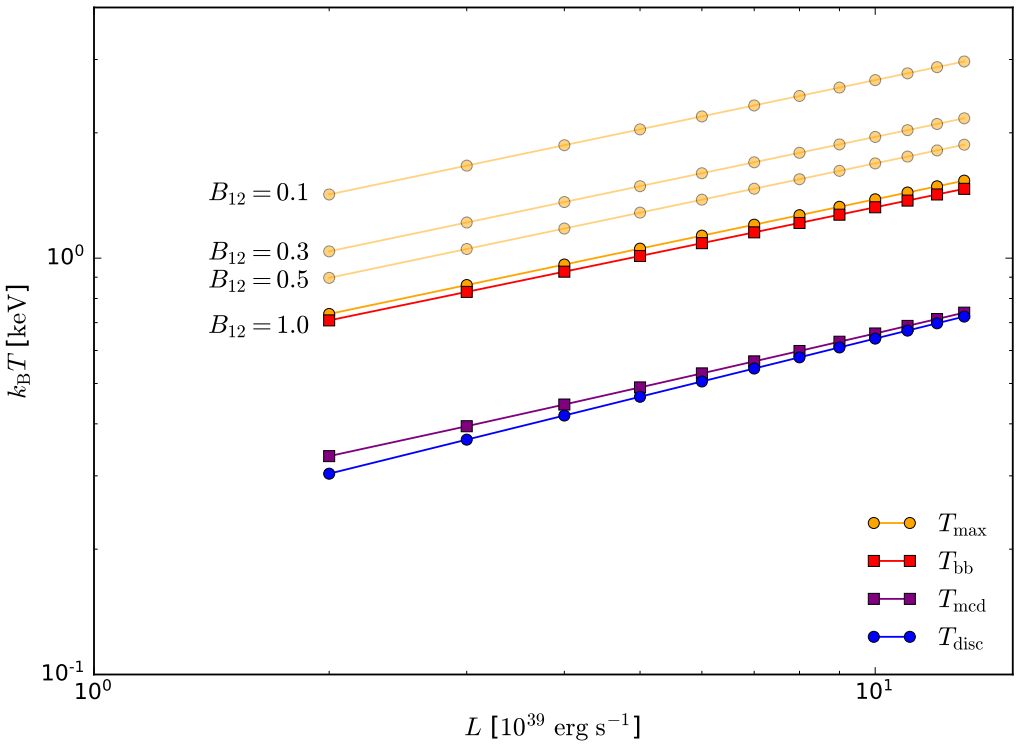

Figure 4.3: Inner disc temperature and envelope temperature, $T_{\rm disc}$ and $T_{\rm max}$ respectively, and the characteristic temperatures from the best-fit mcd+bb spectral model, $T_{\rm mcd}$ and $T_{\rm bb}$ respectively, as a function of the accretion luminosity. The other model parameters were fixed to $B_{12} = 1.0$, $\xi = 10^\circ$, $P = 1$s, and $i = 30^\circ$. In addition, $T_{\rm max}$ is shown for models with various magnetic field strengths for comparison.

the underlying model variable trends. In the primary cases shown in figure 4.3 where the model parameters were fixed to $B_{12} = 1.0$, $\xi = 10^\circ$, $i = 30^\circ$, $P = 1$s, the increase in the mcd characteristic temperature is more rapid than the increase in the bb characteristic temperature. A simple linear regression model for the logarithmic luminosity and temperature values gives the relationship between the mcd temperature and accretion luminosity as $T_{\rm mcd} \propto L_{39}^{0.44}$ whereas the bb temperature is related to the accretion luminosity as $T_{\rm bb} \propto L_{39}^{0.39}$. This trend, where the power law index is steeper for the component associated with the disc, is reflected in the relationship of the accretion luminosity with the underlying model variables, i.e. $T_{\rm disc} \propto L_{39}^{0.46}$ and $T_{\rm max} \propto L_{39}^{0.39}$. In addition, the power law index for the inner disc temperature and envelope temperature were consistent for the alternate magnetic field strengths

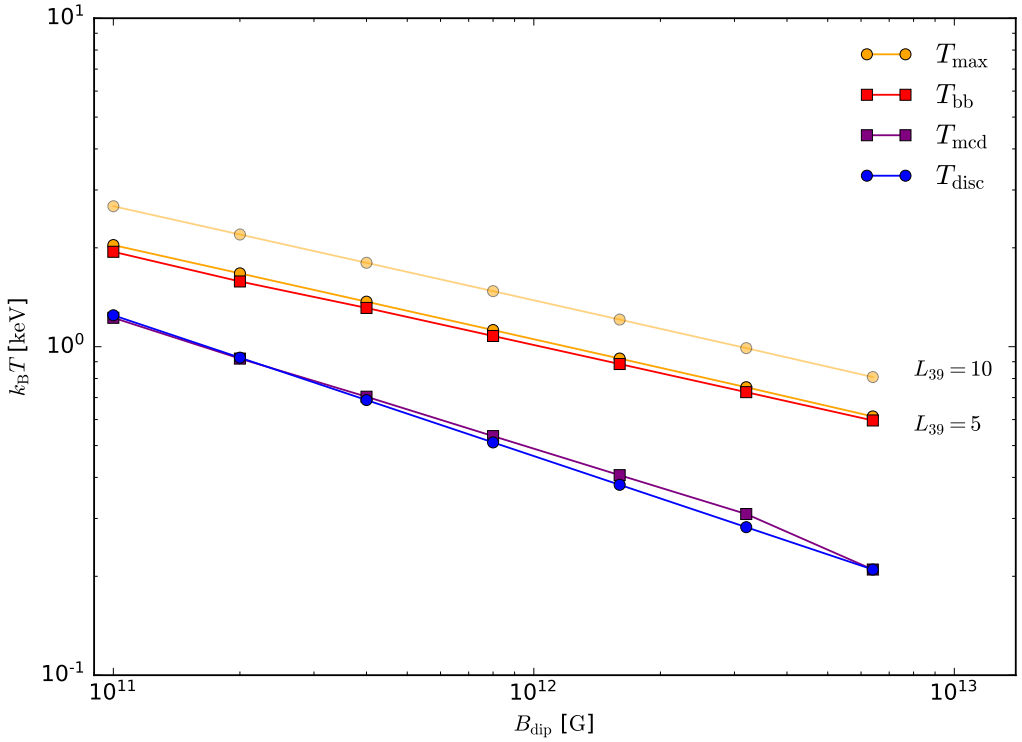

Figure 4.4: Same quantities as in figure 4.3, here shown as a function of the (dipole) magnetic field strength, B_{dip}. The other model parameters were fixed to $L_{39} = 5$, $\xi = 10°$, $P = 1$s, and $i = 30°$. Another line of T_{max} for models with $L_{39} = 10$ is shown for comparison.

shown in figure 4.3.

Since a variation of the accretion luminosity changes the synthetic spectrum, the energy-dependent pulsed fraction is subsequently affected. In particular, models with a higher accretion luminosity (with all other parameters held constant) exhibit a lower pulsed fraction in all energy intervals, as shown in figure 4.5. In addition, the break from steep increase in pulsed fraction with energy occurs at a higher energy for models with higher accretion luminosity.

The fact that the pulsed fraction is lower for all energy intervals, including for energies after the break, can be attributed to the specifics of the temperature distribution on the envelope. Namely, the highest temperatures lie in a small region close to where the disc meets the magnetosphere, which means the pulsed fraction at high energies is representative of the change in effective area, i.e. the projected area onto a plane perpendicular to the observer's LOS, of these high temperature regions

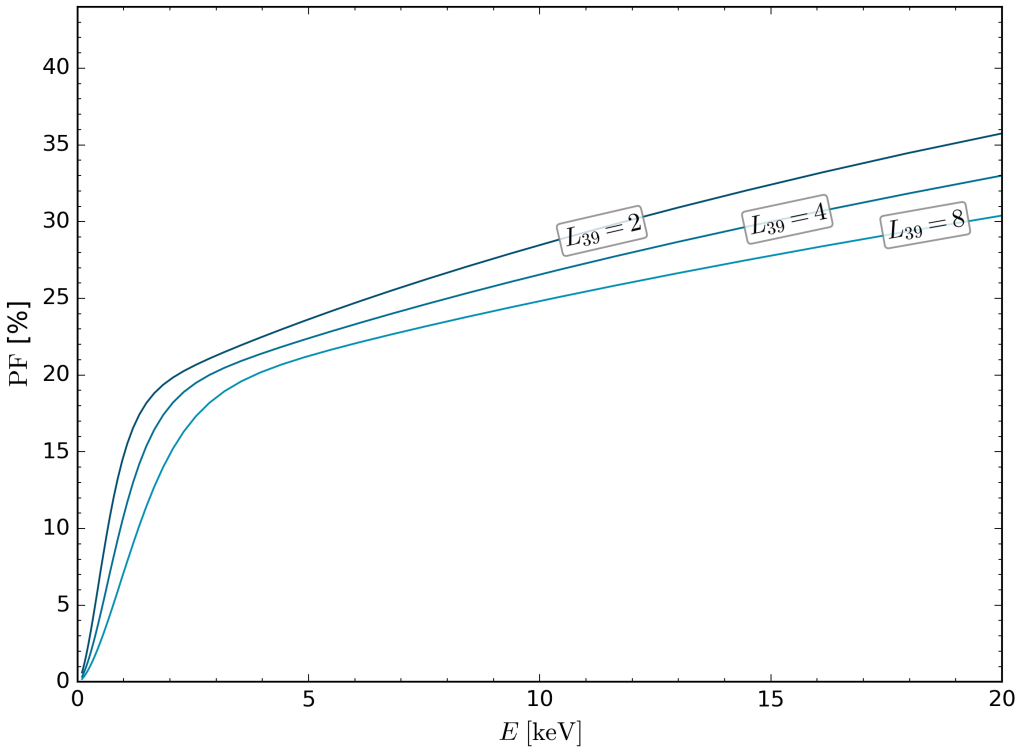

Figure 4.5: The pulsed fraction as a function of energy for models with various accretion luminosities, labelled with each line. The other model parameters were fixed to $B_{12} = 1.0$, $\xi = 10°$, $P = 1$s, and $i = 30°$.

during one full rotation of the system. For increased accretion luminosity, the higher temperature regions make up a larger proportion of the total envelope area, and hence there is a smaller change to the effective area during one full rotation.

The fact that the pulsed fraction break occurs at higher energy can be attributed to a hotter inner disc due to an increased accretion luminosity (and simultaneously smaller magnetospheric radius). It is the temperature of the hottest regions of the disc that determines at what energy the disc flux peaks, after which the envelope emission (with the higher characteristic temperature) dominates.

A change in the dipole magnetic field strength parameter leads to a change in the underlying model variables, which (similarly to the analysis of the accretion luminosity parameter) can be understood from the equations of the envelope model outlined in §4.1. In this case, the inner disc temperature and envelope temperature both depend inversely on the magnetospheric radius, which in turn depends directly

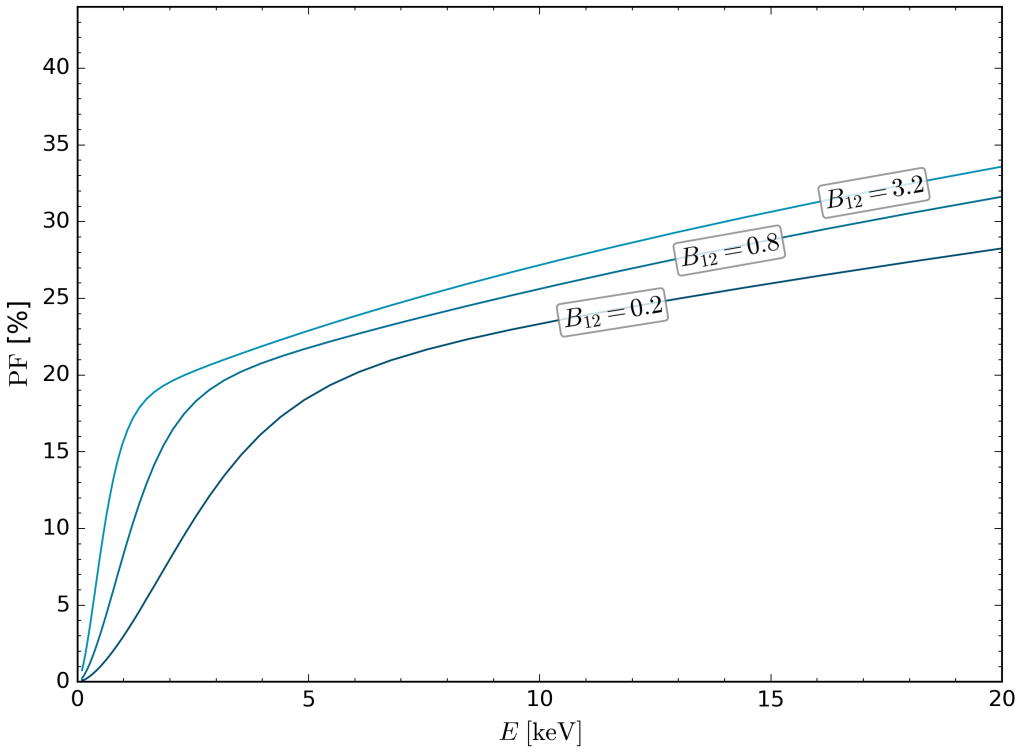

Figure 4.6: The pulsed fraction as a function of energy for models with different values of the magnetic field strength parameter, shown with each line. The other model parameters were fixed to $L_{39} = 5$, $\xi = 10^\circ$, $P = 1$s and $i = 30^\circ$.

on the magnetic field strength, given in equation (2.16).

The best-fit temperatures from the synthetic spectra again show aligned trends to the underlying model variables, with an increase in the dipole magnetic field strength resulting in a decrease of the best-fit component temperatures. For the models shown in figure 4.4, the model parameters were fixed to $L_{39} = 5$, $\xi = 10^\circ$, $P = 1$s, $i = 30^\circ$, and varied the magnetic field strength parameter between $B_{12} = 0.1$ to 3.2. A linear regression model on the logarithmic B_d and temperature values gives the relation between best-fit component temperatures and the dipole field strength parameter as $T_\mathrm{mcd} \propto B_{\mathrm{d},12}^{-0.42}$ and $T_\mathrm{bb} \propto B_{\mathrm{d},12}^{-0.28}$. This aligns with the relations between the underlying model variables and the dipole field strength parameter, where $T_\mathrm{disc} \propto B_{\mathrm{d},12}^{-0.43}$ and $T_\mathrm{max} \propto B_{\mathrm{d},12}^{-0.29}$.

Similarly to the case of increasing accretion luminosity, the changes to the synthetic spectra from an increase in the magnetic field strength results in changes

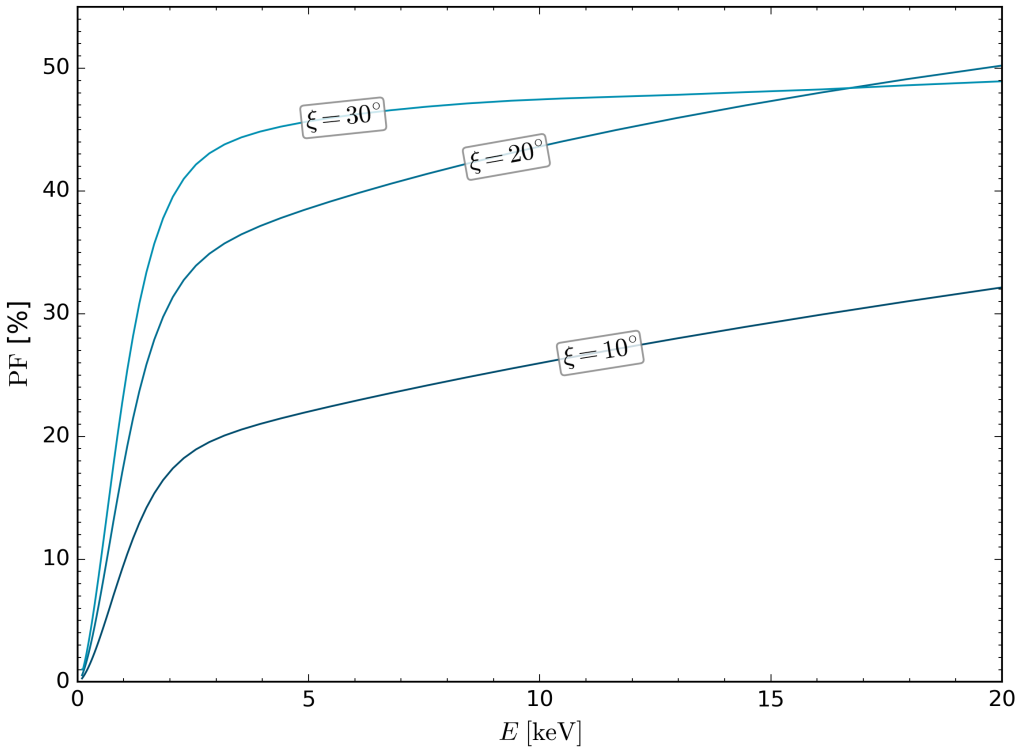

Figure 4.7: The pulsed fraction as a function of energy for models with different values for the magnetic axis tilt, shown with each line. The other model parameters were fixed to $L_{39} = 5$, $B_{12} = 1.0$, $P = 1$s, and $i = 30^\circ$.

to the pulsed fraction profile. In the case of increased magnetospheric radius, the higher temperature regions on the envelope make up a smaller proportion of the total envelope area, and so there is a larger change to the effective area during one full rotation. Hence the pulsed fraction is larger for all energy intervals.

The pulsed fraction break occurring at a lower energy also naturally follows from the explanation in the accretion luminosity case. In this case, the magnetospheric radius is increased with increasing magnetic field strength, which results in the truncation of the disc farther from the compact object. Thus the inner disc temperature is cooler and so the peak of the disc flux is at a lower energy.

In testing the model parameters ξ and P, there was no significant change to the best-fit component temperatures nor in the underlying model variables when these parameters were varied within their respective range of validity, except for parameter values close to the limits of validity, e.g. when the period is close to the propeller

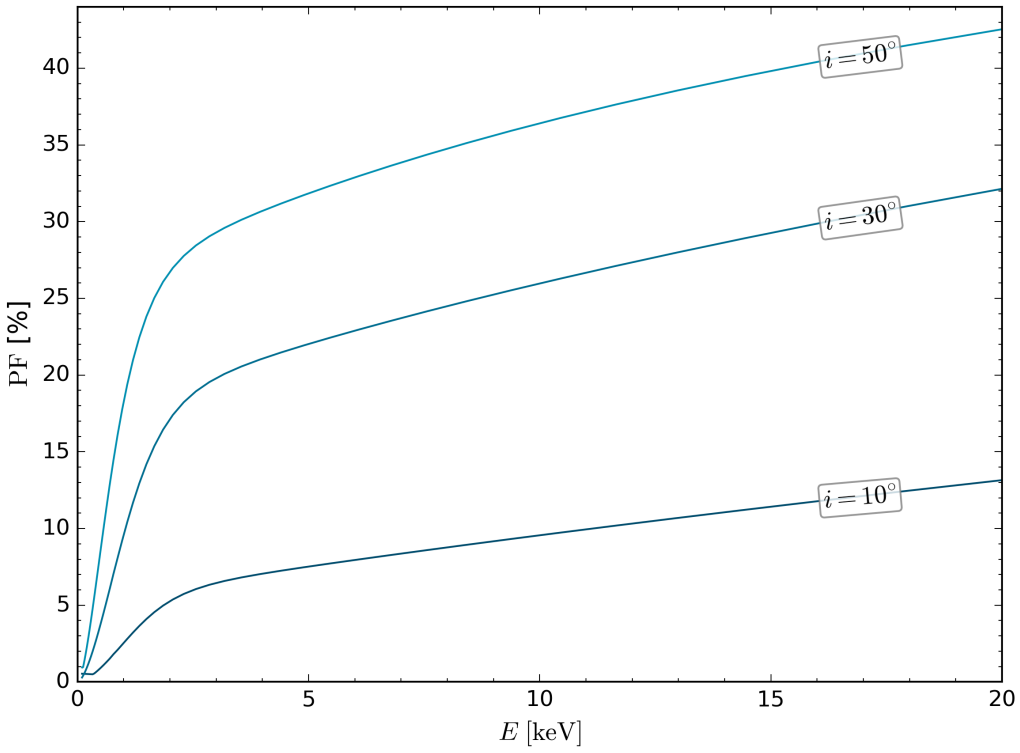

Figure 4.8: The pulsed fraction as a function of energy for models with different inclinations. The blue, green, and red lines show the pulsed fraction profile for models calculated using $i = 10^\circ,\ 30^\circ,\ 50^\circ$ respectively. The other model parameters were fixed to $L_{39} = 20$, $B_{12} = 1$, $\xi = 10^\circ$, $P = 1$s.

regime. However, an examination of the model behaviour in these scenarios is beyond the scope of this work, since the parameter limits are only approximated.

Despite no change in the underlying model variables, a variation of ξ, well within the validity limits, produces a substantial difference to the pulsed fraction, which is shown in figure 4.7. In this case, the pulsed fraction is not changed as a result of an altered contribution from the disc and the envelope emission components. Instead, the pulsed fraction varies with increasing tilt because of the altered viewing geometry to the envelope from the observer LOS. The high temperature region on the envelope is located close to the magnetospheric equator so when the magnetic moment is tilted relative to the spin axis, the high temperature region presents an effective area that depends on the phase of the rotation. With increasing ξ, the change in the effective area during one full rotation is larger and hence producing a larger pulsed fraction at all energies without a difference in the energy at which the break

occurs.

One notable divergence is in the pulsed fraction profile for the model with $\xi = 30^\circ$, which can be seen to flat-line after the break. This change can be understood as a result of the specifics of the viewing geometry to the envelope, in particular that the points of hottest temperature on the envelope are visible throughout the entire rotation. Hence, the envelope flux minimum (even at high energies) is non-vanishing, which results in an upper limit of less than 100% to the pulsed fraction.

In the case of varying the parameter i, the underlying model variables are completely independent of the viewing angle so, again, there is no change to the phase-averaged spectrum for most models. However, at high inclinations, $i \gtrsim 60^\circ$, the best-fit temperature for the mcd component decreased. This can be understood as an effect of a partial obscuration of the inner disc by the envelope. The fraction of the inner disc obscured by the envelope increases as the LOS angle increases so the hotter parts of the disc contribute less to the overall disc emission. Hence, the resulting characteristic mcd temperature obtained from the fit is lowered.

For the same reasons as in the analysis of ξ, the changes of i produce a substantial difference to the pulsed fraction, which is shown in figure 4.8. However, In this case, the break of the pulsed fraction profile occurs at a lower energy for models with larger i. This is an effect of the inner disc obscuration by the envelope (described above), which results in a lower disc specific flux at energies for which the inner disc is the main contributor. Hence, the energy at which the envelope flux dominates is down-shifted.

4.2.1 Parameter constraints

The envelope model as described in §4.1 is valid provided that the accretion column emission is thermalised inside the magnetosphere cavity. This condition holds when the envelope is optically thick, i.e. $\tau \gg 1$. As previously discussed by Mushtukov et al. (2017), the condition of an optically thick envelope translates to a constraint on the model parameters for self-consistent models. In the case of models with $\xi = 0^\circ$, the constraint can be approximated by an accretion luminosity bound: $L_{39} \gtrsim B_{12}^{1/4}$. In the case of models with $\xi > 0^\circ$ i.e. a tilted magnetic axis to the spin axis,

the equivalent minimum accretion luminosity bound depends on ξ and must be computed numerically.

Another constraint on model parameters comes from the fact that the radiation contained in the cavity exerts a pressure on the envelope walls. Since the material is channelled along magnetic field lines, the magnetic field must be strong enough to confine the accretion flow against the radiation pressure. As a rough approximation, this means that the magnetic pressure (at the magnetospheric radius) is required to be higher than the radiation pressure for the model to be self-consistent.

This translates into an upper bound for the accretion luminosity as a function of the magnetic field strength. The exact maximum luminosity also depends on ξ, due to the effect of the magnetic field tilt on $T_{\rm in}$, and thus must be computed numerically.

The minimum and maximum accretion luminosity is calculated as a function of the mangetic field strength, for models with fixed $P = 1$s and for various values of ξ. The results are shown in figure 4.9. The curves are truncated for the maximum accretion luminosity at the approximate magnetic field strength for which the maximum accretion luminosity becomes lower than the minimum accretion luminosity for the corresponding models. Beyond this point, the cavity temperature is not physical.

Specifically for the minimum accretion luminosity, the sharp increase reflects the progressive onset of a propeller mechanism. This is the case when centrifugal forces from the rotating magnetosphere (which are included in the velocity expression) become progressively dominant for larger magnetosphere radii, which in turn decrease the velocity along the magnetic field lines and eventually halting accretion altogether.

The self-consistency conditions rule out models with accretion luminosities $\lesssim 10^{39}$erg s^{-1} or $\gtrsim 10^{40}$erg s^{-1}, and in general models with tilts $\xi > 40^{\circ}$. Since the accretion luminosity is twice the envelope luminosity, i.e. the luminosity used to calculate the emission as used in equation (4.4), the maximum luminosity constraint would exclude astrophysical sources with observed X-ray luminosi-

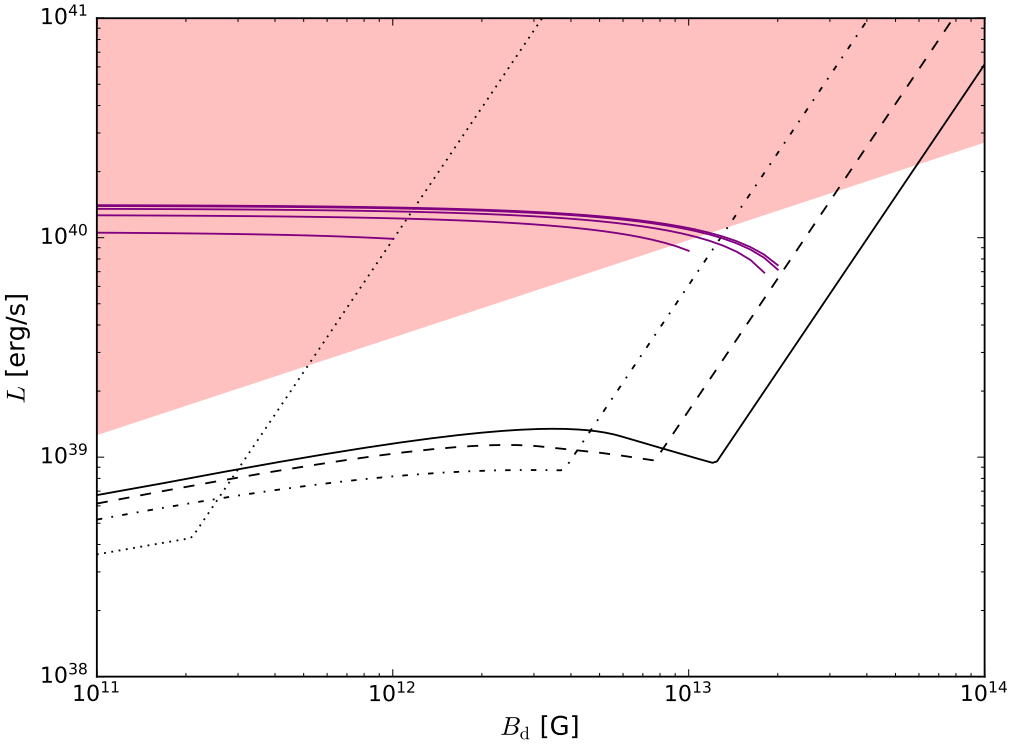

Figure 4.9: The accretion luminosity bounds for an optically thick envelope, $\tau > 1$, as a function of the dipole field strength. All models are calculated with $P = 1$s. The black solid, dashed, dot-dashed, and dotted lines indicate the minimum accretion luminosity for models with $\xi = 0°, 20°, 30°, 40°$ respectively. The minimum accretion luminosity line for models with $\xi = 10°$ overlaps with the minimum accretion luminosity line for models with $\xi = 0°$ so are omitted. The progressively lower solid purple lines indicate the maximum accretion luminosity for models with $\xi = 0°, 10°, 20°, 30°, 40°$. These lines have been truncated at the last $B_{\rm d}$ for which the maximum luminosity is greater than the minimum luminosity for the corresponding models. The shaded red region indicates the set of parameters for which the disc is super-critical.

ties $\gtrsim 5 \times 10^{39}$erg s^{-1}. However, the anisotropy of the emission from the envelope means that the observed luminosity (calculated assuming isotropic emission) can be greater than the envelope luminosity. This luminosity amplification increases from a factor ~ 1.1 to $\gtrsim 2$ for increasing viewing angle i. Thus, for real astrophysical sources, the apparent X-ray luminosity can be approximated as up to the accretion luminosity. The full investigation of the luminosity amplification for an optically thick envelope is left for a future work.

4.2.2 Application to sources

In the following, I present the application of this model to two PULX sources: NGC 7793 P13 (Fürst et al., 2016), and NGC 5907 ULX1 (Israel et al., 2017a). These sources were chosen because the pulsed fraction data was available for multiple energy bands and because they were the sources from the previous chapter §3.

The aim was to identify whether the optically thick envelope model as described in §4.1 is capable of explaining the spectra and pulsed fraction data. In particular, I attempt to find a model that simultaneously agrees with the modelled observational spectrum (as calculated by Koliopanos et al. 2017) and the pulsed fraction profile of each source.

To find a suitable model for each source, firstly, the possible set of model parameters (specifically accretion luminosity and magnetic field strength) is narrowed by using the temperatures from the best-fit mcd+bb spectral model from Koliopanos et al. (2017). Secondly, the values of ξ and i are varied to find a geometric configuration that best reproduces the pulsed fraction profile of the observed X-ray data. These data are taken from Fürst et al. (2016) and Israel et al. (2017a) for the sources NGC7793 P13 and NGC5907 ULX1 respectively.

4.2.2.1 NGC 7793 P13

The spectrum of the *XMM-Newton* observation of NGC 7793 P13 (obs. 0748390901), in the $0.3-10$ keV energy band, can be fitted by a combination of two thermal components, one representing the disc (mcd model), and one representing the hotter envelope (bb model), with $T_{\rm mcd} \approx 0.6$ keV and $T_{\rm bb} \approx 1.7$ keV, respectively (see Koliopanos et al. 2017). The X-ray luminosity for the *XMM-Newton* observation is $L \sim 7 \times 10^{39}$erg s^{-1} (assuming isotropic emission and a distance of ≈ 3.6 Mpc), and the spin period of the source is $P \approx 0.4$ s (Fürst et al., 2016).

The synthetic spectra for models with $L_{39} = 10$ are generated so that the flux from the synthetic spectra is similar in value to the observed flux. Models with $B_{12} = 0.55$ were able to produce synthetic spectra with best-fit temperatures of $T_{\rm mcd} \approx 0.8$ keV and $T_{\rm bb} \approx 1.6$ keV, which are similar to the spectrum from the

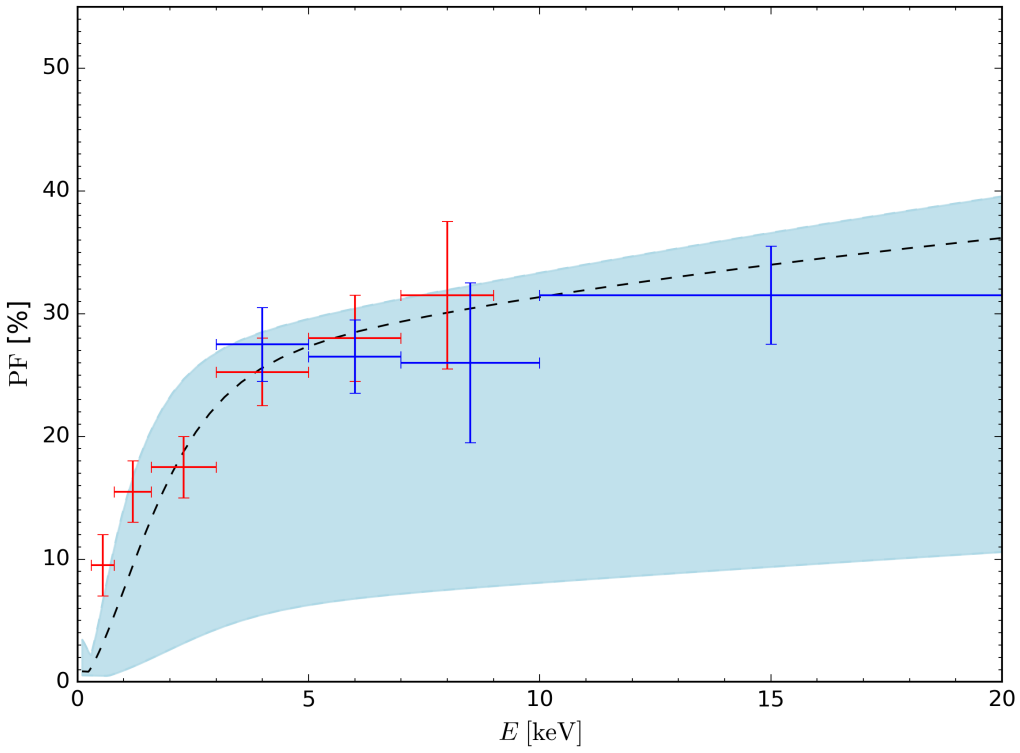

Figure 4.10: The pulsed fraction as a function of energy for the source NGC7793 P13. The red and blue points with error bars are the observed *XMM-Newton* and *NuSTAR* data, respectively, reported by Fürst et al. (2016). The pulsed fraction profile shown is from a model with $L_{39} = 10$, $B_{12} = 0.55$, $P = 0.4$ s, $\xi = 10^\circ$. The blue shaded region indicates the pulsed fraction profiles obtainable from this model by varying the inclination i (from $i = 10^\circ$ for the region bounding line at the bottom to $i = 70^\circ$ for the region bounding line at the top). The dashed line in the blue region indicates the pulsed fraction for a model with $i = 45^\circ$, which we found to most closely match the pulsed fraction data.

observation.

Using the model parameters obtained from matching with the observed spectrum, a model with $\xi = 10^\circ$ and $i = 45^\circ$ were able to closely match the pulsed fractions as reported by Fürst et al. (2016) in the energy intervals $0.3-0.8,\ 0.8-1.6,\ 1.6-3.0,\ 3.0-5.0,\ 5.0-7.0,\ 7.0-9.0$ keV and $3.0-5.0,\ 5.0-7.0,\ 7.0-10.0,\ 10.0-20.0$ keV (for *XMM-Newton* and *NuSTAR* data sets respectively). The results are shown in figure 4.10. For this particular model, the overall trend of the pulsed fraction profile is consistent with the observational data and the higher energy (> 3.0 keV) pulsed fraction values are all within the 1σ error margin.

4.2.2.2 NGC 5907 ULX1

NGC5907 ULX1 is the brightest PULX observed to date, with a luminosity that exceeds ~ 500 times the NS Eddington luminosity in some observations (Israel et al., 2017a). For this specific application, the synethic spectra of the model was matched to the spectral data from *XMM-Newton* observation 072956AS1301 (Koliopanos et al., 2017), which suggest an X-ray luminosity of $\sim 8.3 \times 10^{40}$erg s^{-1} (assuming isotropic emission and a distance of ≈ 17 Mpc). The best-fit mcd+bb model in this case has characteristic temperatures $T_{\rm mcd} \approx 0.7$ keV and $T_{\rm bb} \approx 1.4$ keV respectively. A spin period of $P \approx 1.1$ s was used for the models (Israel et al., 2017a).

To match the observed flux of the source would require $L_{39} \sim 100$, which is above the maximum accretion luminosity of our models. Instead, models with an accretion luminosity of $L_{39} = 10$ and a dipole magnetic field strength parameter of $B_{12} = 0.8$ had a similar synthetic spectrum to the observed spectrum, with best-fit temperatures of $T_{\rm mcd} \approx 0.7$ keV and $T_{\rm bb} \approx 1.4$ keV. This result suggests that the spectrum can be adequately described by the optically thick envelope model and that there is an additional mechanism responsible for the amplification of the observed flux.

Together with the accretion luminosity and magnetic field strength parameters used above, a model with $\xi = 10^\circ$ and $i = 25^\circ$ was able to reproduce the pulsed fractions as reported by Israel et al. (2017a) in the energy intervals < 2.5 keV and > 7 keV. The results are shown in figure 4.11.

4.3 Discussion and Conclusions

The model presented in this work is applicable in scenarios where the accreting NS has a magnetic field $B \gtrsim 10^{11}$ G, and the accretion rate is $\gtrsim 10^{39}$ erg s^{-1}, such that an optically thick envelope can develop. If there is little or no beaming and if the dipole magnetic field strength is typical of X-ray pulsars, PULXs fall in the range of applicability.

This study is the first to account for the tilt of the dipole moment from the spin-axis in the calculations of the velocity of the accreting material and the optical depth

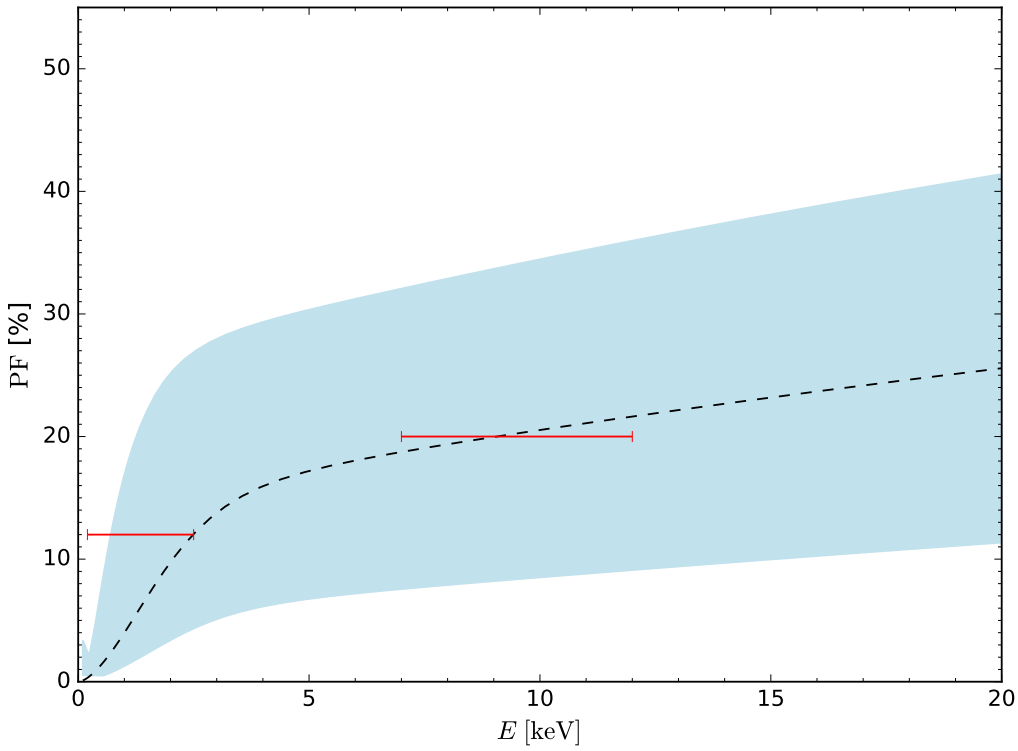

Figure 4.11: The pulsed fraction as a function of energy for the source NGC5907 ULX1. The red bars are pulsed fraction values given in specific energy intervals ($0-2.5$ keV and $7-12$ keV) as reported by Israel et al. (2017a). The pulsed fraction profile shown is from a model with $L_{39}=10$, $B_{12}=0.8$, $P=1.1$ s, $\xi=10^{\circ}$. The blue shaded region indicates the pulsed fraction profiles obtainable from this model by varying the inclination (from $i=10^{\circ}$ for the region bounding line below to $i=70^{\circ}$ for the region bounding line above). The dashed line in the blue region indicates the pulsed fraction profile for the model with $i=25^{\circ}$, which we found to most closely match the pulsed fraction data.

of the envelope. I found an analytical solution to the velocity of the accreting material, which decreased computation time and enabled comparison of different model parameters. Crucially, a tilt of the dipole moment leads to a non-homogeneous temperature distribution on the envelope, which contributes to a greater pulsed emission as the NS rotates.

The main aim of this work was to understand the observational implications of an optically thick envelope. In particular, the pulsed fraction profile and phase-averaged spectrum was studied by comparing the synthetic model data with observational data from PULXs.

These models reproduced the trend of increasing pulsed fraction with increasing photon energy, which is observed in PULXs (and in fact a large pulsed fraction at high photon energies is a typical feature of X-ray pulsars in general). In particular, they were able to match the pulsed fraction profile of the two PULXs studied for this work: NGC7793 P13 and NGC5907 ULX1. In fact, a range of pulsed fractions was obtained, from $< 5\%$ to $\sim 50\%$ (depending on the tilt and viewing angle). Thus, the optically thick envelope scenario is also consistent with low pulsed fractions, such as that measured for the PULX NGC1313 X-2 by Sathyaprakash et al. (2019), provided the viewing angle is close to the spin-axis (as suggested by these authors) and the dipole magnetic field tilt is small.

The synethic spectra produced by these models are broadly consistent with a double thermal spectral model, which has previously been used to analyse ULX spectra (Koliopanos et al., 2017). In particular, model parameters were found that reproduced the mcd+bb best-fit parameters for NGC7793 P13 and NGC5907 ULX1.

While model parameters were found that reproduced the spectral best-fit parameters of NGC5907 ULX1, a lower accretion luminosity parameter was used in the models than the value of the observed luminosity. This was necessary because the value of the observed luminosity is an order of magnitude larger than the maximum accretion luminosity for the optically thick envelope models (see §3.2.5), which suggests the need for another mechanism to explain the observed luminosity, e.g. luminosity amplification through geometrical beaming by optically thick outflows from a super-Eddington accretion disc (King & Lasota, 2020; Mushtukov et al., 2021; Mushtukov & Portegies Zwart, 2023).

A possible mechanism for luminosity amplification in the optically thick envelope model comes from the accretion column emission that is not injected into the cavity. This part of the emission was not included in this work since the focus was to model the envelope and disc emission. This emission from the accretion column accounts for half of the total accretion luminosity and it is funnelled along a narrow cone aligned with the magnetic axis (since the envelope exterior is optically thick).

Hence, this emission is highly an-isotropic and would contribute significantly to a luminosity amplification effect for observers that are within the emission cone.

The contribution of the accretion column to the spectrum requires a full radiative transfer calculation, which is beyond the scope of this work. However, I speculate that this emission would be dominated by hard X-rays since it comes from a relatively small region. In fact, Walton et al. (2018) find a hard X-ray power-law excess in the pulsed part of the broadband spectra of NGC7793 P13 and NGC5907 ULX1 after fitting the lower energy spectra with an mcd+bb model, which could indicate that this component of the accretion column emission does contribute in these sources.

The spectral model best-fit parameters for both of the PULXs studied here suggest that the dipole magnetic field strength is $< 10^{12}$G at the NS surface. However, the locally super-Eddington luminosity in the accretion column requires a magnetar-like surface magnetic field strength, i.e. $\gtrsim 10^{14}$G (Mushtukov et al., 2015). This contrast can be explained by the presence of significant multipole components in the magnetic field, i.e. a more complex magnetic field topology than a pure dipole (Brice et al., 2021).

As part of this modelling, several simplifying assumptions were made that may change the specifics of the phase-resolved synethic spectra. One of these assumptions is in the use of the Shakura & Sunyaev (1973) thin accretion disc model and its spectral profile. This could be inaccurate at super-critical accretion rates (locally super-Eddington for the disc) because the disc becomes geometrically thick due to radiation pressure and the disc may be advection dominated (Poutanen et al., 2007; Chashkina et al., 2019).

A more suitable disc model for this regime, (e.g. see Chashkina et al., 2017, 2019), would take into account the effect of the disc thickness on the disc emission and on the envelope emission. The spectral profile of a thick disc could differ substantially from that of a thin disc due to changes in the density and viscosity of the accreting material. In addition, a geometrically thick disc changes the spectral profile of the envelope by blocking a portion of the emitting area of the envelope,

which would result in a change of the temperature distribution on the envelope wall.

In the models of the two PULXs, the accretion disc is actually in the supercritical regime and so is expected to produce outflows (Shakura & Sunyaev, 1973). Material outflows would change the total mass accretion rate through the envelope (Mushtukov et al., 2019) and hence change the spectral profile from both the disc and envelope. In addition, certain LOS would be affected by the collimation of emission by optically thick outflowing material, in a similar scenario to that presented by King & Lasota (2020). In this work, the accretion luminosity was assumed to be equal to the mass accretion rate without any mass loss in outflows for simplicity. In principle, a ray-tracing computation could include the effect of collimation by outflows but this is left for a future work.

In conclusion, the observed pulsed fraction from NGC7793 P13 and NGC5907 ULX1 can be reproduced in this modelling of an optically thick envelope. In contrast, Mushtukov et al. (2021) found that the pulsed fraction values from these sources would be difficult to explain in the scenario with highly geometrically beamed emission.

4.4 Appendices

4.4.1 Envelope Cross-Section Area

The envelope cross-section area, A_c, given by equation (4.7) in §4.1.1 is calculated from geometrical considerations of the accretion flow.

An infinitesimal surface, $\mathrm{d}A_c$, perpendicular to the local magnetic field line direction, $\vec{B}$, is also perpendicular to the accretion flow direction. The infinitesimal surface extends in the azimuthal direction $\vec{\varphi}$ with total arc-length $2\pi r\cos\theta$ and extends in the direction $\vec{\varphi}\times\vec{B}$ with arc-length denoted by $\mathrm{d}\ell$. Hence $\mathrm{d}A_c = 2\pi r\cos\theta\mathrm{d}\ell$.

Under the assumption that the photon propagation direction through the optically thick envelope occurs in the $\vec{\varphi}\times\vec{B}$ direction, the distance is given by

$$D = \int_{R_m - P_m}^{R_m} \mathrm{d}\ell. \tag{4.21}$$

Approximating the circumference of the circles in the $\vec{\varphi}$ direction to be constant for all infinitesimal areas along the $\vec{\varphi} \times \vec{B}$ direction, i.e. by taking the value for the circumference at the field line at $R = R_m - \frac{1}{2}P_m$, gives

$$2\pi r \cos\theta = 2\pi \left(R_m - \frac{1}{2} P_m \right) \cos^3 \theta. \tag{4.22}$$

This can be justified since the greatest difference in the circumference is $2\pi P_m$ at latitude $\theta = 0°$. The infinitesimal surfaces along the $\vec{\varphi} \times \vec{B}$ direction can now be integrated, which gives

$$\int_R \mathrm{d}A_c \approx A_c = 2\pi \left(R_m - \frac{1}{2} P_m \right) D \cos^3 \theta. \tag{4.23}$$

4.4.2 Distance to the spin axis in the magnetic reference frame

Points in the magnetic axis reference frame can be described in terms of an orthonormal basis

$$\{\vec{e}_1,\ \vec{e}_2,\ \vec{b}\}, \tag{4.24}$$

where $\vec{b}$ is aligned with the magnetic dipole moment and $\vec{e}_1,\ \vec{e}_2$ satisfy $\vec{e}_1 \cdot \vec{e}_2 \times \vec{b} = 1$. Since the dipole magnetic field is axially symmetric, we can choose $\vec{e}_1$ and $\vec{e}_2$ such that the spin axis direction vector, $\vec{\Omega}$, is given by

$$\vec{\Omega} = -\sin\xi \vec{e}_1 + \cos\xi \vec{b}, \tag{4.25}$$

where ξ is the angle of the tilt between the dipole magnetic moment and the spin axis.

Let points in the spin axis reference frame be described in terms of the orthonormal basis

$$\{\vec{e'}_1,\ \vec{e}_2,\ \vec{\Omega}\}, \tag{4.26}$$

which is related to the magnetic axis reference frame vector basis, namely through

the relations $\vec{e'}_1 = \cos\xi\vec{e}_1 + \sin\xi\vec{b}$ and the one given in equation (4.25). Hence a point (x,y,z) in the magnetic axis reference frame is given by

$$(x',y',z') = (x\cos\xi + z\sin\xi,\ y,\ -x\sin\xi + z\cos\xi) \tag{4.27}$$

in the spin axis reference frame. It follows that the distance squared of the point (x,y,z) from the spin axis is given by

$$\begin{aligned} d^2 &= x'^2 + y'^2 \\ &= x^2\cos^2\xi + z^2\sin^2\xi + 2xz\cos\xi\sin\xi + y^2, \end{aligned} \tag{4.28}$$

which in a spherical coordinate system, (r,θ,φ), of the magnetic axis reference frame becomes

$$\begin{aligned} d^2 = r^2\Big[&\cos^2\xi\cos^2\theta\cos^2\varphi + \sin^2\theta\sin^2\xi \\ &+ 2\cos\theta\cos\varphi\sin\theta\cos\xi\sin\xi + \cos^2\theta\sin^2\varphi\Big]. \end{aligned} \tag{4.29}$$

Note that θ is the latitude angle and φ is the azimuth angle.

4.4.3 Initial Angle for tilted magnetosphere

In the model, the normal to the disc plane is aligned with the spin axis. Hence, we obtain the initial angle, θ_0, where the accreting disc meets the magnetic field lines from equation (4.27) by setting $z' = H_m/2$, where H_m is the height of the disc at the magnetospheric radius. For dipole magnetic field lines extending to the magnetospheric radius, $r = R_m\cos^2\theta$, we obtain

$$\cos^2\theta_0\left[\cos\xi\sin\theta_0 - \sin\xi\cos\theta_0\cos\varphi\right] = \frac{1}{2}\frac{H_m}{R_m}. \tag{4.30}$$

In the case of geometrically thin disc, we set $H_m = 0$, which simplifies equation (4.30) to

$$\tan\theta_0 = \tan\xi\cos\varphi. \tag{4.31}$$

Note that $\theta_0 = \pi/2$ is a non-physical solution since the disc is actually truncated at the magnetospheric radius.

Chapter 5

General Conclusions

5.1 Summary

Previously, models of accretion onto a NS assumed a pure-dipole magnetic field topology for simplicity. In this thesis, I have shown that there is a significant change to the properties of the emission (that originates close to the NS surface) because of higher degree multipole components or a tilt in the magnetic field moment.

In addition, and particularly for highly-magnetised NS, I have shown that it is possible to find an analytical solution to the dynamics of the accreting material for a tilted (from the spin axis) magnetic field. I derived the velocity of accreting charges for a pure dipole magnetic field topology explicitly. This derivation is easily generalisable to the case of a multipolar magnetic field through the use of the curvilinear coordinate system presented in §2.

In §3, I adapted an accretion column model (for a highly-magnetised NS) by relaxing the assumption of a pure dipole magnetic field topology. I used the adapted accretion column model to diagnose the necessity for a more complex (than pure dipole) magnetic field topology in PULXs. This was done by taking into account constraints on the strength of the dipole component from the spin period and spin period derivative. The results showed a multipole component was necessary to explain the peak luminosity of NGC 5907 ULX-1. The other PULX studied in this work, NGC 7793 P13, had a lower peak luminosity by an order of magnitude but a multipole component was still necessary if no luminosity amplification was

assumed.

The magnetic field strengths and the complex magnetic field topology, found in this analysis, suggests PULXs are related to magnetars, which have similar strength and topology (Tong & Wang, 2019).

In §4, I investigated the phase-resolved spectrum from an optically thick, closed envelope, which is theorised to manifest for super-Eddington accretion onto a highly magnetised NS (Mushtukov et al., 2017). I enabled a systematic analysis of the envelope models by deriving an analytical expression for the velocity of accreting charges that are fixed on rotating and tilted (from the spin axis) magnetic field lines. The phase-resolved spectrum and pulsed fraction profiles were calculated for each model by ray-tracing emitting points on the envelope to an observer.

The aim of this work was to check the validity of the closed envelope model against the data on PULXs by comparing the synthetic pulsed fraction profile with the observed pulsed fraction profile. I showed that pulsed fraction profiles follow the general trend seen from the pulsed fraction profiles of PULXs: an increasing pulsed fraction with increasing energy. The synthetic pulsed fraction profiles were also consistent with the profile shape, namely starting with a sharp increase at energies $\lesssim$ 1keV followed by a shallower increase from $\sim$ 1keV. A subset of the synthetic pulsed fraction profiles matched the observed pulsed fraction profiles of NGC 7793 P13 and NGC 5907 ULX-1, which indicates the closed envelope model to be a favourable interpretation of PULXs.

5.2 Future Work

There are several directions for research made apparent by the work of this thesis. I divided these research projects into two categories. In the first category, the framework for the magnetic field structure can be further developed and applied to other settings. In the second category, the models can be extended for further investigation of PULXs. Each category is discussed in turn.

Foremost, the next study that directly relates to the work of this thesis is a systematic study of the changes to the polarization degree due to higher degree

multipole components (that dominate close to the surface). Taverna et al. (2015) studied the polarization fraction and angle of radiation from a NS that propagates through a QED polarized vacuum (that surrounds the NS) before arriving at an observer. The effect of the QED polarized vacuum is to align the magnetic field component of the radiation with the NS magnetic field direction until the adiabatic radius, where the effect is too weak and the polarization angle of the radiation is frozen in. Thus, the magnetic field topology at the adiabatic radius directly affects the final polarization angle. By applying the cuvilinear coordinate system in §2.1.1, the magnetic field direction at the adiabatic radius is easily found for more complex magnetic field topologies. The results of this research project would give a way to quantify the differences that are expected from variation in the magnetic field topology. They have applications to the IXPE mission, which attempts to measure the polarization of X-rays from astrophysical sources more precisely and brings with it a need to accurately assess the polarization.

In general, the dynamics of the accreting material near magnetic null points is not well understood. An analytical description of these dynamics is needed to calculate (without simulation) the geometry of hot-spots and the footprint of accretion columns in the case of a dipole plus quadrupole magnetic field topology. This hot-spot geometry is needed for a calculation of pulse profiles (here meaning the shape of the pulses in time) from a self-consistent model of accretion onto NSs. Hence, an understanding of the dynamics gives a way of relating the shapes of pulse profiles in accreting NSs with the magnetic field topology.

The curvilinear coordinate system of a axisymmetric magnetic field, described in §2.1.1 can be applied to the accretion column model. This allows for a consistent accounting of the curvature of the magnetic field lines, even for taller ($H > R_*$) accretion columns. By using the globally consistent curvilinear coordinate system (as done by Canalle et al. 2005) for the simplified hydrodynamical equations (of the accretion column model in §3.1), some of the assumptions used in the accretion column model can be relaxed, e.g. the maximum height for an accretion column is $H = R_*$ above the surface.

Once a way to account for the magnetic null points is found, it would also be possible to extend the accretion column model to compute the maximum luminosity from a NS with a dipole plus quadrupole magnetic field topology. The maximum luminosity can be compared with that of the pure dipole and dipole plus octupole topology. In the dipole plus quadrupole case, the geometric compression is not as much as in the dipole plus octupole case. Thus, some change to the maximum luminosity is expected from changes to the density and temperature of the accretion column.

In addition, it may be possible to extend the analysis of the effect of the magnetic field structure to include the toroidal components. Non-axisymmetric magnetic field topologies give rise to asymmetric pulse profiles. The results from this investigation would enable a method for interpretation of the asymmetries in observed pulse profiles in terms of the asymmetry (about the axis) of the magnetic field topology.

By using the curvilinear coordinate system for general magnetic field topologies and the ray-tracing technique, it is possible to study the pulsed fraction profiles from geometries other than the one considered in §4, e.g. an accretion curtain or accretion column, which applies to a variety of other sub-Eddington accreting NSs. This enables a robust comparison between the pulsed fraction profiles from surface hot-spots and from accretion columns, without resorting to approximations of the geometry (e.g. a cone).

For further investigation of PULXs, the work of this thesis (both §3 and §4) can be applied immediately to other known PULXs to infer trends in the population as a whole, e.g. whether or not multipole components are usually needed, whether or not super-Eddington accretion rates are usual.

However, there are a number of modifications that would improve the fidelity of the accretion column model. In particular by accounting for the ion contribution to the scattering cross-section and other QED effects, both of which may influence the emission properties from a hot ($\sim$ 100keV) and dense plasma (some of which are now starting to be addressed by Suleimanov et al. 2022). These proposed mod-

ifications are not new, and have already been addressed in other studies, e.g. the ion contribution to the scattering cross-section (Zane et al., 2001), and the vacuum resonance (Kaminker et al., 1982).

The inclusion of the proton cyclotron resonance in the accretion column model would provide information about the necessary conditions for proton cyclotron line formation in the accretion column of a super-Eddington accreting NS. This may alter the credence for the proton cyclotron line found in the spectrum of M51 ULX8 (Brightman et al., 2018).

In addition, a self-consistent treatment of the polarization normal modes that includes the scattering between the modes is desirable, since the maximum luminosity was seen to depend on the polarization degree (see §3.2.2). Currently in the accretion column model, the polarization degree is constant throughout, which is unlikely to be accurate given the variance in the temperature and density from the bottom to the top of the column.

Despite the development of super-Eddington discs models (Chashkina et al., 2017, 2019) and studies on the luminosity amplification from optically thick outflows (King, 2009; Mushtukov et al., 2021; Mushtukov & Portegies Zwart, 2023), there are no quantitative studies on the luminosity amplification from a highly magnetised NS accreting at super-Eddington rates, i.e. luminosity amplification from an optically thick envelope. The envelope model in this thesis only briefly begins to address the luminosity amplification. A more systematic study of the luminosity amplification is needed to properly assess the validity of applying the envelope model to the most luminous PULXs, since the accretion rate constraint (given in §4.2.1) should otherwise rule out most of the more luminous PULXs, including NGC 5907 ULX-1.

The results from studies of super-Eddington discs can be implemented for the envelope model. Unlike a thin disc, a thick disc would cover some of the envelope emitting area, which would change the spectrum of the envelope (from the current spectrum). This means a different set of model parameters would produce the best-fitting synthetic spectrum to the observed spectrum (of a particular PULX). Whether

this would resolve some of the issues with the inferred model parameters from the best-fit spectra is to be determined.

The use of the observed pulsed fraction profile as a diagnostic tool for the system can be applied more generally to spectral modelling of PULX. This works particularly well for PULXs because the soft X-ray part of PULX spectra is expected to be dominated by the emission from the disc (if the accretion rate is super-Eddington). The dominance of the disc emission in the soft X-rays bears out in the pulsed fraction profile because the soft X-rays have a much lower pulsed fraction than the hard X-rays. Thus, in the spectral models, there is (usually) a soft thermal component, which is attributed to the disc emission. The other (harder) spectral component is attributed to emission close to the NS, e.g. from the accretion column or from the envelope. This interpretation of the origins of the spectral components gives a new condition for validity through the use of the observed pulsed fraction profile. Using such a condition would narrow the range of possible spectral models.

This list is only a number of the questions that were raised while conducting the work in this thesis. Other questions related to the disc-magnetosphere interaction have resurfaced in the context of super-Eddington discs. Providing a theory to answer these questions would help in resolving questions about accretion more generally. PULXs serve as a rich source for testing our understanding of the physics of accretion.

Bibliography

Adams, F. C. & Gregory, S. G. (2012). Magnetically Controlled Accretion Flows onto Young Stellar Objects. , 744(1), 55.

Bachetti, M., Harrison, F. A., Walton, D. J., Grefenstette, B. W., Chakrabarty, D., Fürst, F., Barret, D., Beloborodov, A., Boggs, S. E., Christensen, F. E., Craig, W. W., Fabian, A. C., Hailey, C. J., Hornschemeier, A., Kaspi, V., Kulkarni, S. R., Maccarone, T., Miller, J. M., Rana, V., Stern, D., Tendulkar, S. P., Tomsick, J., Webb, N. A., & Zhang, W. W. (2014). An ultraluminous X-ray source powered by an accreting neutron star. , 514(7521), 202–204.

Basko, M. M. & Sunyaev, R. A. (1975). Radiative transfer in a strong magnetic field and accreting X-ray pulsars. , 42(3), 311–321.

Basko, M. M. & Sunyaev, R. A. (1976). The limiting luminosity of accreting neutron stars with magnetic fields. , 175, 395–417.

Becker, P. A. (1998). Dynamical Structure of Radiation-dominated Pulsar Accretion Shocks. , 498(2), 790–801.

Becker, P. A. & Wolff, M. T. (2007). Thermal and Bulk Comptonization in Accretion-powered X-Ray Pulsars. , 654(1), 435–457.

Becker, P. A. & Wolff, M. T. (2022). A Generalized Analytical Model for Thermal and Bulk Comptonization in Accretion-powered X-Ray Pulsars. , 939(2), 67.

Bildsten, L., Chakrabarty, D., Chiu, J., Finger, M. H., Koh, D. T., Nelson, R. W., Prince, T. A., Rubin, B. C., Scott, D. M., Stollberg, M., Vaughan, B. A., Wilson,

C. A., & Wilson, R. B. (1997). Observations of Accreting Pulsars. , 113(2), 367–408.

Bilous, A. V., Watts, A. L., Harding, A. K., Riley, T. E., Arzoumanian, Z., Bogdanov, S., Gendreau, K. C., Ray, P. S., Guillot, S., Ho, W. C. G., & Chakrabarty, D. (2019). A NICER View of PSR J0030+0451: Evidence for a Global-scale Multipolar Magnetic Field. , 887(1), L23.

Borghese, A., Rea, N., Coti Zelati, F., Tiengo, A., & Turolla, R. (2015). Discovery of a Strongly Phase-variable Spectral Feature in the Isolated Neutron Star RX J0720.4-3125. , 807(1), L20.

Borghese, A., Rea, N., Coti Zelati, F., Tiengo, A., Turolla, R., & Zane, S. (2017). Narrow phase-dependent features in X-ray dim isolated neutron stars: a new detection and upper limits. , 468(3), 2975–2983.

Brice, N., Zane, S., Taverna, R., Turolla, R., & Wu, K. (2023). Observational properties of accreting neutron stars with an optically thick envelope. , 525(3), 4176–4185.

Brice, N., Zane, S., Turolla, R., & Wu, K. (2021). Super-eddington emission from accreting, highly magnetized neutron stars with a multipolar magnetic field. , 504(1), 701–715.

Brightman, M., Harrison, F. A., Fürst, F., Middleton, M. J., Walton, D. J., Stern, D., Fabian, A. C., Heida, M., Barret, D., & Bachetti, M. (2018). Magnetic field strength of a neutron-star-powered ultraluminous X-ray source. *Nature Astronomy*, 2, 312–316.

Canalle, J. B. G., Saxton, C. J., Wu, K., Cropper, M., & Ramsay, G. (2005). Accretion in dipole magnetic fields: flow structure and X-ray emission of accreting white dwarfs. , 440(1), 185–198.

Carpano, S., Haberl, F., Maitra, C., & Vasilopoulos, G. (2018). Discovery of pulsations from NGC 300 ULX1 and its fast period evolution. , 476(1), L45–L49.

Chashkina, A., Abolmasov, P., & Poutanen, J. (2017). Super-Eddington accretion on to a magnetized neutron star. , 470(3), 2799–2813.

Chashkina, A., Lipunova, G., Abolmasov, P., & Poutanen, J. (2019). Super-Eddington accretion discs with advection and outflows around magnetized neutron stars. , 626, A18.

Colbert, E. J. M. & Mushotzky, R. F. (1999). The Nature of Accreting Black Holes in Nearby Galaxy Nuclei. , 519(1), 89–107.

Dall'Osso, S., Perna, R., Papitto, A., Bozzo, E., & Stella, L. (2016). The accretion regimes of a highly magnetized NS: the unique case of NuSTAR J095551+6940.8. , 457(3), 3076–3083.

Davidson, K. & Ostriker, J. P. (1973). Neutron-Star Accretion in a Stellar Wind: Model for a Pulsed X-Ray Source. , 179, 585–598.

Erkut, M. H., Türkoğlu, M. M., Ekşi, K. Y., & Alpar, M. A. (2020). On the Magnetic Fields, Beaming Fractions, and Fastness Parameters of Pulsating Ultraluminous X-Ray Sources. , 899(2), 97.

Fabrika, S. N., Atapin, K. E., Vinokurov, A. S., & Sholukhova, O. N. (2021). Ultraluminous X-Ray Sources. *Astrophysical Bulletin*, 76(1), 6–38.

Fürst, F., Walton, D. J., Harrison, F. A., Stern, D., Barret, D., Brightman, M., Fabian, A. C., Grefenstette, B., Madsen, K. K., Middleton, M. J., Miller, J. M., Pottschmidt, K., Ptak, A., Rana, V., & Webb, N. (2016). Discovery of Coherent Pulsations from the Ultraluminous X-Ray Source NGC 7793 P13. , 831(2), L14.

Ghosh, P. & Lamb, F. K. (1978). Disk accretion by magnetic neutron stars. , 223, L83–L87.

Ghosh, P. & Lamb, F. K. (1979). Accretion by rotating magnetic neutron stars. II. Radial and vertical structure of the transition zone in disk accretion. , 232, 259–276.

Ghosh, P., Lamb, F. K., & Pethick, C. J. (1977). Accretion by rotating magnetic neutron stars. I. Flow of matter inside the magnetosphere and its implications for spin-up and spin-down of the star. , 217, 578–596.

Giacconi, R. (1975). Her X-1 and Cen X-3 revisited. In P. G. Bergman, E. J. Fenyves, & L. Motz (Eds.), *Seventh Texas Symposium on Relativistic Astrophysics*, volume 262 (pp. 312–330).

Giacconi, R., Gursky, H., Kellogg, E., Schreier, E., & Tananbaum, H. (1971). Discovery of Periodic X-Ray Pulsations in Centaurus X-3 from UHURU. , 167, L67.

Gladstone, J. C., Roberts, T. P., & Done, C. (2009). The ultraluminous state. , 397(4), 1836–1851.

Harding, A. K. & Lai, D. (2006). Physics of strongly magnetized neutron stars. *Reports on Progress in Physics*, 69(9), 2631–2708.

Illarionov, A. F. & Sunyaev, R. A. (1975). Why the Number of Galactic X-ray Stars Is so Small? , 39, 185.

Israel, G. L., Belfiore, A., Stella, L., Esposito, P., Casella, P., De Luca, A., Marelli, M., Papitto, A., Perri, M., Puccetti, S., Castillo, G. A. R., Salvetti, D., Tiengo, A., Zampieri, L., D'Agostino, D., Greiner, J., Haberl, F., Novara, G., Salvaterra, R., Turolla, R., Watson, M., Wilms, J., & Wolter, A. (2017a). An accreting pulsar with extreme properties drives an ultraluminous x-ray source in NGC 5907. *Science*, 355(6327), 817–819.

Israel, G. L., Papitto, A., Esposito, P., Stella, L., Zampieri, L., Belfiore, A., Rodríguez Castillo, G. A., De Luca, A., Tiengo, A., Haberl, F., Greiner, J., Salvaterra, R., Sandrelli, S., & Lisini, G. (2017b). Discovery of a 0.42-s pulsar in the ultraluminous X-ray source NGC 7793 P13. , 466(1), L48–L52.

Kaaret, P., Feng, H., & Roberts, T. P. (2017). Ultraluminous X-Ray Sources. , 55(1), 303–341.

Kaminker, A. D., Pavlov, G. G., & Shibanov, I. A. (1982). Radiation from a Strongly Magnetized Plasma - the Case of Predominant Scattering. , 86(2), 249–297.

King, A. & Lasota, J.-P. (2020). Pulsing and non-pulsing ULXs: the iceberg emerges. , 494(3), 3611–3615.

King, A., Lasota, J.-P., & Middleton, M. (2023). Ultraluminous X-ray sources. , 96, 101672.

King, A. R. (2009). Masses, beaming and Eddington ratios in ultraluminous X-ray sources. , 393(1), L41–L44.

Koliopanos, F., Vasilopoulos, G., Godet, O., Bachetti, M., Webb, N. A., & Barret, D. (2017). ULX spectra revisited: Accreting, highly magnetized neutron stars as the engines of ultraluminous X-ray sources. , 608, A47.

Kosec, P., Pinto, C., Walton, D. J., Fabian, A. C., Bachetti, M., Brightman, M., Fürst, F., & Grefenstette, B. W. (2018). Evidence for a variable Ultrafast Outflow in the newly discovered Ultraluminous Pulsar NGC 300 ULX-1. , 479(3), 3978–3986.

Lai, D. (2014). Theory of Disk Accretion onto Magnetic Stars. In *European Physical Journal Web of Conferences*, volume 64 of *European Physical Journal Web of Conferences* (pp. 01001).

Lamb, F. K. (1977). Knowledge of Neutron Stars from X-Ray Observations. In M. D. Papagiannis (Ed.), *Eighth Texas Symposium on Relativistic Astrophysics*, volume 302 (pp. 482).

Lamb, F. K., Pethick, C. J., & Pines, D. (1973). A Model for Compact X-Ray Sources: Accretion by Rotating Magnetic Stars. , 184, 271–290.

Li, X. D. & Wang, Z. R. (1999). Disk Accretion onto Magnetized Neutron Stars: The Inner Disk Radius and Fastness Parameter. , 513(2), 845–848.

Lyubarskii, Y. E. & Syunyaev, R. A. (1988). Accretion Column Structure. *Soviet Astronomy Letters*, 14, 390.

Makishima, K., Maejima, Y., Mitsuda, K., Bradt, H. V., Remillard, R. A., Tuohy, I. R., Hoshi, R., & Nakagawa, M. (1986). Simultaneous X-Ray and Optical Observations of GX 339-4 in an X-Ray High State. , 308, 635.

Meszaros, P. (1992). *High-energy radiation from magnetized neutron stars*.

Mushtukov, A. & Tsygankov, S. (2022). Accreting strongly magnetised neutron stars: X-ray Pulsars. *arXiv e-prints*, (pp. arXiv:2204.14185).

Mushtukov, A. A., Ingram, A., Middleton, M., Nagirner, D. I., & van der Klis, M. (2019). Timing properties of ULX pulsars: optically thick envelopes and outflows. , 484(1), 687–697.

Mushtukov, A. A. & Portegies Zwart, S. (2023). Bright X-ray pulsars: how outflows influence beaming, pulsations and pulse phase lags. , 518(4), 5457–5464.

Mushtukov, A. A., Portegies Zwart, S., Tsygankov, S. S., Nagirner, D. I., & Poutanen, J. (2021). Pulsating ULXs: large pulsed fraction excludes strong beaming. , 501(2), 2424–2429.

Mushtukov, A. A., Suleimanov, V. F., Tsygankov, S. S., & Ingram, A. (2017). Optically thick envelopes around ULXs powered by accreating neutron stars. , 467(1), 1202–1208.

Mushtukov, A. A., Suleimanov, V. F., Tsygankov, S. S., & Poutanen, J. (2015). On the maximum accretion luminosity of magnetized neutron stars: connecting X-ray pulsars and ultraluminous X-ray sources. , 454(3), 2539–2548.

Mushtukov, A. A., Tsygankov, S. S., Suleimanov, V. F., & Poutanen, J. (2018). Ultraluminous X-ray sources as neutrino pulsars. , 476(3), 2867–2873.

Page, D. & Sarmiento, A. (1996). Surface Temperature of a Magnetized Neutron Star and Interpretation of the ROSAT Data. II. , 473, 1067.

Pavan, L., Turolla, R., Zane, S., & Nobili, L. (2009). Topology of magnetars external field - I. Axially symmetric fields. , 395(2), 753–763.

Pinto, C., Alston, W., Soria, R., Middleton, M. J., Walton, D. J., Sutton, A. D., Fabian, A. C., Earnshaw, H., Urquhart, R., Kara, E., & Roberts, T. P. (2017). From ultraluminous X-ray sources to ultraluminous supersoft sources: NGC 55 ULX, the missing link. , 468(3), 2865–2883.

Pinto, C., Middleton, M. J., & Fabian, A. C. (2016). Resolved atomic lines reveal outflows in two ultraluminous X-ray sources. , 533(7601), 64–67.

Poutanen, J., Lipunova, G., Fabrika, S., Butkevich, A. G., & Abolmasov, P. (2007). Supercritically accreting stellar mass black holes as ultraluminous X-ray sources. , 377(3), 1187–1194.

Pringle, J. E. & Rees, M. J. (1972). Accretion Disc Models for Compact X-Ray Sources. , 21, 1.

Rappaport, S. & Joss, P. C. (1977). Binary X-ray pulsars. , 266(5598), 123–125.

Rodríguez Castillo, G. A., Israel, G. L., Belfiore, A., Bernardini, F., Esposito, P., Pintore, F., De Luca, A., Papitto, A., Stella, L., Tiengo, A., Zampieri, L., Bachetti, M., Brightman, M., Casella, P., D'Agostino, D., Dall'Osso, S., Earnshaw, H. P., Fürst, F., Haberl, F., Harrison, F. A., Mapelli, M., Marelli, M., Middleton, M., Pinto, C., Roberts, T. P., Salvaterra, R., Turolla, R., Walton, D. J., & Wolter, A. (2020). Discovery of a 2.8 s Pulsar in a 2 Day Orbit High-mass X-Ray Binary Powering the Ultraluminous X-Ray Source ULX-7 in M51. , 895(1), 60.

Sathyaprakash, R., Roberts, T. P., Walton, D. J., Fuerst, F., Bachetti, M., Pinto, C., Alston, W. N., Earnshaw, H. P., Fabian, A. C., Middleton, M. J., & Soria, R. (2019). The discovery of weak coherent pulsations in the ultraluminous X-ray source NGC 1313 X-2. , 488(1), L35–L40.

Savonije, G. J. (1978). Roche-lobe overflow in X-ray binaries. , 62(3), 317–338.

Schreier, E., Levinson, R., Gursky, H., Kellogg, E., Tananbaum, H., & Giacconi, R. (1972). Evidence for the Binary Nature of Centaurus X-3 from UHURU X-Ray Observations. , 172, L79.

Shakura, N. I. & Sunyaev, R. A. (1973). Black holes in binary systems. Observational appearance. , 24, 337–355.

Spruit, H. C. (2008). Origin of neutron star magnetic fields. In C. Bassa, Z. Wang, A. Cumming, & V. M. Kaspi (Eds.), *40 Years of Pulsars: Millisecond Pulsars, Magnetars and More*, volume 983 of *American Institute of Physics Conference Series* (pp. 391–398).

Staubert, R., Trümper, J., Kendziorra, E., Klochkov, D., Postnov, K., Kretschmar, P., Pottschmidt, K., Haberl, F., Rothschild, R. E., Santangelo, A., Wilms, J., Kreykenbohm, I., & Fürst, F. (2019). Cyclotron lines in highly magnetized neutron stars. , 622, A61.

Stella, L., White, N. E., & Rosner, R. (1986). Intermittent Stellar Wind Acceleration and the Long-Term Activity of Population I Binary Systems Containing an X-Ray Pulsar. , 308, 669.

Stobbart, A. M., Roberts, T. P., & Wilms, J. (2006). XMM-Newton observations of the brightest ultraluminous X-ray sources. , 368(1), 397–413.

Suleimanov, V. F., Mushtukov, A. A., Ognev, I., Doroshenko, V. A., & Werner, K. (2022). Mean opacities of a strongly magnetized high-temperature plasma. , 517(3), 4022–4033.

Tananbaum, H., Gursky, H., Kellogg, E. M., Levinson, R., Schreier, E., & Giacconi, R. (1972). Discovery of a Periodic Pulsating Binary X-Ray Source in Hercules from UHURU. , 174, L143.

Taverna, R. & Turolla, R. (2017). On the spectrum and polarization of magnetar flare emission. , 469(3), 3610–3628.

Taverna, R., Turolla, R., Gonzalez Caniulef, D., Zane, S., Muleri, F., & Soffitta, P. (2015). Polarization of neutron star surface emission: a systematic analysis. , 454(3), 3254–3266.

Tiengo, A., Esposito, P., Mereghetti, S., Turolla, R., Nobili, L., Gastaldello, F., Götz, D., Israel, G. L., Rea, N., Stella, L., Zane, S., & Bignami, G. F. (2013). A variable absorption feature in the X-ray spectrum of a magnetar. , 500(7462), 312–314.

Tong, H. & Wang, W. (2019). Accreting magnetars: linking ultraluminous X-ray pulsars and the slow pulsation X-ray pulsars. , 482(4), 4956–4964.

Truemper, J., Pietsch, W., Reppin, C., Voges, W., Staubert, R., & Kendziorra, E. (1978). Evidence for strong cyclotron line emission in the hard X-ray spectrum of Hercules X-1. , 219, L105–L110.

Tsygankov, S. S., Mushtukov, A. A., Suleimanov, V. F., & Poutanen, J. (2016). Propeller effect in action in the ultraluminous accreting magnetar M82 X-2. , 457(1), 1101–1106.

Veledina, A., Muleri, F., Poutanen, J., Podgorný, J., Dovčiak, M., Capitanio, F., Churazov, E., De Rosa, A., Di Marco, A., Forsblom, S., Kaaret, P., Krawczynski, H., La Monaca, F., Loktev, V., Lutovinov, A. A., Molkov, S. V., Mushtukov, A. A., Ratheesh, A., Rodriguez Cavero, N., Steiner, J. F., Sunyaev, R. A., Tsygankov, S. S., Zdziarski, A. A., Bianchi, S., Bright, J. S., Bursov, N., Costa, E., Egron, E., Garcia, J. A., Green, D. A., Gurwell, M., Ingram, A., Kajava, J. J. E., Kale, R., Kraus, A., Malyshev, D., Marin, F., Matt, G., McCollough, M., Mereminskiy, I. A., Nizhelsky, N., Piano, G., Pilia, M., Pittori, C., Rao, R., Righini, S., Soffitta, P., Shevchenko, A., Svoboda, J., Tombesi, F., Trushkin, S., Tsybulev, P., Ursini, F., Weisskopf, M. C., Wu, K., Agudo, I., Antonelli, L. A., Bachetti, M., Baldini, L., Baumgartner, W. H., Bellazzini, R., Bongiorno, S. D., Bonino, R., Brez, A., Bucciantini, N., Castellano, S., Cavazzuti, E., Chen, C.-T., Ciprini, S., Del Monte, E., Di Gesu, L., Di Lalla, N., Donnarumma, I.,

Doroshenko, V., Ehlert, S. R., Enoto, T., Evangelista, Y., Fabiani, S., Ferrazzoli, R., Gunji, S., Hayashida, K., Heyl, J., Iwakiri, W., Jorstad, S. G., Karas, V., Kislat, F., Kitaguchi, T., Kolodziejczak, J. J., Latronico, L., Liodakis, I., Maldera, S., Manfreda, A., Marinucci, A., Marscher, A. P., Marshall, H. L., Massaro, F., Mitsuishi, I., Mizuno, T., Negro, M., Ng, C.-Y., O'Dell, S. L., Omodei, N., Oppedisano, C., Papitto, A., Pavlov, G. G., Peirson, A. L., Perri, M., Pesce-Rollins, M., Petrucci, P.-O., Possenti, A., Puccetti, S., Ramsey, B. D., Rankin, J., Roberts, O., Romani, R. W., Sgrò, C., Slane, P., Spandre, G., Swartz, D., Tamagawa, T., Tavecchio, F., Taverna, R., Tawara, Y., Tennant, A. F., Thomas, N. E., Trois, A., Turolla, R., Vink, J., Xie, F., & Zane, S. (2023). Astronomical puzzle Cyg X-3 is a hidden Galactic ultraluminous X-ray source. *arXiv e-prints*, (pp. arXiv:2303.01174).

Ventura, J. (1979). Scattering of light in a strongly magnetized plasma. , 19(6), 1684–1695.

Walton, D. J., Fürst, F., Heida, M., Harrison, F. A., Barret, D., Stern, D., Bachetti, M., Brightman, M., Fabian, A. C., & Middleton, M. J. (2018). Evidence for Pulsar-like Emission Components in the Broadband ULX Sample. , 856(2), 128.

Wang, Y. M. (1987). Disc accretion by magnetized neutron stars : a reassessment of the torque. , 183, 257–264.

Wilson-Hodge, C. A., Malacaria, C., Jenke, P. A., Jaisawal, G. K., Kerr, M., Wolff, M. T., Arzoumanian, Z., Chakrabarty, D., Doty, J. P., Gendreau, K. C., Guillot, S., Ho, W. C. G., LaMarr, B., Markwardt, C. B., Özel, F., Prigozhin, G. Y., Ray, P. S., Ramos-Lerate, M., Remillard, R. A., Strohmayer, T. E., Vezie, M. L., Wood, K. S., & NICER Science Team (2018). NICER and Fermi GBM Observations of the First Galactic Ultraluminous X-Ray Pulsar Swift J0243.6+6124. , 863(1), 9.

Zane, S. & Turolla, R. (2006). Unveiling the thermal and magnetic map of neutron star surfaces though their X-ray emission: method and light-curve analysis. , 366(3), 727–738.

Zane, S., Turolla, R., Stella, L., & Treves, A. (2001). Proton Cyclotron Features in Thermal Spectra of Ultramagnetized Neutron Stars. , 560(1), 384–389.